UNIVERSIDADE FEDERAL DE PERNAMBUCO
CENTRO DE TECNOLOGIA E GEOCIÊNCIAS
PROGRAMA DE PÓS-GRADUAÇÃO EM ENGENHARIA CIVIL

TESE DE DOUTORADO

MODELAGEM E SIMULAÇÃO DE ANÁLOGOS DE RESERVATÓRIOS SILICICLÁSTICOS AFETADOS POR BANDAS DE DEFORMAÇÃO NA BACIA RIO DO PEIXE, NORDESTE DO BRASIL

Autor:

Franklyn Macedo de Souza

Orientador:

Prof. Dr. Igor Fernandes Gomes (PPGEC/UFPE)
Coorientador:
Prof. Dr. Francisco Cézar Costa Nogueira (UAEpetro/UFCG)

Recife, 2024

Recife-PE, dezembro de 2024.

UNIVERSIDADE FEDERAL DE PERNAMBUCO
CENTRO DE TECNOLOGIA E GEOCIÊNCIAS
PROGRAMA DE PÓS-GRADUAÇÃO EM ENGENHARIA CIVIL

TESE DE DOUTORADO

MODELAGEM E SIMULAÇÃO DE ANÁLOGOS DE RESERVATÓRIOS SILICICLÁSTICOS AFETADOS POR BANDAS DE DEFORMAÇÃO NA BACIA RIO DO PEIXE, NORDESTE DO BRASIL

Autor:

Franklyn Macedo de Souza

Documento submetido ao Programa de Pós-graduação em Engenharia Civil da Universidade Federal de Pernambuco como parte integrante dos requisitos necessários à defesa do doutorado em Engenharia Civil.

Área de concentração: Simulação computacional e modelagem aplicadas a petróleo e meio ambiente.

.Catalogação de Publicação na Fonte. UFPE - Biblioteca Central

Souza, Franklyn Macedo de.
Modelagem e simulação de análogos de reservatórios siliciclásticos afetados por bandas de deformação na Bacia Rio do Peixe, Nordeste do Brasil / Franklyn Macedo de Souza. - Recife, 2024.
154 f.: il.

Tese (Doutorado) - Universidade Federal de Pernambuco, Centro de Tecnologia e Geociencias, Pós-Graduação em Engenharia Civil, 2024.
Orientação: Igor Fernandes Gomes.
Inclui referências.

1. Bandas de deformação; 2. Modelagem geológica; 3. Simulação numérica. I. Gomes, Igor Fernandes. II. Título.

FRANKLYN MACEDO DE SOUZA

MODELAGEM E SIMULAÇÃO DE ANÁLOGOS DE RESERVATÓRIOS SILICICLÁSTICOS AFETADOS POR BANDAS DE DEFORMAÇÃO NA BACIA RIO DO PEIXE, NORDESTE DO BRASIL

Tese em Engenharia Civil da Universidade Federal de Pernambuco, Centro de Tecnologia e Geociências, como requisito para obtenção do título de Doutor em Engenharia Civil, Área de Simulação e Gerenciamento de Reservatórios de Petróleo.

Aprovada em 20/12/2024

Orientador: Prof. Dr. Igor Fernandes Gomes – UFPB
Coorientador: Prof. Dr. Francisco Cézar Costa Nogueira - UFCG

gov.br Documento assinado digitalmente
IGOR FERNANDES GOMES
Data: 20/01/2025 09:13:43-0300
Verifique em https://validar.iti.gov.br

gov.br Documento assinado digitalmente
FRANCISCO CEZAR COSTA NOGUEIRA
Data: 27/01/2025 09:00:30-0300
Verifique em https://validar.iti.gov.br

BANCA EXAMINADORA

participação por videoconferência
Prof. Dr. José Antônio Barbosa (examinador interno)
Universidade Federal de Pernambuco

gov.br Documento assinado digitalmente
MATHEUS AMADOR NICCHIO
Data: 30/01/2025 14:07:34-0300
Verifique em https://validar.iti.gov.br

participação por videoconferência
Prof. Dr. Matheus Amador Nicchio (examinador externo)
Universidade Federal do Rio de Janeiro

gov.br Documento assinado digitalmente
DAVID LINO VASCONCELOS
Data: 04/01/2025 08:18:41-0300
Verifique em https://validar.iti.gov.br

participação por videoconferência
Prof. Dr. David Lino Vasconcelos (examinador externo)
Universidade Federal de Campina Grande

gov.br Documento assinado digitalmente
EDSON DE ANDRADE ARAUJO
Data: 02/01/2025 22:49:23-0300
Verifique em https://validar.iti.gov.br

participação por videoconferência
Prof. Dr. Edson de Andrade Araújo (examinador externo)
Universidade Federal de Campina Grande

participação por videoconferência
Prof.ª Dr.ª Débora Cristina Almeida de Assis (examinadora externa)
Universidade Federal de Pernambuco

A toda minha família.

AGRADECIMENTOS

Primeiramente, gostaria de expressar minha mais sincera gratidão a todos aqueles que, de maneiras diversas e valiosas, contribuíram para a realização deste trabalho de pesquisa. Cada um de voces desempenhou um papel crucial, desde os momentos iniciais de concepção até os estágios finais de conclusão, e por isso sou imensamente grato. Suas orientações, *insights*, apoio emocional e encorajamento foram essenciais para superar os desafios ao longo desta jornada acadêmica. Sem a colaboração e apoio de vocês, este trabalho não teria alcançado o nível de excelência que buscamos. Por isso, meu mais profundo agradecimento a cada um de vocês por fazerem parte deste importante capítulo da minha trajetória acadêmica, tanto meus amigos de LAPEP, quanto os novos amigos que construí na UFPE, onde sou extremamente grato por esta oportunidade.

Gostaria de agradecer a minha esposa Renally que me acompanha nesta jornada toda desde o ensino médio, sempre me apoiando em todas as decisões e me dando força para continuar e que agora Jesus nos presentiou com a benção maior que pode nos dá: A honra de sermos pais de um filho lindo chamado Theo. Amo vocês e amo nossa vida hoje.

Agradeço aos meus pais por todo o esforço que foi feito durante toda minha vida para que chegasse esse momento. Em especial, agradeço a minha mãe Veroneide e minha irmã Camila por tudo. Amo vocês

Agradeço ao meu co-orientador de doutorado Prof. Dr. Francisco Cezar Costa Nogueira, que nesta tese atuou como co orientador, mas que foi a pessoa responsavel academicamente por todo meu percurso desde o primeiro período, sendo o principal responsável por todo meu desenvolvimeto. Este foi quem me proporcionou grandes oportunidades de aprendizado, bem como estagios e quem me guiou em todo esses quase 15 anos de trabalho em conjunto. Obrigado por tudo professor.

Agradeço ao meu orientador, Prof. Dr. Igor Fernandes Gomes por ter me orientado neste doutorado. Com ele tive oportunidades de crescimento pessoal e acadêmico incríveis, nos tornando bons amigos durante esta jornada.

Agradeço aos meus colegas de trabalho que, por muitas vezes, me atenderam nas trocas de plantões para que eu pudesse assistir aulas e não tivesse nenhum prejuízo acadêmico. Voces tambem tem participação neste trabalho.

Por fim, à Petrobras/UFCG pelo financiamento do projeto de pesquisa DEBRIP: análise multiescalar e geração de banco de dados geofísico, geológico, modelagem e simulação numérica (TC 5850.0109438.18.9) ao qual minha tese fez parte.

RESUMO

As bandas de deformação são estruturas rúpteis que podem ocorrer como estruturas *single* (estruturas isoladas) ou *clusters* (estruturas agrupadas). Estas desempenham um papel crucial na dinâmica de deformação de rochas e no comportamento hidromecânico de reservatórios. O estudo dessas estruturas é fundamental para avaliar a integridade de reservatórios, prever trajetórias de escoamento de fluidos e otimizar a exploração de recursos naturais, como petróleo, gás e água subterrânea. Assim, o principal objetivo desta tese é a modelagem geológica e a simulação numérica de escoamento para cenários de zonas de falhas geológicas em análogos de reservatórios siliciclásticos. Em escala de afloramento, o foco será no entendimento do papel destas estruturas nos reservatórios de petróleo. Uma outra abordagem será o emprego de estratégias de *flow basic upscaling* para modelos de alta fidelidade 2D (com modelos 7 por 2.5 metros), em escala de uma porção aflorante da zona de falha, e simulação de fluxo convencional de modelos 3D (150 x 80 x 40 metros) em escala de afloramento, com foco no entendimento do papel destas estruturas dentro de reservatórios. Para isso, utilizou se de uma vasta base de dados, coletados em campo e outros compilados de trabalhos previamentes publicados, onde, dentro desses se teve levantamento aéreo com drones, coleta de amostras para análise em laboratório e realização de perfis de scanlines. Nossos resultados indicam que a inclinação dessas estruturas é um fator crucial no cálculo da permeabilidade equivalente, reforçando a necessidade de considerar a distribuição não homogênea da permeabilidade nos reservatórios, devido a casos observados onde a zona de cluster ter valores de permeabidade que rocha hospedeira. Além disso, a conectividade hidráulica nos clusters é diretamente influenciada pelas zonas de linkagem, onde áreas de alta complexidade estrutural podem aumentar significativamente a permeabilidade efetiva. Para que os efeitos das bandas de deformação no fluxo sejam claramente evidenciados, é necessário que a rocha hospedeira apresente, no mínimo, três ordens de grandeza de diferença nos valores de permeabilidade, em comparação a permeabilidade das bandas. A distribuição adequada dos poços também desempenha um papel importante na definição do esquema de produção, contribuindo para uma melhor gestão do campo. Modelos de alta fidelidade são essenciais para capturar com maior precisão as variações no campo de pressão, enquanto os modelos de resistividade se mostraram ferramentas valiosas para a aquisição indireta de dados de porosidade, devido ao seu baixo custo de aquisição. Diante disso, é imprescindível a continuidade das pesquisas nessa área, com o objetivo de aprofundar o entendimento e aprimorar as ferramentas de modelagem e simulação.

Palavras-chave: Bandas de deformação; Resistividade; Propriedades petrofisicas; Zonas de bandas de deformação; Simulação; Modelagem.

ABSTRACT

Deformation bands can appear as single structures or clusters. These structures play a crucial role in the dynamics of rock deformation and the behavior of geological reservoirs. The study of these features is fundamental for assessing reservoir integrity, predicting flow pathways, and optimizing the exploitation of natural resources such as oil, gas, and groundwater. Thus, the primary objective of this thesis is to construct 2D and 3D models, coupled with high-fidelity flow simulation in the 2D models and the simulation of 3D models at outcrop scale, aiming to understand the role of these structures within reservoirs. For this purpose, an extensive database was utilized, including field-collected data and others compiled from previously published studies. Data acquisition included aerial surveys with drones, sample collection for laboratory analysis, scanline profiling, among others. This data densification is critical for distributing information in the model construction process. It is concluded that deformation bands can act as either partial barriers or conduits, depending on their characteristics. The inclination of these structures is a crucial factor in calculating equivalent permeability, emphasizing the need to consider the heterogeneous permeability distribution in reservoirs, as evidenced by cases where cluster zones show permeability values distinct from those of the host rock. Additionally, hydraulic connectivity within clusters is directly influenced by linkage zones, where areas of high structural complexity can significantly increase effective permeability. For the effects of deformation bands on flow to be clearly evident, the host rock must present at least three orders of magnitude difference in permeability compared to the bands' permeability. Proper well distribution also plays an important role in defining production schemes, contributing to better field management. High-fidelity models are essential for more accurately capturing pressure field variations, while resistivity models have proven valuable for indirect porosity data acquisition due to their low acquisition cost.

Given this, continuing research in this area is imperative to deepen understanding and improve modeling and simulation tools.

Keywords: Deformation bands; Resistivity; Petrophysical properties; Deformation bands cluster zone; Simulation; Modeling.

SUMÁRIO

LISTA DE FIGURAS E TABELAS

Capítulo 1

Introdução

1.1. Apresentação

Esta Tese de Doutorado é parte dos requisitos necessários para a obtenção do título de Doutor em Engenharia Civil, com ênfase em simulação computacional e modelagem aplicadas à área de petróleo e meio ambiente, pelo Programa de Pós-graduação em Engenharia Ciivil (PPGEC) da Universidade Federal de Pernambuco (UFPE). Esta pesquisa visa desenvolver modelos geológicos (2D e 3D) e realizar simulações numéricas de escoamento em análogos de reservatórios siliciclásticos que são impactados por bandas de deformação. Para alcançar esse propósito, a área de estudo escolhida foi a Bacia Rio do Peixe, localizada no extremo oeste do estado da Paraíba, com foco nos afloramentos localizados nas proximidades da zona de falha Portalegre.

Durante o período de elaboração dessa tese, o autor recebeu bolsa de estudo da PETROBRAS, por meio do projeto DEBRIP. O doutorado foi realizado em parte na UFPE, no laboratório de métodos computacionais em geomecânica (LMCG), sob orientação do professor Dr Igor Fernandes Gomes e a outra parte no laboratório de pesquisa e exploração de petróleo (LAPEP), sob co-orientação do professor Dr Francisco Cézar Costa Nogueira.

1.2. Estrutura da Tese

Diversos programas de pós-graduação em diferentes áreas do conhecimento permitem que seus discentes desenvolvam teses em formato de artigos, submetidos e/ou publicados em revistas científicas. Esse modelo confere maior objetividade às teses, cuja disseminação é mais ampla, além de tornar mais concisas as ideias defendidas. Essa tese será estruturada em seis capítulos, onde detalhes da metodologia, os resultados e as discussões foram redigidos em forma de artigos publicados e submetidos em periódicos internacionais. A escolha desse formato de dissertação foi motivada pela constatação de que desta maneira, as teses são mais focadas no tema central da pesquisa.

Seguindo essa propositura, o **Capítulo 1 (Introdução)** tem como finalidade apresentar a Tese, descrever seus objetivos, justificativas, base de dados e localizar espacialmente o leitor em relação à área de pesquisa.

No **Capítulo 2 (Referêncial teórico)** é proposta uma explanação sobre bandas de deformação e todos os outros conteúdos pertinentes para o desenvolvimento da tese, bem como sobre a construção de modelos que consideram a inserção dessas estruturas, abordando também os aspectos gerais da simulação de fluxo.

No **Capítulo 3 (Geologia Regional e área de estudo)**, é mostrada uma revisão geral sobre a geologia regional da BRP, contemplando os aspectos regionais nos quais esta bacia está inserida e os tipos de unidades estratigráficas presentes, em especial na área de estudo.

No **Capítulo 4**, é apresentado o manuscrito “**2D modeling and simulation of deformation bands’ effect on fluid flow: Implications for hydraulic properties in siliciclastic reservoirs**”, publicado no *Journal of Structural Geology*, Volume 158, May 2022, https://doi.org/10.1016/j.jsg.2022.104581. Esse manuscrito aborda a influência das bandas de deformação nas propriedades hidráulicas de reservatórios siliciclásticos, para cenários 2D. Vale ressaltar que o mesmo se encontra em ingês, haja vista o mesmo já foi publicado e no capítulo foi realizado apenas a inserção deste.

No **Capítulo 5**, é apresentado o manuscrito “**Fluid flow in a deformation band fault zone: Implications for modelling and numerical simulation in Siliciclastic rocks**”, submetido para a revista *Marine and Petroleum Geology*. Esse manuscrito aborda o fluxo de fluidos em zonas de linkagem, bem como o comportamento do fluido, quando se tem esquemas de produção.

No **Capítulo 6**, é apresentado de forma concisa as conclusões deste desenvolvimento de tese.

1.3. Contextualização do problema

A devida caracterização de reservatórios petrolíferos é de suma importância para a escolha da estratégia a ser adotada para exploração e produção de uma determinada jazida de petróleo. Os modelos de propriedades gerados permitem o entendimento das heterogeneidades associados ao campo e uma análise para melhor distribuição dos atributos dentro do modelo.

Associado a construção desses modelos, é necessário a incorporação de todas as informações obtidas através de estudos prévios. Dentro desse processo de modelagem, é possível que se esteja trabalhando em uma grande zona de falha, composta por diferentes elementos arquiteturais, tais como: planos de falha, núcleo da falha e a zona de dano. Por terem uma espessura que pode variar de poucos centímetros a vários quilômetros, é necessário que sejam considerados dentro dos estudos de modelagem.

Diversos problemas na indústria de petróleo ocorrem associados a zonas selantes afetadas por bandas de deformação (FOSSEN, 2010). Por exemplo, redução da porosidade e da permeabilidade nas bandas de deformação, em comparação com o arenito não deformado, geralmente é vista como uma barreira na migração e acúmulos de fluidos em reservatórios, sejam estes de água, óleo ou gás (ANTONELLINI et al., 1994; HOLCOMB et al., 2007; FAULKNER et al., 2010). Entretanto, há também trabalhos que apontam que bandas de deformação possam atuar como condutos de fluidos (PARRYET al., 2004; SAMPLE et al., 2006). Conforme mencionado anteriormente, as bandas de deformação, quando presentes em reservatórios de petróleo, podem atuar como barreira ao escoamento de fluidos ou como condutos para sua migração, podendo exercer quaisquer dessas funções. Os fatores controladores para definir qual dessas funções será exercida estão relacionadas com a espessura da banda, disposição espacial no reservatório, características permo-porosas e direção do fluxo de fluido em relação a estrutura. Apesar das bandas de deformação possuírem espessura milimétrica a centimétrica, seu impacto na redução da permeabilidade em um sistema formado por arenitos porosos pode ser de até 6 ordens de grandeza (Ballas et al., 2015; Silva et al., 2022). Nesse contexto, inserem-se diversas acumulações de petróleo em arenitos pouco consolidados com alta porosidade, como por exemplo, os reservatórios turbidíticos da Bacia de Campos (WINTER et al., 2007). Sendo assim, a compreensão da deformação em arenitos pouco consolidados e de sua influência no escoamento em meio poroso é vital para o aumento do fator de recuperação dessas acumulações, fazendo-se necessária a correta representação do impacto das bandas de deformação, que possuem escala subsísmica, nos modelos geológicos de reservatório.

As características internas das bandas de deformação têm potencial para mudar as propriedades do reservatório, afetando assim a escolha das melhores estratégias para produção de óleo e gás (FISHER E KNIPE, 2001; HESTHAMMER e

FOSSEN, 2001; OGILVIE E GLOVER, 2001). Em função da possibilidade de bandas de deformação e zonas de bandas de deformação serem longas suficiente para compartimentar reservatórios conforme discutido por Aydin (1978), Pittman (1981), Jamison e Stearns (1982), Underhill e Woodcock (1987) e Gibson (1998), vem sendo dada ênfase para o estudo das propriedades petrofísicas e como estas atuam modificando as propriedades das rochas, como porosidade e permeabilidade.

O estudo de bandas de deformação e sua representatividade no escoamento de fluidos é bem desafiador devido a insuficiência de informações relacionada à limitação da resolução de ferramentas de análise e mapeamento em reservatórios de hidrocarbonetos. A melhor maneira de se identificar a ocorrência destas estruturas no reservatório é através da amostragem de rocha, principalmente em testemunhos, porém este tipo de dado é muito restrito, sendo dificilmente obtido em regiões propícias à ocorrência de bandas de deformação, muitas vezes limitadas à zona de dano de falhas (FOSSEN & HESTHAMMER, 2001).

Assim, uma maneira de reduzir e tentar representar estas estruturas na construção do modelo é através do estudo em análogos, onde se irá eliminar esse *“gap”* de escalas, que se refere a falta de informações no salto de uma escala menor para uma maior, de forma a serem ferramentas preditivas na exploração e na produção de reservatórios que apresentam essas características.

A presente tese pretende preencher uma lacuna científica, que é o desenvolvimento de um modelo de alta fidelidade baseado em exposição de estruturas de bandas de deformação. Estas estruturas são sub-sismicas, em afloramentos análogos de reservatórios com zona de falha, aliados a uma investigação geofísica de alta resolução e medidas petrofísicas que constituem duas opções de modelos de reservatório em escala de afloramento para uma investigação em maior detalhe e técnicas de simulação de métodos rotineiramente empregados no estudo de escoamento de petróleo.

1.4. Justificativa

O estudo de afloramentos como análogos de reservatórios de hidrocarbonetos tem sido utilizado amplamente ao longo das últimas décadas na indústria do petróleo por constituir uma poderosa ferramenta de aquisição de dados, melhorando assim a elaboração de modelos detalhados de reservatórios em sub-superficie. Este estudo fornece valiosas informações, e permite avaliar de forma qualitativa e quantitativa características como dimensões e geometrias dos corpos sedimentares e descontinuidades estruturais laterais e verticais em escala sub-sísmica, que são de difícil realização em reservatórios de hidrocarbonetos em sub-superfície pela baixa resolução dos dados sísmicos e de poço. Devido a essa problemática, faz se necessário a construção e simulação de modelos geológicos que incorporem o impacto das bandas de deformação no fluxo de fluidos em meios porosos. Na presente tese, foram estudados 02 (dois) afloramentos distintos, onde o afloramento 1, denominado “afloramento Melancias”, utilizou-se o *software* acadêmico em elementos finitos para modelagem numérica bidimensional de escoamento monofásico, com propósito da avaliação do impacto das bandas de deformação no escoamento de fluidos em um modelo de alta fidelidade, através da determinação numérica de permeabilidade equivalente em um processo de *flow basic upscaling*. No afloramento 2 (dois), denominado como “Utah”, adota-se o *software* Petrel para modelagem geológica tridimensional, contemplando as estruturas inseridas e consideradas dentro da construção fidedigna em um segundo caso a ser modelado e posteriormente simulado. A partir disso, será possível representar a redução de permeabilidade no fluxo de fluidos quando atravessar as bandas de deformação, bem como o comportamento das zonas de *linkagem*, que se trata das conexões entre as terminações de estruturas distintas, ao serem subtmetidos ao escoamento de fluidos.

A utilização da modelagem 2D se deu devido a exposição vertical do afloramento 1 modelado, haja vista foi possível uma aquisição mais detalhada das propriedades necessárias para inserir no modelo e assim obter parâmetros com o objetivo de realizar um upscaling de propriedades para modelos maiores. Para a realização da modelagem 3D, foi necessário a escolha de outro afloramento, distante a 1,6 km (Figura 1.1), pois no afloramento 1 não era possível observar os “*tip*s” de falha, que são as extremidades onde ela já não se propaga mais. Assim, foi escolhido o afloramento 2, onde os *tips* de falha estão bem visíveis e presentes e foram inseridos no modelo.

Figura 1.1 - Mapa com a localização dos afloramentos estudados nesta tese, onde os mesmos têm uma distância de 1.6 km entre eles.

1.5. Objetivos

A principal finalidade desta tese é caracterizar a influência destas estruturas tectônicas, presentes nas unidades cretáceas da Bacia Rio do Peixe (BRP), sobre o padrão de migração e acumulação de fluidos da Bacia Rio do Peixe e como essas estruturas afetam as propriedades hidráulicas dessas unidades aflorantes. Assim, a presente tese visa caracterizar as bandas de deformação, de forma estrutural e petrofísica, quando estas estão presentes em afloramentos considerados análogos de reservatório deformados na BRP.

Como objetivos específicos desta tese temos:

- •. Coletar e mapear imagens de alta resolução levantadas com drone em afloramentos, para construção do modelo geológico da área de estudo, tanto 2D quanto 3D;
- •. Realizar e compilar dados de *scanlines* para obter dados estruturais e povoar o modelo geológico;

•. Construir um modelo bidimensional, simular fluxo monofásico e determinar permeabilidades equivalentes via *flow based upscaling* utilizando o *software* em elementos finitos CODE BRIGHT;

•. Construir um modelo tridimensional utilizando o *software* PETREL;

•. Realizar simulações de fluxo utilizando o FRONTISIM a partir de modelos construídos no PETREL;

•. Realizar levantamentos de eletrorresistividade e observar se é possível realizar uma inversão de dados e assim obter se indiretamente os valores de porosidade;

•. Modelar uma zona de deformação em escala de produção e observar o comportamento desta, quando submetida ao fluxo de fluidos;

•. Verificar a influência das Bandas de Deformação na produção e nas frentes de saturação;

•. Estimar a relação das propriedades petrofísicas e o comportamento hidráulico das rochas deformadas e não deformadas por bandas de deformação;

•. Criar um banco de dados com propriedades petrofísicas das estruturas tectônicas, passíveis de serem utilizados no estudo de análogos de reservatórios siliciclásticos deformados.

•. Elaborar artigos científicos com os resultados desta pesquisa.

1.6. Dados utilizados

O conjunto de dados utilizados nesta pesquisa abrange dados de natureza estrutural e petrofísica. No entanto, nesse capítulo são descritos apenas a origem desses dados e os parâmetros de aquisição, enquanto o detalhamento do processamento e a metodologia de interpretação estão descritos nos manuscritos apresentados nos capítulos 4 e 5 dessa tese.

No afloramento 1 (Melancias) foram adquiridas imagens de alta resolução obtidos por *VANT* (Veículo Aéreo Não Tripulado), objetivando serem utilizadas de base da interpretação devido a alta resolução. A partir destas, foi possível o mapeamento das principais estruturas e a inserção destas no modelo para a simulação. Tambem foram realizados perfis de *scanlines* cruzando as Bandas de deformação, onde parâmetros como espessura, direção das estruturas e espaçamento entre estas foram coletados e inseridas dentro do modelo. Após a coleta estrutural, deu se início a coleta petrofísica, onde as estruturas foram dividas por direção (NE-SW; N-S e E-W) e foram coletados *plugs* em cada uma dessas direção, para que no laboratório fossem realizadas as devidas análises e tivessemos os valores de porosidade e permeabilidade para inserir no modelo.

No afloramento 2 (Utah) foram utilizados como base dois artigos científicos disponíveis na bibliografia para a construção do modelo geológico a ser simulado posteriormente. O primeiro foi publicado por de Souza et al., 2021, intitulado "*Growth of cataclastic bands into a fault zone: A multiscalar process by microcrack coalescence in sandstone of Rio do Peixe Basin, NE Brazil*" na revista *Journal of Structural Geology.* A partir deste, foi possível uma melhor compreensão estrutural do afloramento e quais sets principais presentes, bem como seu controle na formação dos *clusters.* O segundo foi publicado por *Torabi et al.*, 2021, intitulado "V*ariation of rhickness, internal structure and petrophysicl properties in a deformation band faul zone in siliciclastic rocks" na revista Marine and Petroleum Geology.* Neste foi possível entender importancia da heterogeneidade estrutural e geométrica das falhas e como isto influencia nas propriedades petrofisicas das rochas. Adicionalmente, foi realizado um levantamento de eletrorresistividade, objetivando a criação do modelo de distribuição, a fim de observar a presença de anomalias em subsuperficie e posterior utilização do modelo como base para contrução do modelo de porosidade. O conjunto de dados utilizados neste trabalho é bem vasto e permite construir um modelo geologico de alta fidelidade, tendo em vista a distribuição das coletas. Deste trabalho foram compilado os dados estruturais, para se somar à interpretação de de Souza et al., 2021, bem como as scanlines e os dados petrofísicos da área em estudo.

Paralelo a isto e objetivando adensar mais a região com dados, foram adquiridas imagens de alta resolução com o VANT, bem como a coleta de permeabilidades com o equipamento *Tiny Perm*. Somando-se a isto, foi realizado um levantamento de eletrorresistividade, cujos dados poderão ser utilizados na modelagem das propriedades.

1.7. Referências

ANTONELLINI, M. A.; AYDIN, A.; POLLARD, D. D. Microstructure of deformation bands in porous sandstones at Arches National Park, Utah. Journal of Structural Geology, v. 16, p. 941-959, 1994.

AYDIN, A. Small faults formed as deformation bands in sandstone. Pure and Applied Geophysics, v. 116, p. 913-930, 1978.

BALLAS, G.; FOSSEN, H. & SOLIVA, R. 2015. Factors controlling permeability of cataclastic deformation bands and faults in porous sandstone reservoirs. Journal of Structural Geology, 76: 1-21.

FAULKNER, D. R; et al. A review of recent developments concerning the structure, mechanics and fluid flow of fault zones. Journal of Structural Geology, v. 32, p. 1557-1575, 2010

FISHER, Q. J.; R. J. KNIPE. The permeability of faults within siliciclastic petroleum reservoirs of the North Sea and Norwegian Continental Shelf: Marine and Petroleum Geology, v. 18, p. 1063–1081, 2001

FOSSEN, H. Geologia Estrutural. 1ª Edição. São Paulo: Oficina de textos. p. 566, 2010.

GIBSON, R. G. Physical character and fluid-flow properties of sandstone-derived fault zone: Geological Society (London) Special Publication. v. 127, p. 83–97, 1998.

HESTHAMMER, J.; FOSSEN, H. Structural core analysis from the Gullfaks area, northern North Sea: Marine and Petroleum Geology, v. 18, p. 411–439, 2001.

HOLCOMB, D.; RUDNICKI, J. W.; ISSEN, K. A.; STERNLOF, K. Compaction localization in the Earth and the laboratory: state of the research and research directions. Acta Geotechnica, v. 2, p. 1-15, 2007

JAMISON, W. R.; STEARNS, D. W. Tectonic deformation of Wingate Sandstone, Colorado National Monument: AAPG Bulletin, v. 66, p. 2584–2608, 1982.

OGILVIE, S. R.; GLOVER, P. W. J. The petrophysical properties of deformation bands in relation to their microstructure: Earth and Planetary Science Letters, v. 193, p. 129–142, 2001.

PARRY, W. T; CHAN, M. A; BEITLER, B. Chemical bleaching indicates episodes of fluid flow in deformation bands in sandstone. 2004.

PITTMAN, E. D. Effect of fault-related granulation on porosity and permeability of quartz sandstones, Simpson Group (Ordovician) Oklahoma: AAPG Bulletin, v. 65, p. 2381–2387, 1981.

SAMPLE, J.C; WOODS, S; BENDER, E; LOVEALL, M. Relationship between deformation bands and petroleum migration in an exhumed reservoir rocks, Los Angels Basin, Califórnia, USA. 2006.

SILVA, M. E.; NOGUEIRA, F. C.C.; PÉREZ, Y.A.R.; VASCONCELOS, D. L.; STOHLER, R. C.; SANGLARD, J. C.D.; BALSAMO, F.; BEZERRA, F. H.R.; CARVALHO, B. R.B.M.; SOUZA, J. A.B. Permeability modeling of a basin-bounding fault damage zone in the Rio do Peixe Basin, Brazil. Marine and Petroleum Geology, v. 135, p. 1-22, 2022.

UNDERHILL, J. R.; WOODCOCK, N. H. Faulting mechanisms in high porosity sandstones: New Red Sandstone, Arran, Scotland, in M. E. Jones and R. M. F. Preston, eds.,Deformation of sediments and sedimentary rocks: Geological Society Special Publication, v, 29, p. 91–105, 1987.

WINTER, W.R., JAHNERT, R.J. & França, A.B. 2007. Bacia de Campos. Boletim Geológico de Geociências, 15(2): 511-529.

Capítulo 2

Revisão Bibliográfica

2. Revisão Bibliográfica

2.1. Introdução

Neste capítulo, empreenderemos uma revisão bibliográfica abrangente, visando contextualizar e fundamentar nossa pesquisa no corpo existente de conhecimento. A relevância dessa revisão reside na sua capacidade de proporcionar uma compreensão aprofundada das teorias, conceitos e descobertas relacionadas ao tema em análise. Ao explorar e analisar criticamente as contribuições acadêmicas existentes, objetivamos identificar lacunas no conhecimento e estabelecer um sólido alicerce para a construção de argumentos e abordagens inovadoras ao longo deste trabalho.

2.2. Zona de falha

Por muitas vezes, as falhas geológicas são consideradas como descontinuidades desenvolvidas, localizadas em um local submetido a tensões. Entretanto, a falha não pode ser considerada como um único traço ou segmento, mas sim como uma zona deformada, compondo uma porção volumétrica deformada.

A arquitetura de uma zona de falha foi definida por Caine et al. (1996) como sendo litologicamente heterogênea, representando descontinuidades estruturalmente anisotrópicas na crosta. Podem atuar como condutos, barreiras individuais ou sistemas integrados de condutos e barreiras, otimizando ou dificultando o movimento de fluidos nas rochas deformadas. Em termos arquiteturais, a zona de falha é composta por 3 elementos principais (Figura 2.1): núcleo de falha, zona de dano e protolito. O núcleo da falha é a porção que concentra maior deformação, sendo caracterizada pela formação de intensa catáclase e brechação, podendo formar clusters em seu interior. Já a zona de dano é menos deformada que o núcleo principal, onde se observa a presença de bandas de deformação mais espaçadas entre si, bem como a presença de pequenas falhas e, por vezes, pequenas juntas (CHOI et al., 2016). A extensão da zona de dano, perpendicular ao núcleo principal, é definida a partir da frequência de ocorrência dessas estruturas, onde tendem a diminuir em direção ao protólito. Alem disso, há uma relação preditiva de que quando maior for o rejeito da falha, mais será a espessura da zona de dano (Schol, 1987). Ao observar o protólito, este é a porção onde ocorrem poucas ou quase nenhuma banda de deformação, haja vista este elemento é o mais distante do núcleo principal e as possíveis estruturas que estiverem presentes podem ser relacionadas às estruturas preexistentes. Caine et al. (1996) indicam que não existiria relação de escala entre os elementos e nem seria necessário que todos estejam sempre presentes em uma mesma zona de falha.

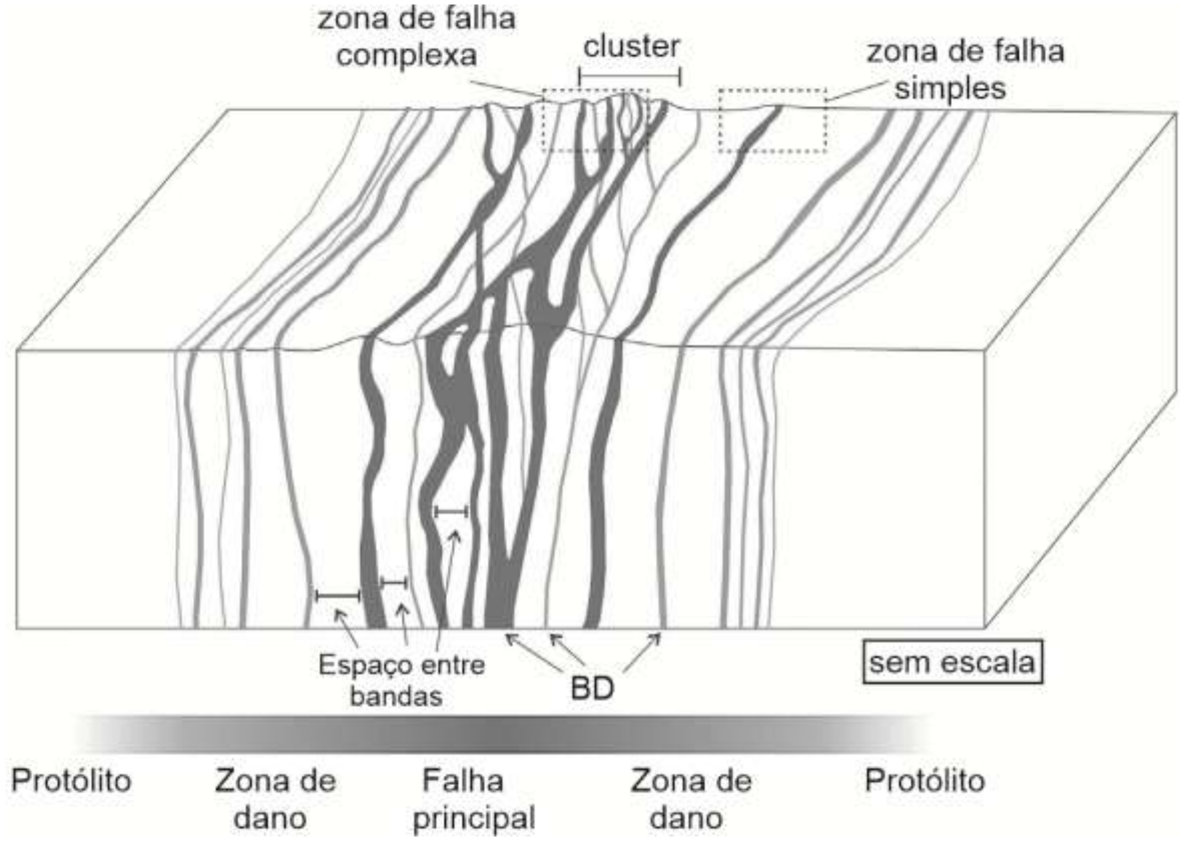

Figura 2.1 - Disposição esquemática de uma zona de falha e seus elementos arquiteturais (Modificado de PONTES et al., 2019).

2.3. Bandas de deformação

As bandas de deformação são rotineiramente caracterizadas como estruturas rúpteis, onde pequenas falhas se desenvolvem em rochas com porosidade alta (FOSSEN et al., 2007; TORABI E FOSSEN, 2009). Quando presentes de forma individual em reservatórios, estas estruturas não são capazes de promover alterações significativas, que sejam capazes de interferir nas propriedades do reservatório. Entretanto, quando dispostas em grandes “clusters” ou concentradas em regiões especificas, estas bandas podem ter influência na migração e fluxo de fluidos no interior do reservatório, podendo atuar como barreira ou corredor para o escoamento, como também agindo nas propriedades mecânicas do reservatório (PONTES et al., 2019). Localmente, estas estruturas alteram propriedades petrofísicas, geomecânicas, geométricas e texturais das rochas a qual estão inseridas (FOSSEN et al., 2007; TORABI; FOSSEN; ALAEI, 2008; PONTES et al., 2019; NOGUEIRA et al., 2021). È de suma importância também o entendimento do comportamento da região entre bandas de deformação, que é uma área dentro de um material deformado que está localizada entre bandas, onde tem se como característica a presença de deformação local menor.

Alguns fatores são de suma importância no processo de formação e desenvolvimento de bandas de deformação, sendo estes os ambientes tectônicos, a pressão confinante (relacionado a profundidade de soterramento), grau de litificação da rocha hospedeira, pressão de fluido dos poros, mineralogia da rocha hospedeira, tamanho, formato e selecionamento dos grãos (FOSSEN et al., 2007). Isso gera certos tipos de classificação dessas estruturas.

De acordo com Fossen (2010), as bandas de deformação podem ser classificadas, pela sua cinemática, em bandas de dilatação, cisalhamento e compactação (Figura 2.2). As bandas de dilatação ocorrem quando a tensão aplicada na rocha, tensão esta responsável pela deformação, gera novos poros ou aumenta o tamanho dos poros existentes, ao invés de fechar, que é o mais comum de se observar (ANTONELLINI et al., 1994). Na banda de cisalhamento, associada à cinemática , tem-se o movimento dos grãos na direção da aplicação da força cisalhante, junto com a rotação deles. Por último, nas bandas de compactação acontece a reorganização dos grãos que se dá com uma aplicação de tensão compressiva, que compacta a rocha e reorganiza os grãos, reduzindo assim as propriedades petrofísicas neste tipo de banda. Segundo a revisão proposta por Stohler (2021), a grande maioria das bandas de deformação descritas na literatura são bandas de cisalhamento com compactação subordinada (bandas de cisalhamento compactantes) causadas pela reorganização dos grãos com ou sem catáclase. O componente de compactação contribui para o endurecimento por deformação e na criação da zona de bandas de deformação que precede a formação da superfície de deslizamento (FOSSEN et al., 2007; FOSSEN et al., 2017).

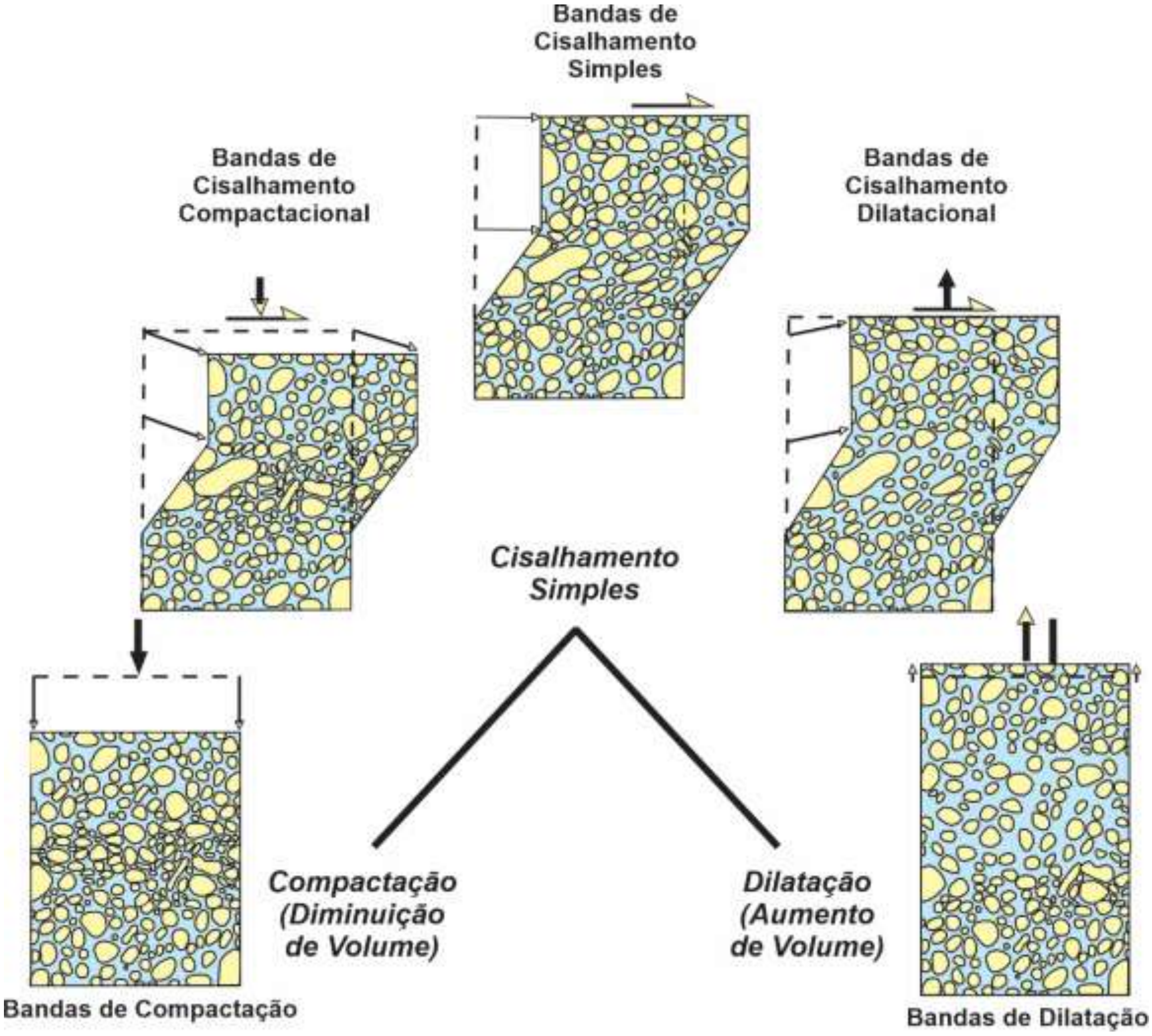

Figura 2.2 - Classificação das bandas de deformação, de acordo com sua cinemática (FOSSEN et al., 2007).

Outra forma de classificar as bandas de deformação é de acordo com o mecanismo associado à sua formação. Essa é de grande importância devido ao mecanismo dominante controlar as mudanças na porosidade e permeabilidade das estruturas (FOSSEN et al., 2017). Vários fatores podem influenciar nos mecanismos, como cimentação, porosidade, mineralogia etc. Quando tratamos das bandas, os mecanismos podem ser fluxo granular, catáclase, lubrificação de filossilicatos e dissolução e cimentação (Figura 2.3).

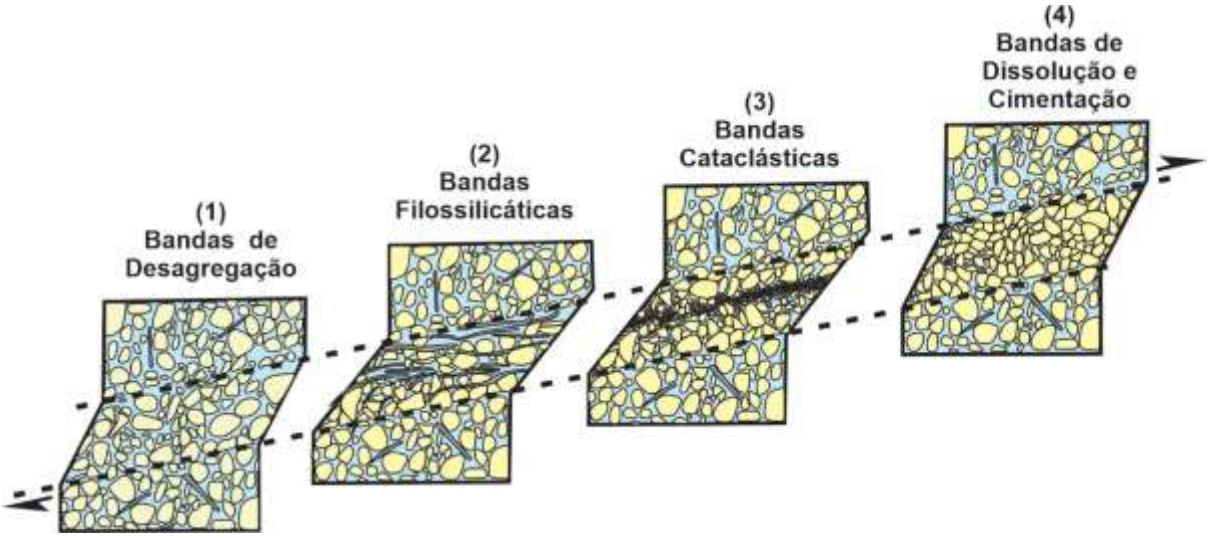

Figura 2.3 - Principais tipos de bandas de deformação, baseado no mecanismo de deformação. (a) banda de desagregação, formada por fluxo granular. (b) banda filossilicática, formada pela remobilização de argila. (c) banda cataclástica, formada por catáclase. (d) banda de dissolução ou cimentação (FOSSEN et al., 2007).

De maneira suscinta, fluxo granular ocorre pelo cisalhamento dos grãos podendo ter rotação e rearranjo dos grãos. Este processo forma bandas de deformação do tipo desagregação, que são encontradas em areias e arenitos pouco consolidados (FOSSEN et al., 2007). As bandas filossilicáticas formam-se em arenitos com porção maior que 10% de minerais de argila. Estas podem ser consideradas um tipo especial de bandas formadas por fluxo granular, em que a argila facilita o deslizamento dos grãos (FOSSEN et al., 2007). As bandas filossilicáticas são de fácil detecção, pois os filossilicatos alinhados conferem às bandas cores ou tramas, que são semelhantes aos das camadas ricas em filossilicatos na rocha não deformada (FOSSEN, 2010). Se a argila for o mineral laminar dominante, as bandas são caracterizadas por granulometria fina e baixa porosidade. Outro tipo de banda é a cataclástica, que consiste em um núcleo completamente deformado e todo cominuído, devido à fricção dos grãos. O núcleo é facilmente percebido por ter uma redução no tamanho dos grãos (ENGELDER, 1974; RAWLING E GOODWIN, 2003) e colapso dos poros, reduzindo assim sua porosidade e permeabilidade (FOWLES E BURLEY, 1994; STERNLOFET al., 2004; FOSSEN E BALE, 2007; SAILLET, 2009; TUECKMANTEL et al., 2010; SUN et al., 2011). De acordo com Fossen (2010), estas bandas acontecem comumente em profundidades que variam entre 1,5 e 3,0 km. Por fim as bandas de cimentação e dissolução ocorrem quando os cristais de minerais diagenéticos crescem ou são dissolvidos a partir de suas faces recém-quebradas por moagem ou deslizamento.

2.4. Eletrorresistividade

O método de eletrorresistividade implica na injeção de corrente elétrica contínua ou alternada de baixa frequência (inferior a 10 Hz) através de fontes artificiais de corrente, como baterias e geradores, que alimentam uma unidade transmissora de corrente, denominada eletrorresistivímetro. Este equipamento é então inserido no solo por meio de dois eletrodos A e B, conhecidos como eletrodos de corrente. As diferenças de potencial resultantes são posteriormente medidas na superfície através de dois eletrodos M e N, chamados de eletrodos de potencial. O propósito fundamental é estimar a distribuição de resistividade da subsuperfície em diversas profundidades de investigação. De acordo com Orellana (1972), o valor registrado dessa diferença de potencial e da corrente associada está relacionado com a resistividade aparente do solo e com o arranjo geométrico dos eletrodos, sendo a profundidade de investigação diretamente proporcional ao espaçamento entre os eletrodos de corrente.

Os valores de resistividade são predominantemente influenciados pela composição, porosidade, teor de água e quantidade de sais dissolvidos. Segundo Braga (2006) e Costa (2008), a porosidade é o fator determinante da resistividade em rochas, geralmente aumentando conforme a porosidade diminui. Tipicamente, os valores de resistividade tendem a diminuir com o aumento da saturação nos poros, pois a água contida nesses poros contém sais dissolvidos, facilitando o fluxo elétrico devido à sua baixa resistividade. Além disso, as fraturas e fissuras na matriz da rocha também reduzem os valores de resistividade, pois proporcionam caminhos para a infiltração de água e alterações na rocha.

Para a investigação em subsuperfície, dois procedimentos são os mais utilizados: SEV (Sondagem elétrica vertical) e CE (Caminhamento elétrico). Para o desenvolvimento desta pesquisa, foi utilizado a técnica da sondagem elétrica vertical, que consiste em uma sucessão de medidas efetuadas, a partir da superfície do terreno, mantendo-se uma separação crescente entre os eletrodos de emissão de corrente e recepção de potencial. O modelo geoelétrico obtido é atribuído ao ponto central do arranjo, que permite observar a variação das camadas geológicas naquele ponto em profundidade. Da mesma forma, permite a utilização de diferentes arranjos de campo, onde nesta pesquisa utilizou-se o Arranjo Schlumberger (Figura 2.4).

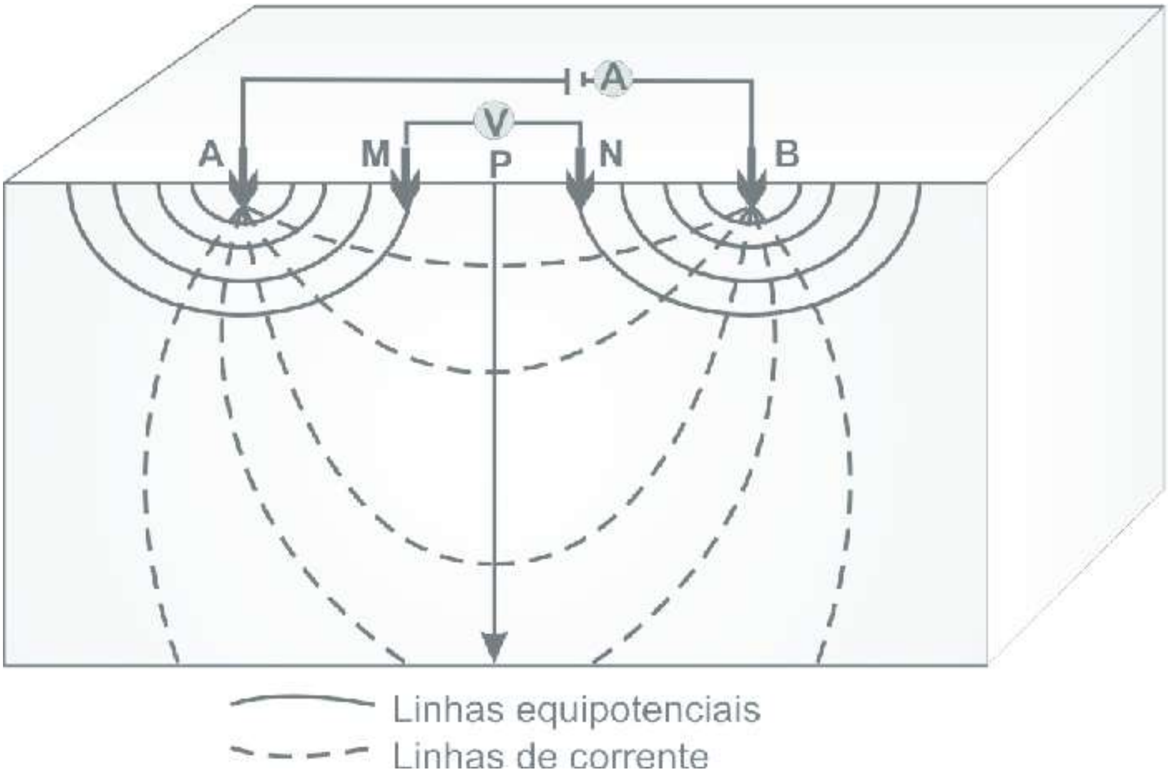

Figura 2.4 – Arranjo de aquisição do método Schlumberger (Modificado de Braga, 2006).

A técnica da sondagem elétrica vertical consiste, basicamente, na análise e interpretação de um parâmetro físico, obtido a partir de medidas efetuadas na superfície do terreno, investigando, de maneira pontual, sua variação em profundidade. O arranjo Schlumberger, além de ser mais prático no campo, sendo necessário o deslocamento de apenas dois eletrodos, as leituras nos equipamentos são menos sujeitas às interferências produzidas por ruídos indesejáveis.

Este arranjo é composto por uma configuração de eletrodos que consiste em quatro eletrodos: dois eletrodos de corrente (A e B) e dois eletrodos de potencial (M e N). A disposição desses eletrodos é essencial para a obtenção de dados precisos sobre a resistividade do subsolo.

O funcionamento básico do arranjo Schlumberger promove a injeção de corrente elétrica entre os eletrodos de corrente A e B. Essa corrente percorre o subsolo e é afetada pelas propriedades elétricas do material, incluindo resistividade, porosidade e saturação de água. As variações na resistividade do subsolo causam variações na distribuição de potencial entre os eletrodos de potencial M e N, que são então registradas e analisadas.

A chave para a eficácia do arranjo Schlumberger está na escolha adequada dos espaçamentos entre os eletrodos. O espaçamento AB, que é a distância entre os eletrodos de corrente, determina a profundidade de investigação do método, enquanto o espaçamento MN, que é a distância entre os eletrodos de potencial, influencia a resolução lateral dos dados. A relação entre esses espaçamentos e a profundidade desejada de investigação é crucial para a interpretação precisa dos resultados.

Ao aumentar a distância entre os eletrodos de corrente A e B, o volume total da subsuperfície incluída na medida também aumenta, permitindo alcançar camadas cada vez mais profundas. Os resultados sucessivos estarão, portanto, ligados com as variações das resistividades aparentes e/ou cargabilidades aparentes com a profundidade.

A profundidade de investigação de uma SEV é governada, principalmente, pelo espaçamento entre os eletrodos de corrente AB, podendo ser tomada como AB/4. Esta profundidade é definida como uma profundidade teórica investigada, pois, dependendo dos contrastes entre, por exemplo, as atividades das camadas geoelétricas, na prática, esta relação pode ser alterada.

2.5. Upscaling

A representação geológica de um campo de petróleo pode conter milhões de células descrevendo detalhadamente as estruturas e tipos de rochas presentes na área de estudo (modelo completo, na malha fina), mas a simulação da produção de um modelo dessa grandeza pode requerer um tempo computacional enorme. Assim o modelo precisa ser reduzido para atender a essa demanda (modelo simplificado, na malha grossa). Uma das maneiras para resolver esse problema da escala é o *upscaling* do grid e das propriedades, onde se reduz a quantidade de células unindo-as e recalculando as propriedades das novas células através de médias, métodos numéricos ou outros meios, onde os cálculos matemáticos vão substituir a descrição detalhada do modelo, de forma que as propriedades sejam equivalentes (Figura 2.5). Assim, fica mais viável de ser resolvido o processo de simulação computacionalmente.

Quando se utiliza técnicas geoestatísticas na modelagem numérica, os modelos deveriam utilizar a mesma escala onde foram obtidas as medições das propriedades petrofísicas (RENARD & DE MARSILI, 1997). Contudo, normalmente estas medidas são obtidas em ensaios laboratoriais ou perfis de poços, que possuem uma resolução centimétrica, enquanto os grids normalmente utilizados na modelagem de reservatório possuem células de dezenas a centenas de metros. Desta maneira, é necessário fazer uma mudança para uma escala mais ampla (RENARD & DE MARSILI, 1997). Em termos de propriedades que necessitam de *upscaling*, tem se a porosidade e permeabilidade usualmente utilizadas dentro dos modelos.

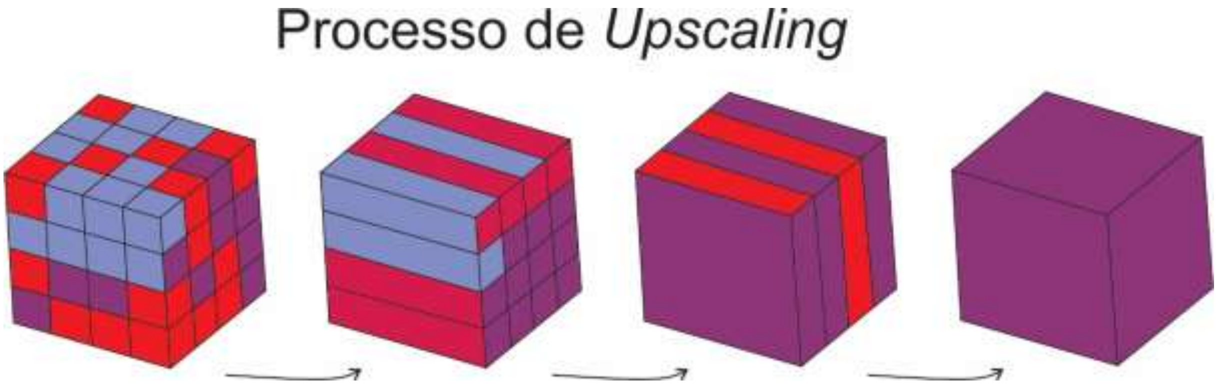

Figura 2.5 - Demonstração do princípio do upscaling de propriedades, onde no primeiro cubo se tem um modelo conceitual com vários elementos até chegar no ultimo com um elemento só e neste se tem valores médios das propriedades de todos os outros. Fonte: O autor.

A porosidade, apesar de bandas de deformação poder ser mais de uma ordem de magnitude menor que na rocha hospedeira, não altera significantemente o valor da porosidade total de uma rocha contendo bandas de deformação (QU et al., 2017). Assim, quando se constrói um modelo geológico, por várias vezes a redução que as bandas de deformação causam na porosidade não são representadas dentro modelo numérico. Ao se observar outra propriedade de grande importância na modelagem, que é a permeabilidade, tem se que a partir da mesma pode se obter uma permeabilidade equivalente durante o processo de *upscaling*, definida pelo tensor de permeabilidade constante, que representa um meio heterogêneo. Esta permeabilidade equivalente vai ser representada como sendo permeabilidade de uma porção da malha do modelo ou elemento, onde se tem várias técnicas para determinar a permeabilidade equivalente, sejam estas determinísticas, analisticas ou estocásticas. Um modelo muito utilizado é o de Cardwell-Parsons (1945), que tem como objetivo calcular as permeabilidades equivalentes utilizando um limite superior dado pelo cálculo da média harmônica das médias aritméticas, e um limite inferior dado pelo cálculo da média aritmética das médias harmônicas, e por fim o uso da média geométrica considerando os dois limites. Obtém-se dois limites para o valor da permeabilidade: um valor mínimo pela média harmônica dos valores de permeabilidade de cada célula em uma dada camada seguida da média aritmética dos valores das camadas; e um valor médio pela média aritmética dos valores de permeabilidade de cada célula de uma dada coluna seguida da média harmônica dos valores das colunas. A permeabilidade equivalente seria um valor intermediário dada pela média geométrica dos dois limites calculados.

2.6. Modelagem e simulação

A modelagem de reservatórios consiste na aplicação de métodos matemáticos e computacionais para representar as características físicas e comportamentais de reservatórios. Esses modelos visam simular fenômenos complexos, como o fluxo de fluidos, a distribuição de pressão e a migração de componentes através das rochas porosas. A precisão dessas representações é essencial para otimizar a produção de petróleo, compreender o comportamento do reservatório ao longo do tempo e tomar decisões estratégicas informadas. A modelagem de reservatórios incorpora dados geológicos, propriedades dos fluidos e informações de poços para criar simulações realistas que orientam o desenvolvimento de estratégias de recuperação eficientes. Avanços contínuos nessa disciplina são fundamentais para enfrentar os desafios complexos associados à extração de petróleo.

A construção desses modelos pode ser utilizada para analisar as variações petrofísicas e estruturais que afetam o fluxo de fluidos em meios porosos, dentre elas as existentes em zonas de falhas compostas por bandas de deformação (ALABERT; AQUITAINE; MODOT, 1992; SEIFERT E JENSEN, 2000). Os reservatórios deformados são caracterizados por apresentar uma distribuição heterogênea entre porosidade e permeabilidade. Geralmente, a matriz rochosa apresenta altos valores de permeabilidade e a rede de estruturas deformacionais apresentam, em geral, baixa permeabilidade. Quando se trabalha com reservatórios nesta configuração, o fluxo de fluido no reservatório, de maneira geral, depende fortemente das propriedades destas redes, que nesse estudo é observado a presença das bandas de deformação.

Conforme se tem o avanço na modelagem e simulação de bandas de deformação, tem se a necessidade da incorporação de elementos arquiteturais que fazem parte da estrutura da rocha. Inserção de bandas de deformação em zonas de dano é algo complexo, pois simuladores comerciais permitem a introdução das características sedimentológicas das formações de reservatórios ou aquíferos em seus modelos. Contudo as características estruturais não são, por muitas vezes, consideradas nas simulações hidráulicas (TVERANGER et al., 2004; ROTEVATN et al., 2009).

As bandas de deformação estão comumente presentes em rochas porosas. Por serem estruturas de espessuras variando de milímetros a pouco centímetros, sua incorporação em modelos de simulação tem uma complexidade maior. O custo computacional é alto, haja visto que é necessária toda uma construção de uma malha com elementos refinados para discretizar o domínio em que a banda está inserida. Alem disso, em subsuperfície, tal detalhamento é impossível de se realizar devido ao caráter subsismico dessas estruturas. Assim, a realização de simulações considerando a presença das bandas requer um tempo de execução longo, tornando inviável sua inserção em modelos de escala de reservatório (SILVA et al., 2022). Os modelos habituais tridimensionais representam as falhas como uma descontinuidade no modelo, reproduzindo sua posição e rejeito, sem alteração das propriedades dessa região do modelo, como realçado por Tveranger et al. (2005). Contudo, as propriedades de fluxo podem mudar de acordo com as características dos elementos arquiteturais (núcleo, zona de dano e protólito) que compõem as zonas de falha, podendo representar uma barreira ou conduto ao fluxo de fluidos (CAINE; EVANS; FORSTE, 1996; TVERANGER et al., 2005; SILVA et al., 2022). Assim, as variações de propriedades das zonas de falha devem ser incorporadas aos modelos de propriedades (Figura 2.6).

Ao longo do tempo, diversos autores (FACHRI et al., 2013; QU et al., 2015; QU & TVERANGER, 2016; QU et al., 2017; STOHLER et al., 2021; SILVA et., 2022) realizaram pesquisas com o intuito de solucionar os problemas advindos da não representação dos impactos causados pela presença dessas estruturas na zona de dano, que, por diversas vezes não são considerados no momento da modelagem e simulação.

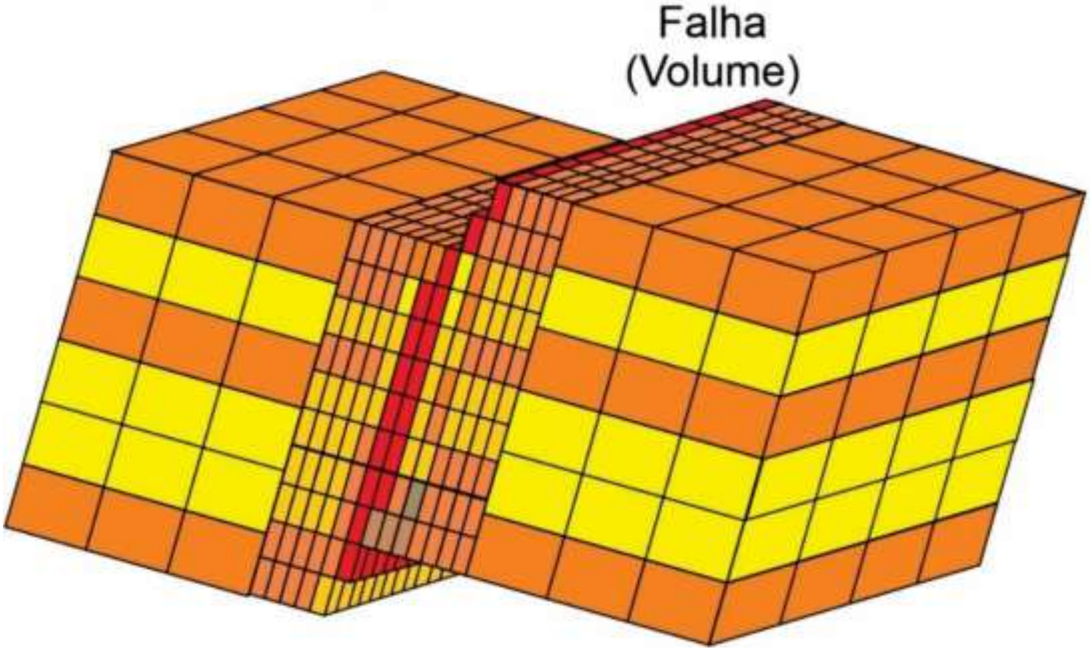

Figura 2.6 - Demonstração do modelo geológico onde a zona de falha é considerada como volume (SILVA et al., 2022).

Para modelagens mais fidedignas, utiliza-se a técnica de *Discrete Fracture Network (DFN)*, onde as bandas de deformação são representadas de maneira espacialmente explicita por meio do método de elementos finitos. O volume do reservatório é representado por elementos triangulares, para representação 2D, e quadriláteros, para representação 3D. Este volume é preenchido por bandas representadas através de elementos lineares, na representação bidimensional, e planos, para representações tridimensionais (LEI, 2017; HARTLEY & ROBERTS, 2013).

Em relação a geração de modelos mais robustos em que ao final de sua construção é realizada a inserção de poços injetores e produtores, é necessário adaptações e considerações que tornem o modelo com um custo computacional compatível com as simulações de fluxo a serem realizadas. Assim, diversos autores (SYVERSVEEN et al., 2006; FACHRI et al., 2013; FACHRI; ROTEVATN; TVERANGER, 2013; QU; TVERANGER, 2016; QU; TVERANGER; FACHRI, 2017; SILVA et al., 2022) introduziram em suas pesquisas um novo conceito, denominado de fácies de falha, que se utiliza de uma modelagem estocástica para construir modelos que envolvem varáveis aleatórias e assim possam prever comportamentos na simulação.

Esse método desempenha a individualização da zona de falha em objetos geológicos tridimensionais, baseado na caracterização estrutural das bandas de deformação, especificamente a intensidade de deformação em termos de quantidade de estruturas por unidade de metro (FACHRI; ROTEVATN; TVERANGER, 2013). A caracterização dessas fácies já foi efetivada de diversas maneiras, sendo estas: pela discretização de mapas de densidade (ou intensidade) de deformação obtidos em campo, que são individualizados em escalas de cores e associados às fácies de falha (FACHRI et al., 2013); pela expansão de uma pequena área de detalhe aonde as bandas foram mapeadas, transformando a espessura das bandas de três milímetros em três metros (ROTEVATN et al., 2017); e pela análise de linhas de varredura (scanlines) da zona de dano, obtidas em afloramento (QU; TVERANGER, 2016; SILVA et al., 2022). Durante o processo de caracterização das fácies de falha na zona de dano, fatores como tendência proporcional, relação espacial e continuidade são inseridos no processo. Tendo como pressuposto, as bandas são então distribuídas em classes, de acordo com a intensidade de deformação, e modeladas com um simulador orientado a objeto, onde este cria um modelo de representação de fenômenos de modelos reais (SILVA et al., 2022). Em seguida, valores de permeabilidade e porosidade são associados às fácies de acordo com a intensidade de deformação. A permeabilidade efetiva pode ser calculada pelo método da média harmônica, que associa os valores de permeabilidade e comprimento das bandas e da rocha hospedeira, para o comprimento de célula do modelo (FACHRI; ROTEVATN; TVERANGER, 2013; QU; TVERANGER, 2016). A porosidade efetiva, por sua vez, pode ser obtida através da média aritmética entre os valores de porosidade da rocha hospedeira e da banda (FACHRI; ROTEVATN; TVERANGER, 2013; QU; TVERANGER, 2016).

$$\emptyset e = \frac{\emptyset t}{\emptyset b}$$

Onde $\emptyset e$ é a porosidade efetiva; $\emptyset t$ a porosidade total e $\emptyset b$ a porosidade da banda.

A simulação permite com que se entenda o comportamento dinâmico do fluxo de fluidos nos meios porosos, otimizando assim os estudos realizados para alocação dos poços e cálculo do fator de recuperação. Entre os simuladores presentes no mercado atualmente, o simulador de linhas de fluxo (Figura 2.7) tem sido bastante usado para entender a relação entre injeção e produção, além de ser consideravelmente mais rápido do que os simuladores de fluxo padrão (SCHLUMBERGER, 2020). Com base nos parâmetros rocha-fluidos incorporados ao modelo construído, esse simulador origina linhas de corrente para representar o padrão de fluxo do modelo simulado, sendo obtidas pelo cálculo de pressão do reservatório (AL-NAJEM et al., 2013; SCHLUMBERGER, 2020), como também a construção de mapas de saturação e avanço do campo de pressão. Segundo PARENTE (2008), as linhas de fluxo representam o campo velocidade num determinado instante, não devendo ser confundidas com o conceito de trajetória de uma partícula. As linhas de fluxo variam com o tempo e indicam o posicionamento de todas as partículas naquele instante, simulando, assim, o movimento do fluido (PARENTE, 2008).

A simulação de fluxo de fluidos também tem sido uma importante ferramenta para investigar o impacto da zona de dano composta por bandas de deformação no desempenho do reservatório (ROTEVATN et al., 2009; QU; TVERANGER (2016); FACHRI et al., 2013; FACHRI et al., 2016; STOHLER, 2021). Syversveen et al. (2006) fizeram um comparativo entre a simulação com linhas de fluxo de um modelo de falha tradicional, com um modelo usando as fácies de falha para individualizar a zona de falha. Estes observaram que o fluxo na zona de falha será maior e mais espalhado quando aplicado o conceito de fácies de falha. Outra observação que foi realizada, é que a o fluxo vertical será controlado pelas fácies de falha.

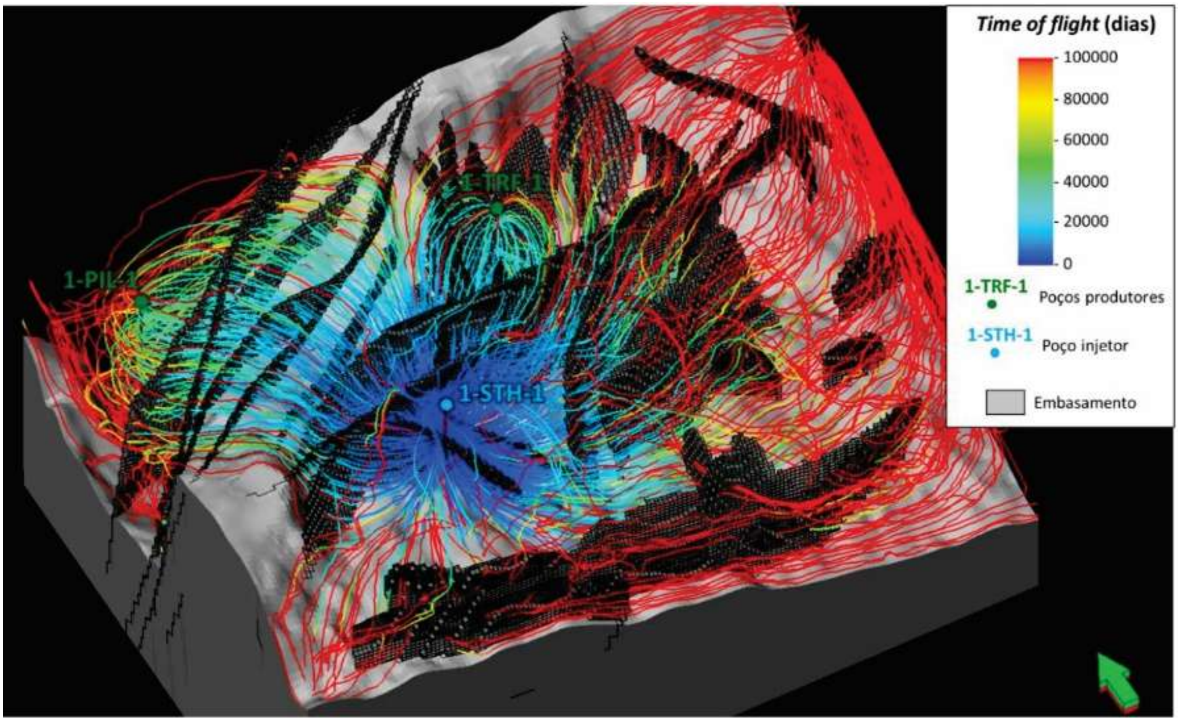

Figura 2.7 - Exemplo do simulador com a presença das linhas de fluxo (STOHLER 2021).

2.7. Referências

ALABERT, F. G.; AQUITAINE, E.; MODOT, V. Stochastic models of reservoir heterogeneity: Impact on connectivity and average permeabilities. Proceedings - SPE Annual Technical Conference and Exhibition, v. Sigma, p. 355–370, 1992

AL-NAJEM, A.; PIRAYESH, E.; SOLIMAN, M. Y.; SIDDIQUI, S. Streamlines simulation of barrier fracture as a novel water shutoff technique. Journal of Petroleum Exploration and Production Technology, v. 3, n. 4, p. 243–254, 2013.

ANTONELLINI, M. A.; AYDIN, A.; POLLARD, D. D. Microstructure of deformation bands in porous sandstones at Arches National Park, Utah. Journal of Structural Geology, v. 16, p. 941-959, 1994.

BRAGA, A. C. O. Aplicação do método de eletrorresistividade na caracterização geológica e ambiental. São Paulo: Universidade Estadual Paulista (UNESP), 2006.

CAINE, J.S.; EVANS, J.P. & FORSTER, C.B. 1996. Fault zone architecture and permeability structure. Geology, 24(11): 1025-1028.

CARDWELL JR., W.T. & PARSONS, R.L. 1945. Average permeabilities of heterogeneous oil sands. Transactions of the AIME, 160(1): 34-42.

CHOI, J.; EDWARD, P.; KO, K. & KIM, Y. 2016. Definition and classification of fault damage zones: A review and a new methodological approach. Earth-Science Reviews, 152: 70-87.

COSTA, J. (2008). Aplicação da resistividade elétrica na investigação geológica e ambiental.
ENGELDER, J. T. Cataclasis and generation of fault gouge: Geological Society of American Bulletin, v. 85, p. 1515–1522, 1974.

FACHRI, M., TVERANGER, J., BRAATHEN, A. & SCHUELLER, S. 2013. Sensitivity of fluid flow to deformation-band damage zone heterogeneities: A study using fault facies and truncated Gaussian simulation. Journal of Structural Geology, 52: 60-79.

FACHRI, M.; ROTEVATN, A.; TVERANGER, J. Fluid flow in relay zones revisited: Towards an improved representation of small-scale structural heterogeneities in flow models. Marine and Petroleum Geology, v. 46, p. 144–164, 2013. Disponível em: http://dx.doi.org/10.1016/j.marpetgeo.2013.05.016

FOSSEN, H.; SCHULTZ, R.; SHIPTON, Z.K.; MAIR, K. Deformation bands in a sandstone e a review. Journal of the Geological Society. v. 164, p. 755-769, 2007.

FOSSEN, H.; BALE, A. Deformation bands and their influence on fluid flow. American Association of Petroleum Geologists Bulletin, v. 91, n. 12, p. 1685–1700, 2007.

FOSSEN, H. Geologia Estrutural. 1ª Edição. São Paulo: Oficina de textos. p. 566, 2010.

FOSSEN. H.; SOLIVA, R.; BALLAS, G.; TRZASKOS, B.; CAVALCANTE, C. & SCHULTZ, R.A. 2017. A review of deformation bands in reservoir sandstones: geometries, mechanisms and distribution. Geological Society, London, Special Publications, 459(1): 9-33.

FOWLES, J.; BURLEY, S. Textural and permeability characteristics of faulted, high-porosity sandstones: Marine and Petroleum Geology, v. 11, p. 608–623, 1994.

HARTLEY, L., ROBERTS, D., Summary of discrete fracture network modelling as applied to hydrogeology of the Forsmark and Laxemar sites. Svensk Kärnbränslehantering AB. AMEC, 2013.

LEI, Q., LATHAM, J-P, TSANG, C. F., The use of discrete fracture networks for modelling coupled geomechanical and hydrological behaviour of fractured rocks. Computers and Geotechnics. ScienceDirect, 2017.

NOGUEIRA, F. C.C.; NICCHIO, M. A.; BALSAMO, F.; SOUZA, J. A.B.; SILVA, I. V.L.; BEZERRA, F. H.R.; VASCONCELOS, D. L.; CARVALHO, B. R.B.M. The influence of the cataclastic matrix on the petrophysical properties of deformation bands in arkosic sandstones. Marine and Petroleum Geology, v. 124, n. November 2020, p. 104825, 2021. Disponível em: https://doi.org/10.1016/j.marpetgeo.2020.104825

ORELLANA, E. (1972). *Métodos geoelétricos aplicados a investigações do subsolo*

PARENTE, J. T. M. A. Otimização de vazão de poços injetores em projeto de injeção de água utilizando simulação por linhas de fluxo. 2008. 78 f. Dissertação (Mestrado) - Curso de Engenharia de Petróleo, Universidade Federal do Rio Grande do Norte, Natal, 2008.

PONTES, C.C; NOGUEIRA, F.C.; BEZERRA, F.H R.; BALSAMO, F.; MIRANDA, T.S.; NICCHIO, M.A.; SOUZA, J.A.B.; CARVALHO, B.R.B.M. Petrophysical properties of deformation bands in high porous sandstones across fault zones in the Rio do Peixe Basin, Brazil. International Journal of Rock Mechanics And Mining Sciences. p. 153-163. fev. 2019.

QU, D.; ROE, P. & TVERANGER, J. 2015. A method for generating volumetric fault zone grids for pillar gridded reservoir models. Computer & Geosciences, 81: 28-37

Qu, D. & TVERANGER, J. 2016. Incorporation of deformation band fault damage zones in reservoir models. AAPG Bulletin, 100(3): 423-443.

Qu, D.; TVERANGER, J. & FACHRI, M. 2017. Influence of deformation-band fault damage zone on reservoir performance. Intepretation, 5(4): SP41-SP56

RAWLING, G. C.; GOODWIN, L. B.. Cataclasis and particulate flow in faulted, poorly lithified sediments: Journal of Structural Geology, v. 25, p. 317–331, 2003.

RENARD, P. & DE MARSILY, G. 1997. Calculating equivalent permeability: a review. Advances in water resources, 20(5-6): 253-278.

ROTEVATN, A.; TVERANGER, J.; HOWELL, J.; FOSSEN, H. Dynamic investigation of the effect of a relay ramp on simulated fluid flow: Geocellular modelling of the delicate arch ramp, utah. Petroleum Geoscience, v. 15, p. 45–58, 02 2009.

ROTEVATN, A. FOSSMARK, H. S.; BASTESEN, E.; THORSHEIM, E.; TORABI, A. Do deformation bands matter for flow? Insights from permeability measurements and flow simulations in porous carbonate rocks. Petroleum Geoscience, v. 23, n. 1, p. 104–119, 2017.

SAILLET, E. La localisation de la déformation dans les grès poreux: Caractérisation d'un analogue de réservoir gréseux et faille dans le Bassin du Sud-Est, Provence, France: Ph.D. thesis, Nice–Sophia Antipolis University, Nice, France, p. 272, 2009.

SEIFERT, D.; JENSEN, J. L. Object and pixel-based reservoir modeling of a braided fluvial reservoir. Mathematical Geology, v. 32, n. 5, p. 581–603, 2000

SILVA, M. E.; NOGUEIRA, F. C.C.; PÉREZ, Y.A.R.; VASCONCELOS, D. L.; STOHLER, R. C.; SANGLARD, J. C.D.; BALSAMO, F.; BEZERRA, F. H.R.; CARVALHO, B. R.B.M.; SOUZA, J. A.B. Permeability modeling of a basin-bounding fault damage zone in the Rio do Peixe Basin, Brazil. Marine and Petroleum Geology, v. 135, p. 1-22, 2022.

STERNLOF, K. R.; CHAPIN, J. R.; POLLARD, D. D.; DURLOFSKY, L. J. Effective permeability in sandstone containing deformation band arrays: AAPG Bulletin, v. 88, p. 1315– 1329, 2004.

STOHLER, Rômulo de Campos. Modelagem numérica 3D do impacto de bandas de deformação no escoamento em meio poroso. Rio de Janeiro, 2021. xix, 204 f. Dissertação – Programa de Pós-graduação em Geologia, Instituto de Geociências, Universidade Federal do Rio de Janeiro, 2021.

SYVERSVEEN, A. R.; SKORSTAD, A.; SOLENG, H.H.; RØE, P.; TVERANGER, J. Facies modeling in fault zones Introduction Fault Facies Workflow. n. September, 2006.

TORABI, A.; FOSSEN, H.; ALAEI, B. Application of spatial correlation functions in permeability estimation of deformation bands in porous rocks. Journal of Geophysical Research: Solid Earth, v. 113, n. 8, p. 1–10, 2008.

TORABI, A.; FOSSEN, H. Spatial variation of microstructure and petrophysical properties along deformation bands in reservoir sandstones. American Association of Petroleum Geologists Bulletin, v. 93, n. 7, p. 919–938, 2009.

TUECKMANTEL, C.; et al. Fault-seal prediction of seismic-scale normal faults in porous sandstone: A case study from the eastern Gulf of Suez rift, Egypt: Marine and Petroleum Geology, v. 27, p. 334–350, 2010.

TVERANGER, J.; SKAR, T.; BRAATHEN, A. Incorporation of fault zones as volumes in reservoir models. Bollettino di Geofisica Teorica ed Applicata, v. 45, p. 316–318, 01 2004.

TVERANGER, J.; BRAATHEN, A.;SKAR, T.; SKAUGE, A. Centre for Integrated Petroleum Research - Research activities with emphasis on fluid flow in fault zones. Norsk Geologisk Tidsskrift. v. 85, p-63-71, 2005.

Capítulo 3

Geologia Regional e Área de estudo

3. Contexto Geológico e Área de estudo

3.1. Contexto geológico

A BRP faz parte de um conjunto de bacias interioranas de pequeno a médio porte localizado no Nordeste do Brasil (MATOS, 1992; FRANÇOLIN et al., 1994; NOGUEIRA et al., 2004). Essa bacia está localizada no extremo Noroeste do Estado da Paraíba, ultrapassando a fronteira desse com o Estado do Ceará, e ocupando uma área de aproximadamente 1.315 m².

A BRP foi formada a partir da separação dos continentes Sul-Americano e Africano durante o Cretáceo Inferior (145–130 Ma) (FRANÇOLIN et al., 1994; DE CASTRO et al., 2007; NOGUEIRA et al., 2015; RAMOS et al., 2022; NICCHIO et al., 2022). O desenvolvimento dessa bacia se deu por tensões extensionais de direção N-S para NNE-SSW, que esta associada a fase sin rift I, enquanto a extensão de NW-SE ocorreu durante a fase sin rift II (NICCHIO et al., 2022). A direção de alongamento gradualmente mudou de NNE-SSW para NW-SE devido à rotação no sentido horário dos principais campos de estresse associados à fragmentação de Pangeia. (NICCHIO et al., 2022), que reativaram de maneira rúptil as zonas de cisalhamento Patos, Portalegre e Rio Piranhas, dando origem as falhas de borda da BRP (SÉNANT; POPOFF, 1991; MATOS, 1992; FRANÇOLIN et al., 1994; NOGUEIRA et al., 2015; RAMOS et al., 2022). A reativação rúptil dessas estruturas do embasamento controlou o desenvolvimento dos principais depocentros da BRP, que são descritos por três sub-bacias (FRANÇOLIN et al., 1994), do tipo semi-grábens, denominadas: Pombal, Sousa e Brejo das Freiras, controladas pelas falhas Rio Piranhas, Malta e Portalegre, respectivamente (FRANÇOLIN et al., 1994; DE CASTRO et al., 2007).

Em relação ao preenchimento sedimentar, Silva (2014) sugere que esta bacia é constituída por cinco formações, que foram depositadas em dois períodos distintos. Da base para o topo são as formações Pilões e Triunfo, depositadas no período Devoniano, constituindo o Grupo Santa Helena, e as formações Rio Piranhas, Sousa e Antenor Navarro, depositadas no período Cretáceo, que formam o Grupo Rio do Peixe (Figura 3.1). A Formação Pilões é formada predominantemente por siltitos e argilitos, laminados ou maciços, podendo conter camadas de arenitos finos a grossos, depositados em ambiente flúvio-deltáico (SILVA et al., 2014). A Formação Triunfo é composta predominantemente por arenitos grossos a conglomeráticos, mal selecionados, contendo arenitos subordinados, com granulometria variando de fina a média, depositados em ambiente flúvio-deltáico (SILVA et al., 2014). A Formação Antenor Navarro consiste predominantemente de conglomerados, arenitos, que variam de finos a grossos e camadas pelíticas intercaladas aos arenitos, encontradas em proporções menores, e depositados em ambientes fluviais entrelaçados e leques aluviais (CARVALHO, 2000). Por sua vez, a Formação Sousa é preenchida por pelitos, na sua maior parcela por folhelhos e siltitos, com arenitos finos e margas subordinadas, depositados em ambiente lacustre. Por fim, a Formação Rio Piranhas é formada por conglomerados e arenitos grossos, intercalados de siltitos e argilitos, depositados em ambientes de leques aluviais e ambientes fluviais entrelaçados influenciados pelas falhas de borda (CARVALHO, 2000).

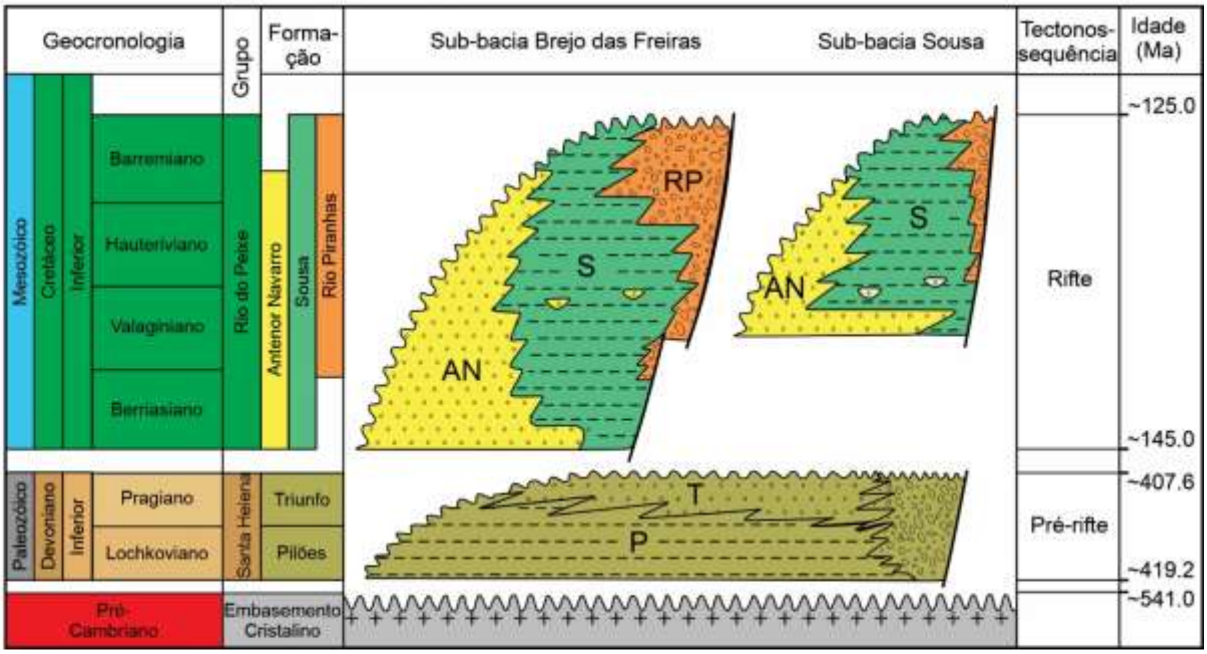

Figura 3.1. Carta estratigráfica da Bacia Rio do Peixe, modificada de Ramos et al., (2022). Legendas: AN (Formação Antenor Navarro), S (Formação Sousa), RP (Formação Rio Piranhas), T (Formação Triunfo) e P (Formação Pilões).

3.2. Localização

Para o desenvolvimento desta Tese de doutorado, foram estudados dois afloramentos na BRP (Figura 3.2A). O primeiro afloramento, informalmente denominado Melancias, que é descrito no paper publicado e anexado a presente tese, no capítulo 4 e resultados. O segundo afloramento, informalmente denominado Utah, foi descrito no segundo manuscrito submetido a *Geoenergy Science and Engineering*.

Ambos os afloramentos estao localizados próximo ao *Horst* de Santa Helena, um alto estrutural que delimita a Sub-bacia Brejo das Freitas da Sub-bacia Sousa. Estes afloramentos apresentam rochas compostas por arenitos conglomeráticos arcoseanos da Formação Antenor Navarro e possui bandas de deformação na forma de *clusters*, com exposição vertical de mais de dois metros de altura, além de bandas de deformação na forma de *single* (PONTES et al., 2019; DE SOUZA et al., 2021; TORABI et al., 2021). O Afloramento 2 encontra-se próximo a dois segmentos da Falha Portalegre (VASCONCELOS et al., 2021) com diferentes direções: NE-SW e EW, sendo este mais proximo do segmento norte da falha, diferente do afloramento 1 (Melancias) que fica mais proximo ao segmento sul (Figura 3.2B). Em adição, Pontes et al. (2019) classificou a deformação ocorrida nesse afloramento como uma *single fault zone*, a qual consiste em uma zona de falha comum único núcleo envolto por uma zona de dano. Torabi et al. (2021) classificou essa zona de falha como uma *deformation band fault zone*, que ao invés de apresentarem rochas de falhas em seu núcleo, apresentam clusters com bandas de deformação. A sua boa exposição lateral e vertical fez desse afloramento um excelente ponto de estudo para entendimento destas zonas que tem as bandas de deformação.

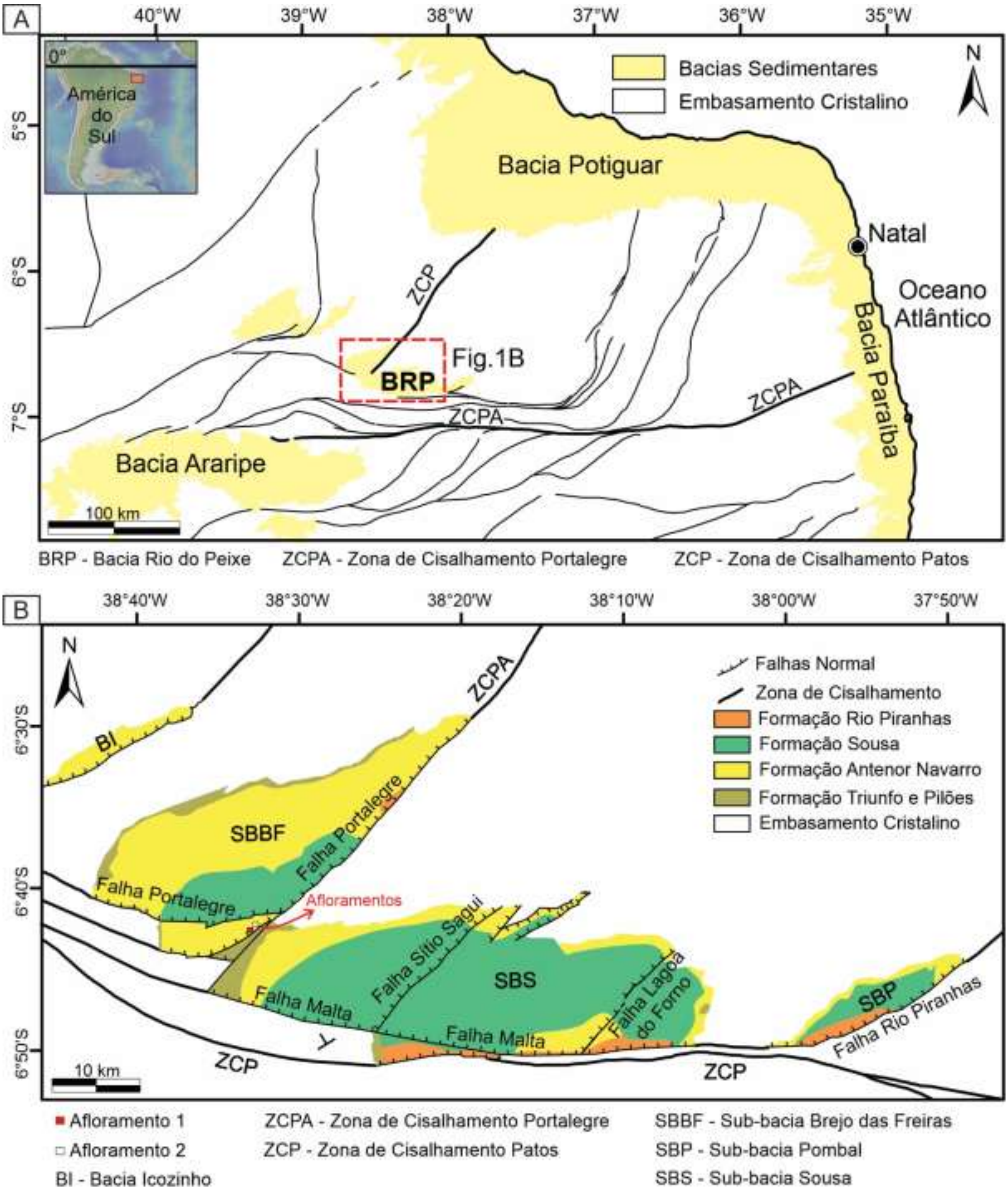

Figura 3.2. (A) Mapa de localização da área de estudo (Bacia Rio do Peixe) na região NE do Brasil. Adaptado e modificado de Françolin et al. (1994), Nogueira et al. (2015), Nicchio et al. (2018), Vasconcelos et al. (2021) e Freitas (2022).(B) Mapa geológico da Bacia Rio do Peixe onde se observa a localização da área de estudo (quadrado vermelho); as zonas de cisalhamento: Portalegre (ZCPA) e Patos (ZCP); as três falhas principais: Malta, Portalegre e Rio Piranhas; e as subbacias: Brejo das Freiras (SBBF), Sousa (SBS) e Pombal (SBP) (adaptado de Vasconcelos et al., 2021).

Referências

DE CASTRO, D. L. et al., 2007. On the tectonics of the Neocomian Rio do Peixe Rift Basin, NE Brazil: Lessons from gravity, magnetics, and radiometric data. Journal of South American Earth Science 24,184-202

FRANÇOLIN, J. B. L. et al., 1994. Faulting in the Early Cretaceous Rio do Peixe Basin (NE Brazil) and its significance for the opening of the Atlantic. Journal Structural Geology 16, 647-661.

MATOS, R. M. D. 1992. The Northeast Brazilian Rift System. Tectonics 11 (4), 766–791.

NOGUEIRA, F. C. C. et al., 2004.Estudo Magnético e Gravimétrico do Arcabouço Estrutural da Bacia Rio do Peixe – PB. Revista de Geologia 17, 74-87

NOGUEIRA, F. C. C. et al., 2015. Cretaceous intracontinental rifting and post-rift inversion in NE Brazil: Insights from the Rio do Peixe Basin. Tectonophysics 644- 645, 92-107.

PONTES, C.C; NOGUEIRA, F.C.; BEZERRA, F.H R.; BALSAMO, F.; MIRANDA, T.S.; NICCHIO, M.A.; SOUZA, J.A.B.; CARVALHO, B.R.B.M. Petrophysical properties of deformation bands in high porous sandstones across fault zones in the Rio do Peixe Basin, Brazil. International Journal of Rock Mechanics And Mining Sciences. p. 153-163. fev. 2019.

SENANT, J., POPOFF, M., 1991.Early Cretaceous extension in northeast Brazil related to the South Atlantic opening. Tectonophysics 198, 35-46.

SILVA, J. G. F. et al., 2014. Proposta de novas unidades litoestratigráficas para o Devoniano da Bacia do Rio do Peixe, Nordeste do Brasil. Brazilian Journal of Geology 44 (4), 561–578

TORABI, A; BALSAMO, F.; NOGUEIRA, F. C. C.; VASCONCELOS, D. L.; SILVA, A. C. E.; BEZERRA, F. H. R. SOUZA, J. A. B. Variation of thickness, internal structure and petrophysical properties in a deformation band fault zone in siliciclastic rocks. Marine and Petroleum Geology, v. 133, p. 1-24, 2021.

VASCONCELOS, D. L. et al., 2021. Tectonic inversion assessed by integration of geological and geophysical data: The intracontinental Rio do Peixe Basin, NE Brazil. Basin Research 33, 705-728

Capítulo 4

2D modeling and simulation of deformation bands' effect on fluid flow: Implications for hydraulic properties in siliciclastic reservoirs

This manuscript was published to Journal of Structural Geology on May, 2022 with https://doi.org/10.1016/j.jsg.2022.104581

4. 2D modeling and simulation of deformation bands' effect on fluid flow: Implications for hydraulic properties in siliciclastic reservoirs

Franklyn Macedo de Souza[a]; Igor Fernandes Gomes[a]; Francisco Cézar Costa Nogueira [b]; David Lino Vasconcelos[b]; Bruno Canabarro[a]; Jorge André Braz de Souza [c]; Leonardo José do Nascimento Guimarães[b] ; Leila Brunet Beserra[b]

[a] Civil Engineering Post-Graduation Program, Federal University of Pernambuco, Recife, PE, 50740-530, Brazil
[b] Federal University of Campina Grande, Campina Grande, PB, Brazil
[c] Petrobras Research Center (CENPES), Rio de Janeiro, Brazil

*Corresponding author, email: franklyn.msouza@gmail.com

Abstract

Deformation bands can influence fluid flow within reservoirs, mainly acting as flow barriers. This study aims to characterize deformation bands and evaluate the influence of these structures on fluid flow through 2D modeling and numerical simulation using the equivalent permeability tensor computed numerically through a flow-based upscaling procedure in siliciclastic reservoirs. To do so, we analyze arkosic sandstones of the Antenor Navarro Formation in the Rio do Peixe Basin, NE Brazil. The characterization of deformation bands involved: 1) acquisition of aerial imagery using a drone; 2) conducting direct field-based structural analysis along one scanline (frequency of deformation bands/m); and 3) collection of samples in the field to perform petrophysical (porosity and permeability) tests. After the characterization phase, we built a 2D geological model using the previously acquired parameters and performed a single-phase numerical flow simulation of water using finite element code. We simulated four different horizontal and vertical flow scenarios for both measured and exaggerated host rock permeability. Our structural analysis demonstrated that the deformation bands preferentially strike NE–SW, with secondary E–W– to N–S– orientations. Our petrophysical analysis showed that samples affected by deformation bands have lower porosity (by up to two orders of magnitude) and permeability (by up to four orders of magnitude) values than samples collected in the host rocks. The numerical fluid flow simulation allowed us to conclude that the deformation bands act as partial flow barriers where the hydraulic head can indicate the barrier effect intensity. Pressure drops between host rock regions separated by deformation bands reached values from 10 to 40%, depending on the fluid flow direction, especially for cases with a high contrast between the permeability values (three orders of magnitude) of the deformation bands and the host rock. The results of this study focus on the importance of contrasts in permeability measurements between deformation bands and host rocks, which could help to enhance understanding of the behavior of the deformation bands as partial fluid flow barriers, as well as their implications for hydraulic properties in deformed siliciclastic reservoirs.

Keywords: Deformation bands, Porous sandstones, Permeability, Porosity, 2D Modeling, Fluid flow.

4.1. Introduction

Deformation bands are subseismic brittle structures with tabular geometries that accommodate small shear offsets, occurring as either single structures or cluster zones (where slip surfaces can initiate), associated with the process of faulting in porous rocks and sediments (>15% porosity) due to grain rearrangement and strain softening, affecting the petrophysical properties of host rocks (Antonellini & Aydin, 1994; Shipton et al., 2005; Fossen et al., 2007; Torabi & Fossen, 2009; Ballas et al., 2015). Generally, deformation bands are described as barriers to fluid flow and often act as sealing zones for flow, particularly where clay is present (e.g., Pittman, 1981; Leveille et al., 1997; Lehner & Pilar, 1997; Foxford et al., 1998; Gibson, 1998; Childs et al., 2009; Braathen et al., 2009; Choanji et al., 2018). However, there are cases where deformation bands appear to enhance fluid flow (Parry et al., 2004; Balsamo et al., 2012; Bense et al., 2013), do not fully compartmentalize the reservoir (Medeiros et al., 2010; Qu & Tveranger, 2016), or behave as fractures, which can be sealing or act as fluid flow conduits if the bands develop slip surfaces (Zambrano et al., 2018).

The description of the spatial distribution of deformation bands in sedimentary units of high porosity is complex and varied, including uniformly distributed arrangements or more complex deformation band patterns, including conjugated, quadrimodal, and polymodal types (e.g., Aydin, 1978; Underhill & Woodcock, 1987; Healy et al., 2006, 2015). In addition to deformation band distribution, it is challenging to predict the distribution of faults with small length and displacement values (which can be associated with the localized occurrence of deformation bands) inside reservoirs. Two groups of factors influence the spatial distribution of deformation bands along fault zones (Antonellini et al., 1994; Fossen et al., 2005, 2007; Ballas et al., 2015; Torabi et al., 2020; Oliveira et al., 2022). The first comprises the internal factors of the host rock, such as the porosity, grain size, grain sorting, grain shape, mineralogy, lithification, and cementation. The second comprises external factors, such as the burial depth, tectonic regime, and the relationship between faults. Thus, it is crucial to understand the factors controlling the distribution of deformation bands, including the impact of tectonic evolution; this can provide data to make reservoir study models more robust, constrain fault distributions in reservoirs, and, ultimately, understand the impact these structures have on fluid flow. In addition, the description of the structural, geological, and petrophysical characteristics of brittle structures in reservoirs is of fundamental importance for evaluating fluid flow in porous media (Rotevatn et al., 2007; Rotevatn & Fossen, 2011; Ballas et al., 2015), reservoir rocks' fluid storage properties (Tueckmantel et al., 2012), and to identifying possible locations that may act as geological traps (Rotevatn et al., 2007; Rotevatn & Fossen, 2011; Torabi et al., 2013).

Furthermore, it is challenging to understand the parameters that characterize the geometry and density of faults and deformation bands, at meso and microscales, due to their scales being below seismic resolution limits (Fossen et al., 2005, 2017; Ballas et al., 2015) and the indirect nature of the methods typically used in reservoir characterization (i.e., seismic and well profiling). For this reason, several studies have used multi-scales of analysis (integrating seismic, well, and outcrop data) to analyze deformation bands and quantify reservoir porosity and permeability and, ultimately, achieve improved robustness of modeling and simulation of fluid flow in the reservoir (e.g., Schueller et al., 2013; Choi et al., 2016; Qu & Tveranger, 2016; Botter et al., 2017; Qu et al., 2017; Araujo et al., 2018).

Some of these studies suggest adopting a high-fidelity modeling approach that includes the exact measurements collected from the deformation bands in the field at a scale (i.e., millimeters to a few centimeters) that integrates more detail of the arrangement of existing deformation bands. On this basis, it is possible to calculate an equivalent permeability tensor, that allows upscaling from discrete models for homogeneous media and application of upscaled properties in simulation cells for larger-scale models. In addition, several studies address flow modeling in porous media, using discrete fracture networks (DFN) to represent discontinuities, whether conductive or barriers, as well as approaches used to determine the equivalent permeability for the replacement of discrete models (e.g., Falcão et al., 2018; Silva et al., 2021; Alvarez et al., 2022) and adoption of gridded fracture and dual-porosity models (e.g., Belayneh et al., 2006; Bourbiaux, 2010; Unsal et al., 2010; Moinfar et al., 2011), for example. However, to date, only a few studies have used DFN to model deformation bands (e.g., Antonellini et al., 2014; Flemisch et al., 2018; Pourmalek et al., 2021); these works have demonstrated the important influence of this type of structure in controlling fluid flow patterns for each problem analyzed.

Although several studies have addressed the impact of deformation bands on the petrophysical properties of host rocks (e.g., Fossen et al., 2007; Torabi & Fossen, 2009; Ballas et al., 2015), the impact of these structures on fluid flow using numerical simulations remains poorly understood. Furthermore, few studies have integrated petrophysical data collected in deformation bands and interband spaces (i.e., deformed host rock located between adjacent deformation bands) for fluid flow simulation and analyzed the pore pressure drop in different flow orientations (Rotevatn et al., 2009; Rotevatn & Fossen, 2011; Antonellini et al., 2014; Qu & Tveranger, 2016; Botter et al., 2017). Thus, in this context, several key questions remain poorly understood: (1) What are the most important structural aspects to consider when simulating fluid flow in siliciclastic reservoirs? (2) How is fluid flow influenced by petrophysical property contrasts between deformation bands and the host rocks in siliciclastic reservoirs? (3) When do deformation bands compartmentalize fluid flow in siliciclastic reservoirs? (4) What factors should be analyzed in equivalent permeability studies?

In this study, we use a field study to characterize the deformation bands in an outcrop of the Antenor Navarro Formation, Rio do Peixe Basin (RPB), northeastern Brazil (Figure 4.1A); in addition, we use numerical simulation to evaluate the influence of these structures on fluid flow through equivalent permeability tensors by a flow-based upscaling procedure. Various recent studies have investigated deformation bands in the RPB (e.g., Araujo et al., 2018; Maciel et al., 2018; Nicchio et al., 2018; Pontes et al., 2019; de Souza et al., 2021; Nogueira et al., 2021; Torabi et al., 2021; Silva et al., 2022); however, none of these studies have directly quantified the role of the deformation bands in the hydraulic behavior of the RPB’s siliciclastic deposits. Our characterization involves collecting structural data using scanlines, acquiring Unmanned Aerial Vehicle (UAV) images for structural mapping, and collecting core plugs for petrophysical laboratory tests. A simulation model is then automatically constructed from the geological model to which a finite element fluid flow formulation is applied, including numerical calculation of the equivalent permeability tensor. The equivalent permeability tensor represents an important parameter in reservoir modeling because it considers the heterogeneity of a medium (Renard & De Marsily, 1997). When determining this property, we consider the host rock, deformation bands, and their attributes (i.e., intensity, thickness, petrophysics, direction, and topological pattern) in a continuous medium (Rotevatn & Fossen, 2011; Silva et al., 2022). A numerical Darcy experiment using a flow-based upscaling method modeled in an in-house finite element method FEM simulator was used to compute key (Olivella et al., 1996; Guimarães et al., 2007; Silva et al., 2021). In this simulation, we observed that the spatial arrangement of the deformation bands (e.g., orientation, dip, and three-dimensional configuration) strongly influences their fluid sealing potential and impacts the components of the equivalent permeability tensor. Furthermore, we verified a permeability contrast of one to two orders of magnitude between the host rock and deformation bands, with the equivalent permeability presenting components lower than those for the host rock values. However, the upscaled properties presented a considerable reduction for a case in which the permeability difference is three orders of magnitude. The increase of one order of magnitude in the permeability contrast between the deformation band sets and the host rock highlights the bands’ influence during water flow; these structures can act as barrier, thus partially compartmentalizing fluid flow.

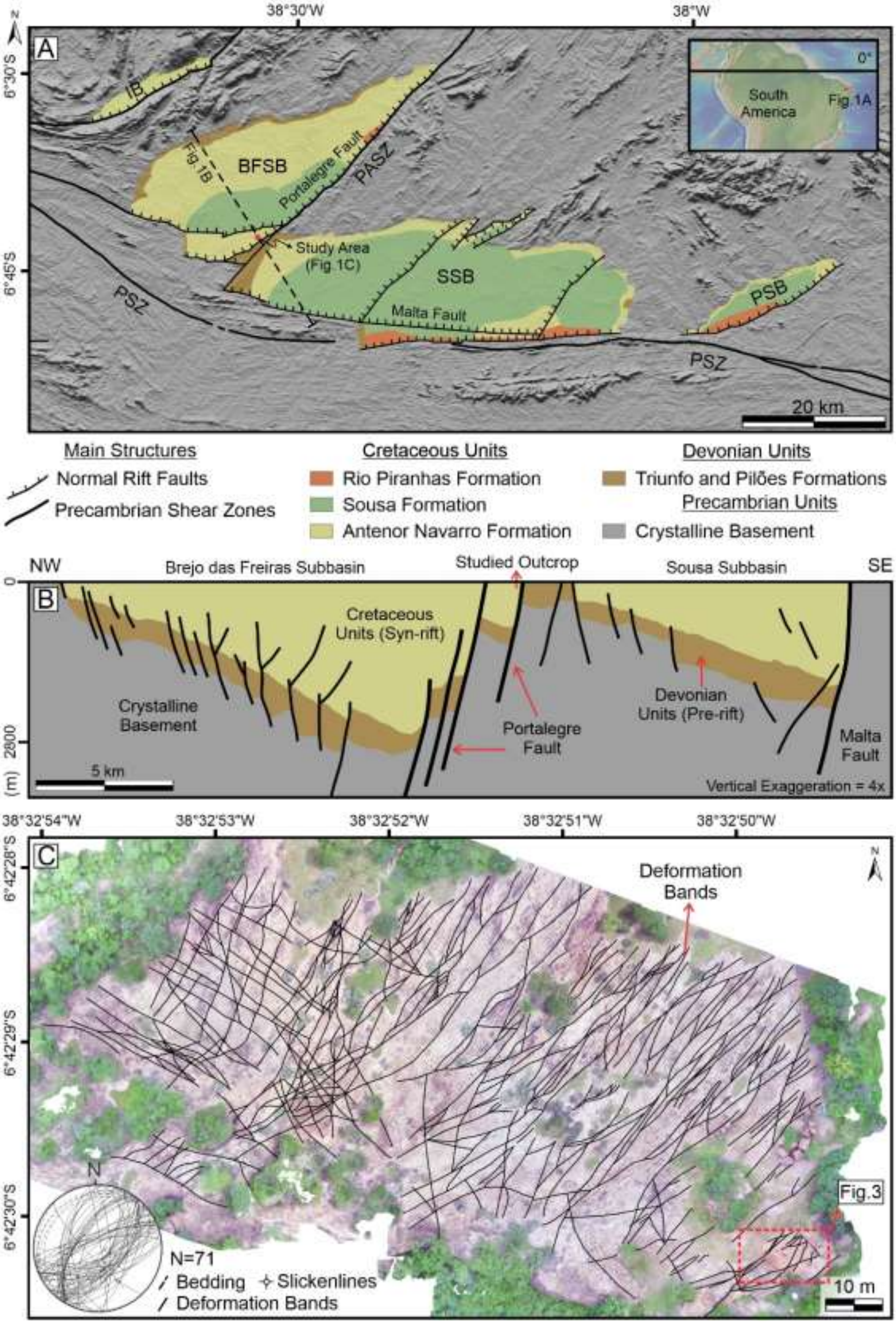

Figure 4.1. (A) Geological map of the Rio do Peixe Basin (RPB) showing the main structures bordering the basin and the main geological formations. (B) NW-SE-oriented geological profile of the Rio do Peixe Basin based on interpretation of a 2D seismic

section (adapted from Vasconcelos et al., 2021). (C) Drone image of the entire outcrop with traces of deformation bands (black lines; the area studied is shown by the red polygon). Stereonet (lower hemisphere of equal area net) showing the average orientation of deformation bands, slickenlines, and sedimentary bedding. N = number of measurements (adapted from Nogueira et al., 2021). Key: PSZ – Patos Shear Zone; PASZ – Portalegre Shear Zone; BFSB – Brejo das Freiras Sub-basin; SSB – Sousa Sub-basin; PSB – Pombal Sub-basin; IB – Icozinho Basin. The shear zones in the crystalline basement, rift faults in the RPB, sedimentary basins boundaries, and boundaries between the sedimentary formations were compiled from Françolin et al. (1994), Medeiros et al. (2005), Silva et al. (2014), Nogueira et al. (2015), and Vasconcelos et al. (2021).

4.2. Geological setting of the continental margin of northeastern Brazil

The interior basins of northeastern Brazil correspond to a relict set of sedimentary basins, originating from the filling of accommodation space generated during the rifting event that ultimately culminated in continental breakup and the separation of the African and South American continents (Ponte et al., 1991; Matos, 1992). The RPB is an example of these basins, consisting of a rift basin (Figure 4.1A), comprising three sub-basins, i.e., Brejo das Freiras (BFSB), Sousa (SSB), and Pombal (PSB), which are separated by crystalline basement horst blocks and controlled by activity along the regional tectonic structures called the Portalegre (NE–SW), Malta (E–W), and Rio Piranhas (NE–SW) faults, which control the geometry and depocenters of these sub-basins (Françolin et al., 1994; de Castro et al., 2007; Nogueira et al., 2015; Vasconcelos et al., 2021; Ramos et al., 2022).

The arrangement of pre-existing tectonic elements in the Precambrian basement has controlled the RPB’s structural framework (Sénant & Popoff, 1991; Lima Filho, 1991). According to several models proposed for the tectonic evolution of the interior basins, the RPB show a close relationship with the tectonic evolution of the passive margin basins (Françolin & Szatmari, 1987; Szatmari et al., 1987; Conceição et al., 1988; Sénant & Popoff, 1991; Ponte et al., 1991; Françolin, 1992; Françolin et al., 1994; Ponte & Ponte Filho, 1996; Matos, 2000). In this context, previous studies (e.g., Sénant & Popoff, 1991; Françolin et al., 1994; de Castro et al., 2007; Nogueira et al., 2015) have suggested that NW- to NNW-oriented extension controlled the opening of the RPB in the Early Cretaceous (from 145 to 130 Ma). Furthermore, mild to moderate tectonic inversion induced by far-field stresses from combined Andean compression and Mid-Atlantic Ridge-push effects partially changed the kinematics of the master bounding faults during the post-rift phase (ca. 80 Ma to present) in the RPB (Nogueira et al., 2015; Vasconcelos et al., 2021).

Within this tectonic context, the RPB is composed of three principal lithostratigraphic units: the Antenor Navarro, Sousa, and Rio Piranhas formations (Françolin et al., 1994; Lima Filho, 2001; Mendonça Filho, 2006); these units have interdigitated contacts, indicating some contemporaneity during their deposition in the Early Cretaceous (from 145 to 130 Ma). According to Nogueira et al. (2021), rocks of the Antenor Navarro Formation predominantly comprise poorly lithified, coarse-arkosic sandstones and fine conglomerates (~ 95% sand and gravel fractions and ~ 5% clay and silt fractions) with well-preserved sedimentary structures deposited in alluvial fans and fluvial braided systems. The Sousa Formation is characterized by a predominance of reddish shales and siltstone, which are locally grayish, with thin lenses of limestone, marl, and bodies of interspersed fine to coarse sandstone, deposited in a lacustrine system (Mendonça Filho, 2006). Françolin et al. (1994) report that the Rio Piranhas Formation comprises fine to coarse sandstones with cross-stratifications, interspersed with pelites deposited in alluvial fans and fluvial braided systems. This formation also contains coarse sandstones and disorganized matrix-supported conglomerates.

Additionally, Silva et al. (2014) proposed incorporating new sedimentary formations into the stratigraphic column of the RPB. Based on a combination of 3D seismic interpretation, well profiles, and lateral cores, in addition to constraints from previous palynological dating (Roesner et al., 2011), it was possible to identify the presence of Devonian sedimentary rocks. Silva et al. (2014) propose two new Devonian units: the Pilões Formation, composed of siltstone, claystone, light gray sandstone, and the Triunfo Formation, composed mainly of whitish-gray or hyaline sandstones, all of which belong to the Santa Helena Group. Recently, Vasconcelos et al. (2021) used field data and 2D seismic data to extend the occurrence of these Devonian units in the flexural border of the BFSB and SSB and throughout the base of the RPB.

We performed the present study in an outcrop located in the BFSB, a promising area for constraining the relationship between deformation bands, perm–porous characteristics, and integrated geological modeling in simulations. The RPB has become a common site for research involving deformation bands (e.g., Araujo et al., 2018; Maciel et al., 2018; de Souza et al., 2021; Oliveira et al., 2022; Silva et al., 2022), especially the Melancias outcrop (Figures 4.1B and 4.1C) (e.g., Nicchio et al., 2018; Pontes et al., 2019; Nogueira et al., 2015, 2021; Ramos et al., 2022). Previous studies have recorded a wide variety of deformation bands affecting the sandstones of the Antenor Navarro Formation, where it is possible to observe the distribution of the bands due to extensive exposures, including in 3D.

4.3. Methods

The characterization of the deformation bands involves the following main steps (Figure 4.2): 1) acquisition of aerial imagery using a drone; 2) carrying out structural analysis along one scanline (i.e., identifying the frequency of deformation bands per meter), performed directly in the field; 3) collecting core plugs in the field to perform petrophysical laboratory analysis (porosity and permeability); 4) construction a 2D geological model using previously acquired input parameters (structural and petrophysical); 5) performing a single-phase numerical simulation (water) using a finite element code for four scenarios of horizontal and vertical flow for measured and exaggerated host rock permeability values.

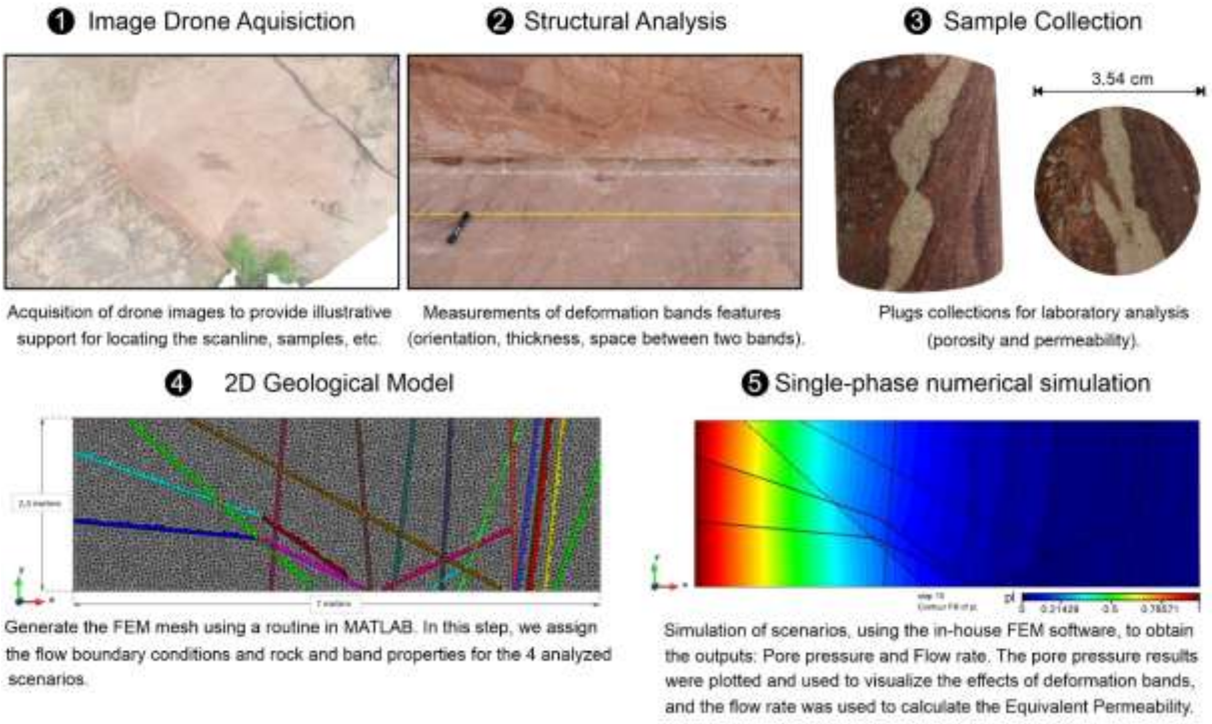

Figure 4.2. Simplified workflow used in this study with methodology steps: (1) Drone image acquisition; (2) Structural analysis; (3) Samples collection; (4) 2D Geological modeling; and (5) Single-phase numerical simulation.

4.3.1. Study area

The choice of the study area was based on three main points: (i) good outcrop accessibility due to adjacent state road; (ii) the strategic location of the outcrop within the basin between two fault zones (Araujo et al., 2018; Torabi et al., 2021; Vasconcelos et al., 2021); and (ii) the abundance of deformation bands due to fault zone complexity (Pontes et al., 2019; Nogueira et al., 2021) with excellent 3D visualization possible due to two cuts made in the outcrop, one on the lower floor and another on the wall, probably performed by the owner of the area (Figures 4.1C, 4.3, and 4.4). In addition, the outcrop presents a complex fault zone represented by several fault cores (Pontes et al., 2019), where several cataclastic deformation bands can be observed, which are oriented NE–SW, N–S, and E–W (Nicchio et al., 2018; Nogueira et al., 2015, 2021; Ramos et al., 2022).

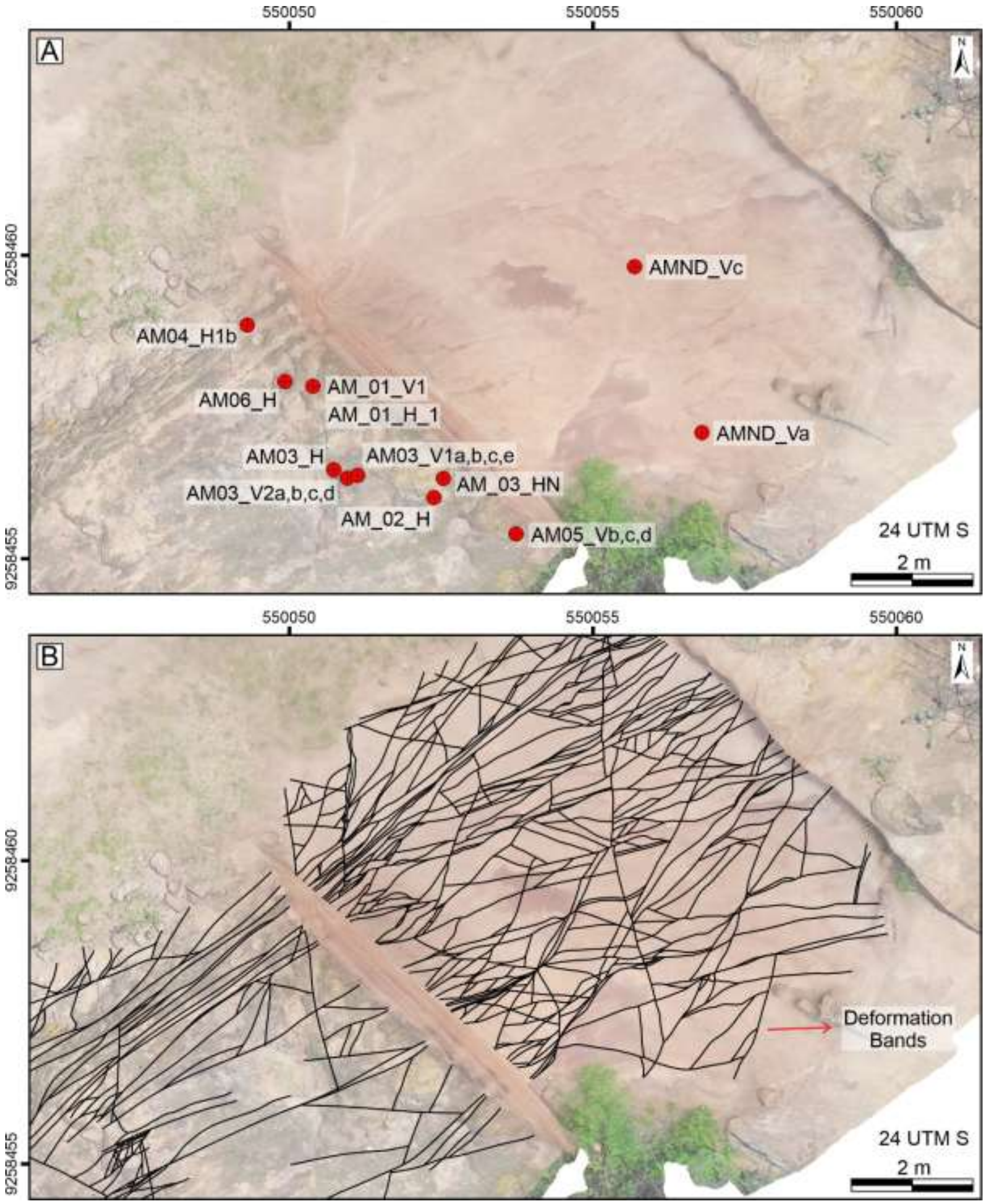

Figure 4.3. Drone image with a flat view of the area used in this study for building the geological model, indicating (A) the location of some samples (red circles) and (B) deformation bands (black lines) interpreted based on drone imagery highlighting the complex arrangement of these structures. Several deformation bands were not interpreted for improve clarity. Figure 4.1C presents the location of this image.

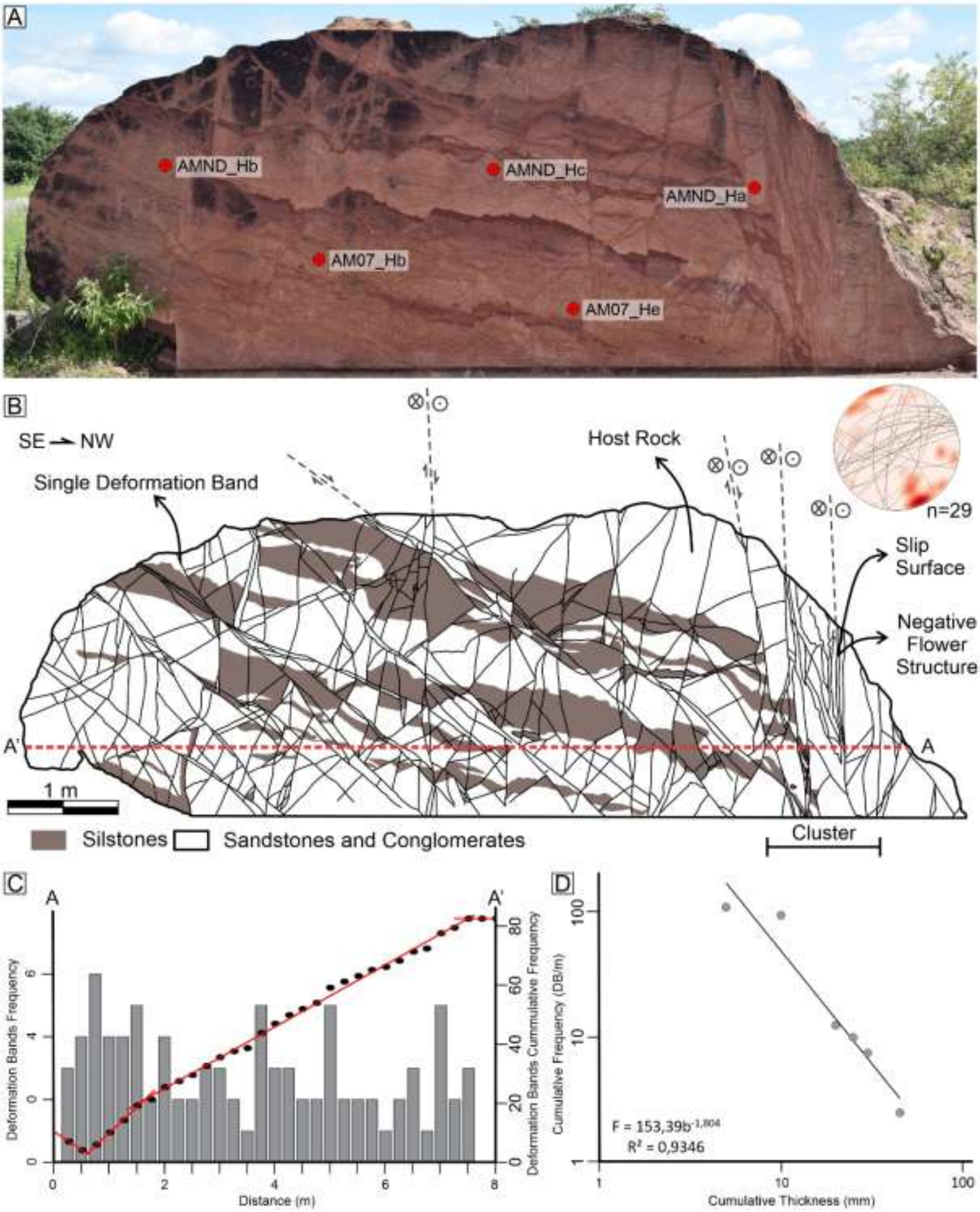

Figure 4.4. (A) Sandstones, conglomerates, and siltstones of the Antenor Navarro Formation in the Melancias outcrop wall selected for the geological model for flow fluid simulation, including the locations of some samples (red circles) not shown in Fig. 4.3 (B) Structural mapping of the Melancias outcrop wall (adapted from Nogueira et al.,

2021), with a stereonet (lower hemisphere equal area net) showing the orientation and kinematics of faults and contouring of the structural data collected in the studied outcrop wall. (C) Graph showing the frequency and cumulative frequency of deformation bands recorded in the scanline (dashed red line in Fig. 4.4B) along the outcrop wall. (D) Graph of the cumulative frequency of deformation bands per meter versus their cumulative thickness in millimeters. (For interpretation of the references to colour in this figure legend, the reader is referred to the Web version of this article).

4.3.2. Data acquisition

The field study aimed to collect structural data in the outcrop by investigating one detailed scanline. First, we acquired attributes related to deformation bands along the scanline, such as their spacing and orientation; a comparator ruler developed by Ortega et al. (2016) was then used to measure the thickness of the deformation bands. This ruler has values standardized on a logarithmic scale, with spacing values between 0.05 and 5 mm, thus enabling more precise measurements along the scanline.

4.3.3. Collection of high-resolution images and core plug samples

At this stage, we collected high-resolution images using a UAV to map the deformation bands present in the outcrop. After acquiring the images, we acquired plugs samples to perform petrophysical laboratory analysis of porosity and permeability of the deformation bands and host rock. Overall, we acquired 18 cylindrical samples (plugs) of 3.54 cm diameter using a motorized drill from the deformation bands and seven plug samples from the host rock, totalizing 25 plug samples. The plug collection strategy aimed to extract at least one expressive deformation band within each corresponding plug and no visible deformation bands in each host rock plug. To preserve the outcrop wall, we obtained the samples from blocks removed during the excavation of the outcrop and in the sub-horizontal exposure situated above the vertical outcrop's exposure. We took all possible care to carry out plug acquisition in the exact locations of the modeled deformation bands present in the outcrop.

4.3.4. Petrophysical analysis

The plugs used in the petrophysical analysis were of standard length (5 cm) and diameter (3.54 cm), with the faces rectified to accurately conduct measurements. The petrophysical properties (porosity and permeability) were measured using the UltraPoroPerm 500®, manufactured by Corelab. This equipment exhibits porosity and permeability measurement ranges of 0–40 porosity unit (%) and 0.001 to 20,000 mD, respectively. The porosity was calculated using the gaseous expansion method supported by a matrix cup under ambient pressure. The permeability was measured using a continuous gas flow supported by a core holder, with samples under confining pressure conditions ranging from 450 to 9,000 psi. For the analysis of this work, we used a confining pressure of 1,000 psi. After flow stabilization in the sample, we measured the pressure drop and flow. The permeability value was then calculated through the Darcy equation considering the viscosity of the gas used (nitrogen) and assuming single-phase, laminar flow.

4.3.5. Tomography

In addition, in one of the collected samples, a 3D image was performed using cone-beam X-ray microtomography to obtain reconstructed images of the plug with an effective pixel size of 61 µm. We utilized this information to calculate porosity values in the deformation bands and host rock of the core sample. Several previous works have implemented X-ray tomography to investigate deformation bands (e.g., Zambrano et al., 2017; Gambino et al., 2019; Awdal et al., 2020). First, the pixel size data was set up to calibrate the calculation; second, we selected the volume of interest (VOI) to calculate the porosity. Subsequently, a portion of the tomography volume was processed and transformed into a binary image (grayscale). From the grayscale calibration, it is possible to identify the total porosity of the material. The portion of voids, which are filled by air, is a less dense region that is represented in the grayscale image by darker tones. Higher density values correspond to lighter gray tones, which are classified as matrix or rock fragments. Accordingly, porosity values can be obtained within both the deformation band and host rock.

4.3.6. Scenarios for 2D numerical model based on outcrop data

We built a geological model of the mapped deformation bands using numerical code developed in MATLAB, which was then used as an input for fluid flow simulation with an FEM simulator. The model built and simulated in this study corresponds to the mapped outcrop wall (Figure 4.4).

The methodology was established based on detailed field-based mapping of deformation bands and integration of high-resolution images generated using a drone. We modeled the most representative deformation bands, i.e., the bands that crosscut the entire outcrop and are likely to exert more influence on the host rock petrophysical properties and fluid flow. However, we did not model all the deformation bands; instead, we based the selection parameter of the deformation bands used to build the model mainly on the continuity of the bands exposed in the wall section with the upper and lower portions of the outcrop. In this case, the thicker deformation bands are more easily identified in the upper and lower portions of the outcrop. Furthermore, we prioritized deformation bands where samples had been acquired for petrophysical analysis, as described above. In total, 17 structures were mapped, which were considered representative of the outcrop for modeling. Notably, as the outcrop has an irregular geometry, we opted to use a rectangular cut representing a compatible geometry for constructing a finite element mesh. A rectangle was constructed with dimensions of 2.3 x 7 meters as a representative fine-scale area within the coarser scale outcrop domain (i.e., meter-scale). The ends of the deformation bands were then extrapolated to the edges of the bands, maintaining all the rock properties and constructing the outcrop model.

The routine to delimit the geometry for the 2D geological model of the outcrop portion under study allows us to observe the arrangement of all the mapped deformation bands and their distribution. The generated finite element grid comprises linear triangular elements representing the entire studied 2D area, containing 46,164 elements and 23,427 nodes. This model represents the deformation bands with local refinement, representing the high fidelity of the proposed outcrop model.

For the model construction and mesh generation, we isolated the geometrical characteristics of the deformation bands (i.e., thickness, tip coordinates, and direction) by creating a domain for each band and assigning a specific material to them in a preprocessing stage. All relevant properties for the numerical analysis are specified in the material definition. We inserted the arithmetic mean thicknesses values for each system, as well as its orientation and position on the scanline. After this procedure, the petrophysical properties were applied to each model material as input parameters for numerical simulation. As the resolution was insufficient to specify the petrophysical properties for each sample in the geological model, we used the average porosity and permeability values obtained from the set of deformation band plugs collected in the field. Similarly, we used the average porosity and permeability values from the host rock samples for our geological model.

Four scenarios were studied, each using a unique model and FEM mesh; the difference between each scenario was the fluid flow direction and the host rock permeability (both the value measured in the field and a value one order of magnitude higher, i.e., 34.729 to 347.290 mD) with the aim of analyzing the effect of the contrast between the host rock and deformation bands. The numerical analysis considered the boundary conditions of the pressure gradient prescribed in opposite contours for the x- and y-directions in all scenarios. In scenarios 1.1 and 1.2, horizontal fluid flow (x-direction) was induced by applying a fluid pressure of 1 MPa in the left boundary of the domain, with a value of 0 MPa applied to the opposite boundary. Similar boundary conditions were considered for scenarios 2.1 and 2.2, except with vertical fluid flow (y-direction) from the bottom to the top of the cell. Scenarios 1.2 and 2.2 were simulated with the host rock permeability increased by one order of magnitude, aiming to constrain fluid flow behavior when there is a higher contrast between the deformation bands and the host rock. In this case, only the permeability was modified, and the new hydraulic behaviors were calculated in the horizontal and vertical directions. This approach was adopted due to the permeability results from the host rock in some cases showing values very close to the permeability values of the deformation bands.

4.3.7. Numerical simulation – fluid flow and equivalent permeability calculation

For a porous medium, the hydraulic problem is governed by the macroscopic fluid mass conservation equation that is constituted by the storage term (i.e., rate of change of the fluid mass through rock of porosity $\emptyset$ and fluid density ρ_l) and flux term defined by the divergent operator applied to Darcy's fluid velocity $\mathbf{q_l}$.

$$\frac{\partial}{\partial t}(\rho_l \emptyset) + \nabla \cdot (\rho_l \mathbf{q_l}) = 0 \qquad (1)$$

Where:

$$\mathbf{q_l} = -\frac{\mathbf{k}}{\mu_l}(\nabla p_l + \rho_l \mathbf{g}) \tag{2}$$

where $\mathbf{k}$ is the intrinsic permeability tensor, μ_l is the fluid viscosity, p_l is the fluid pressure and $\mathbf{g}$ is the gravity vector.

We performed a single-phase numerical simulation (water) considering a saturated porous medium using a finite element simulation that solves the fluid flow problem in porous media to calculate the section's equivalent global permeability in both horizontal and vertical directions. This analysis comprises a numerical upscaling approach called the flow-based upscaling process, as discussed in Durlofsky (2005), He & Durlofsky (2006), Falcão et al. (2018), and Silva et al. (2021). This approach determines an equivalent homogeneous medium from a high-fidelity heterogeneous porous medium, considering a high intensity of deformation bands. Accordingly, an equivalent permeability is calculated, and a homogeneous domain is defined.

The numerical test consists of reproducing Darcy's test, applying a pressure gradient on opposite sides of the domain, and measuring the flow rate when the flow reaches a steady state, which is defined as occurring when the average pressures of all nodes in the finite element mesh vary less than 0.001% in a time step. The scenario was simulated with fluid flow in the vertical and horizontal directions, and with the equivalent permeabilities calculated using the following relationship:

$$k_{eq} = \frac{\mu_l Q_n}{\rho_l L_n} \Delta p \tag{3}$$

where k_{eq} is the equivalent permeability of the section in the given direction, Q_n is the total nodal flow obtained on the outflow face in the finite element mesh, ρ_l is the fluid's specific mass, L_n is the section length perpendicular to the flow direction, and Δp is the fluid pressure difference applied to the outer faces of the mesh. Note that, in this study, we used an isotropic permeability tensor for the host rock material due to limitations in the petrophysical measurements of the samples plugs, which did not allow us to assess the directional permeability. Liquid pressure gradients control the fluid flow. The fluid density and viscosity are 1,000 kg/m^3 and 3.52x10^{-10} MPa.s, respectively.

4.4. Results

4.4.1. Structural characterization of the Melancias outcrop

The studied outcrop (Melancias) is close to the Portalegre Fault (Figure 4.1A) and consists mainly of coarse arkosic sandstones of the Antenor Navarro Formation (Figure 4.4A). The Melancias outcrop provides a 3D view including sub-horizontal and sub-vertical exposures of the deformation bands (Figure 4.1C). We performed our structural characterization in the vertical exposure (Figures 4.4A and 4.4B). The structures comprise mainly NE–SW and secondary E–W- and N–S-striking deformation bands with variable dips, ranging from 34° to sub-vertical (stereonet in Figure 4.4B), dominated by normal to right-lateral kinematics and millimetric to centimetric offsets (Figure 4.4B). In addition, the deformation bands present positive relief and complex geometry in the outcrop due to their anastomosing behavior (Figures 4.3, 4.4A, and 4.4B).

We detail the mapping of deformation bands in the outcrop wall along one scanline (Figure 4.4B). This scanline is approximately 8 meters long, with an average deformation band frequency of 11 band/m, with an average thickness of 11.59 mm. The cumulative thickness of the 88 bands along the 8 meters of the scanline is 1019.92 mm (Figures 4.4C and 4.4D). In addition, the thickness of the deformation bands follows a power-law distribution. However, in the extreme northwest of the outcrop wall, we report a cluster zone (Figure 4.4B) where the deformation band frequency increases to around 23 deformation bands/m (between 0.5 and 1.5 m in Figure 4C). Moreover, the deformation bands mapped on the outcrop wall exhibit continuity in the lower floor, where we observe right-lateral movements in the bands related to the negative flower structure.

4.4.2. Petrophysical characterization of the Melancias outcrop

We collected 25 samples for petrophysical analysis from the deformation bands and host rock (Figures 4.3 and 4.4). Overall, both porosity and permeability are higher in the host rock than in the deformation bands. For instance, the porosity measured in the samples collected within the deformation bands shows a reduction of up to one order of magnitude (mean value = 9.383%; standard deviation = 4.39%) relative to the porosity measured in the samples collected in the host rock (mean value = 23.438%;

standard deviation = 24.365%) (Figure 4.5A and Table 1). Similarly, the permeability measured in the samples collected within the deformation bands shows a reduction reaching four orders of magnitude (mean value = 0.657 mD; standard deviation = 0.946 mD) compared with the permeability measured in the samples collected from the host rock (mean value = 34.729 mD; standard deviation = 15.044 mD) (Figure 4.5B and Table 1). In addition, we evaluated the permeability–porosity relationship and found a positive correlation between the two factors (Figure 4.5C).

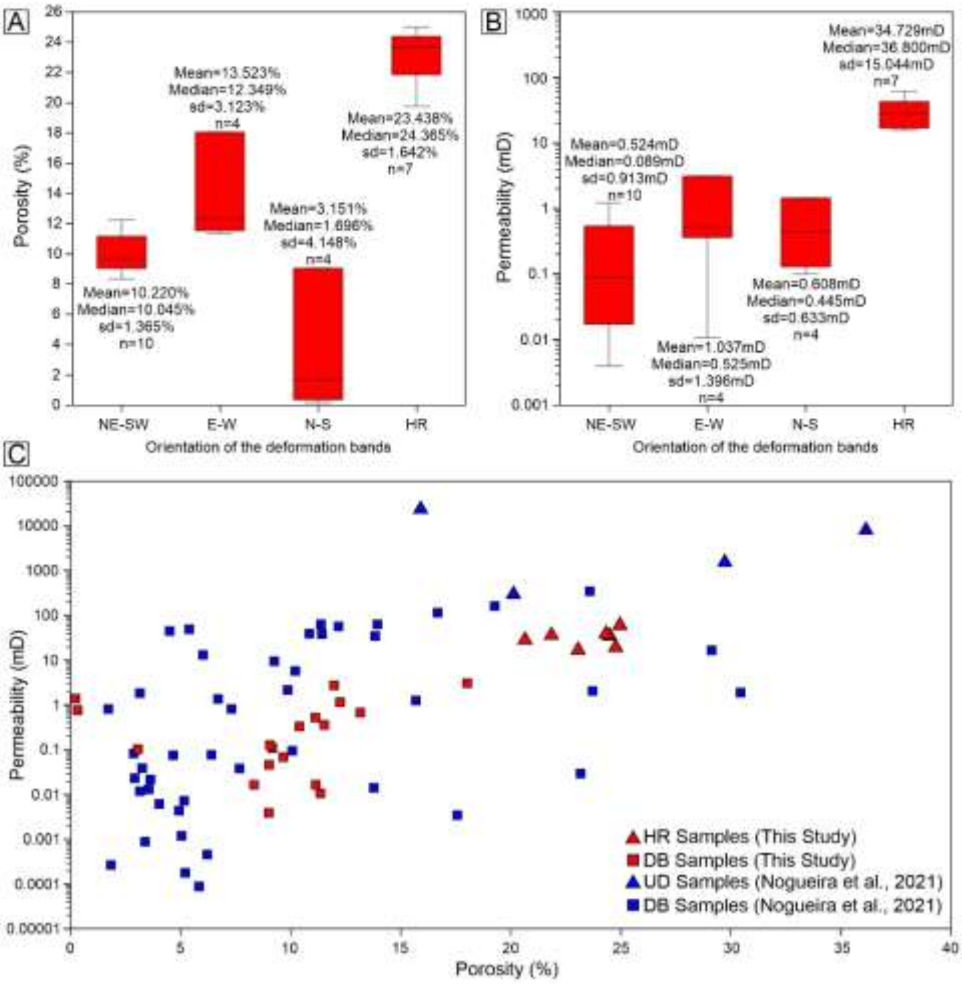

Figure 4.5. Graphs of the (A) porosity and (B) permeability distribution relative to the orientation of deformation bands from the database collected from the outcrop that was modeled and used for the calculation of fluid flow properties. The black line inside the red bars denotes the median, whereas the black lines in the top and base of the red bars indicate the maximum and minimum values, respectively. (C) Permeability–porosity relationship for all samples in this study and Nogueira et al. (2021). Key: HR

– Host Rock; DB – Deformation Band; UD – Undeformed (samples from pristine sandstones used by Nogueira et al. 2021).

Samples	Orientation of Deformation Bands	Porosity (%)	Permeability (mD)
AM05_Vb	E-W	18.044	3.090
AM05_Vc	E-W	13.168	0.689
AM05_Vd	E-W	11.529	0.360
AM06_H	E-W	11.349	0.010
AM03_HN	NE	9.184	0.110
AM03_V1a	NE	9.031	0.047
AM03_V1b	NE	9.008	0.004
AM03_V1c	NE	9.673	0.068
AM03_V1e	NE	8.348	0.017
AM03_V2a	NE	10.417	0.333
AM03_V2b	NE	12.241	1.220
AM03_V2c	NE	11.134	0.538
AM03_V2d	NE	11.993	2.890
AM04_H1b	NE	11.171	0.016
AM_01_H_1	N-S	9.054	0.129
AM_02_H	N-S	3.034	0.100
AM_03_H	N-S	0.357	0.761
AM_01_V1	N-S	0.158	1.440
AMND_Ha	HR	24.767	19.300
AMND_Hb	HR	24.979	60.400
AMND_Hc	HR	24.365	42.400
AMND_Va	HR	23.063	16.700
AMND_Vc	HR	24.369	39.700
AM07_Hb	HR	21.847	36.800
AM07_He	HR	20.676	27.800

Table 1. Petrophysical values (porosity and permeability) of three groups of deformation bands regarding their orientation (18 samples) and the host rock (7 samples). HR – Host Rock.

Furthermore, we analyzed the influence of different deformation band systems on the petrophysical properties. For this purpose, we classified the different samples by the orientation of their parent deformation band (Figure 4.5). For instance, relative to the whole deformation band population, the NE–SW-striking deformation band system maintains approximately constant porosity values, varying from 8.348 to 12.241%, with a mean value of 10.220% (Figure 4.5A), but shows a significant decrease in permeability, varying from 2.89 to 0.004 mD with a mean of 0.524 mD (Figure 4.5B). The N–S-striking deformation band system exhibits significant variability in its porosity values, including the lowest measured value for all samples analyzed, with a range from 0.158 to 9.054% and an average value of 3.151% (Figure 4.5A). In contrast, the permeability values are relatively consistent, ranging from around 1.44 to 0.1 mD with an average of 0.608 mD (Figure 4.5B). The E–W-striking deformation band system exhibits the highest porosity and permeability values of the three systems, varying from 11.349 to 18.044% and 3.09 to 0.01 mD, respectively, with corresponding averages of 13.523% and 1.037 mD (Figures 4.5A and 4.4B).

Finally, we analyzed the 3D porosity tomography (Figure 4.6) performed on one of the plug samples. The analyzed plug contains two deformation bands and host rock (Figure 4.6B). This analysis (Figure 4.6C) allowed us to identify that the individualized sub-volumes inside the core of the two deformation bands (DB in Figure 4.6D) show porosity values of 0.69–1.25%. Further away from the core of the deformation band, the porosity values identified were 1.52% and 6.54% for the host rock (HR in Figure 4.6D).

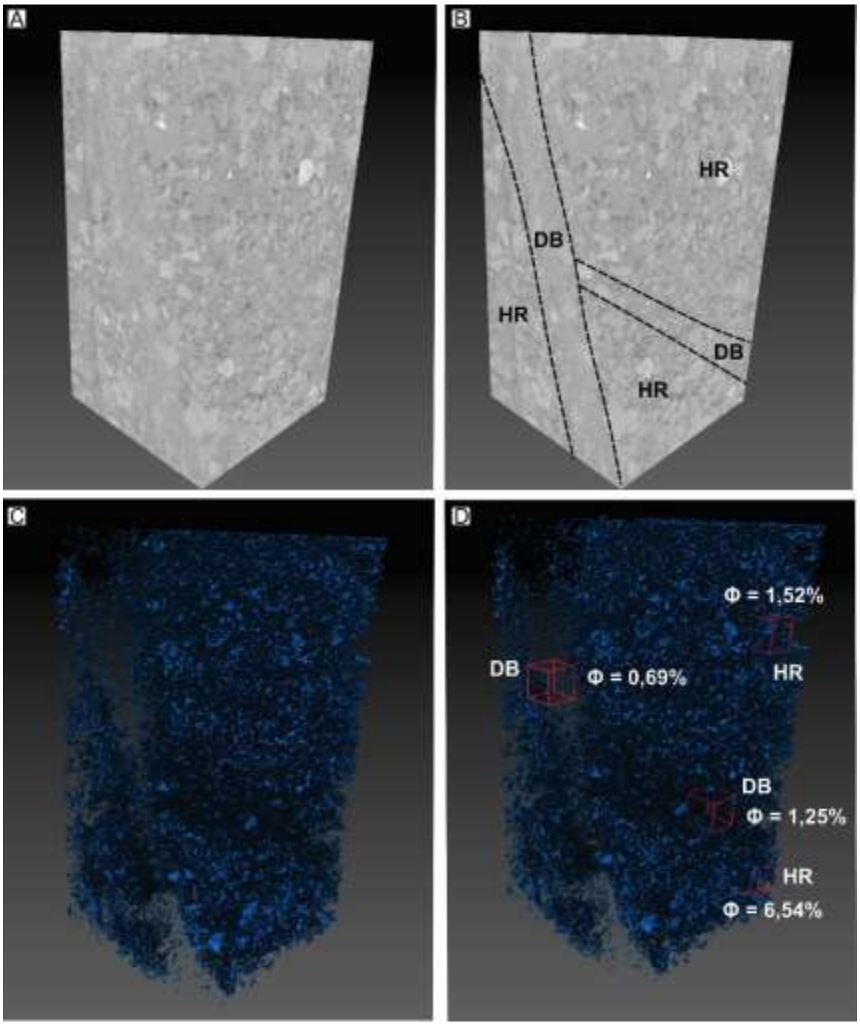

Figure 4.6. Tomography performed on an arkosic sandstone sample of the Antenor Navarro Formation. In (A), we present the entire matrix, and in (B) the boundary of the two deformation bands present in this sample is shown. In (C), we show the binarization process, illustrating the sample's pores (blue area) and demarcating the region where the deformation band is present. In (D), we illustrate the areas analyzed and the 3D porosity values for the core of two deformation bands (DB) and the host rock (HR).

4.4.3. Modeling the Melancias outcrop

We selected the most expressive deformation bands to construct a geological model of the Melancias outcrop. Accordingly, 17 deformation bands (numbered 1 to 17 in Figures 4.7A and 4.7B) were considered more expressive and chosen for the geological model. The model was generated by a finite element grid (Figures 4.7C and

7D), which contains linear triangular elements representing the Melancias outcrop wall, containing 46,164 elements and 23,427 nodes, in a domain 2.3 x 7 meters in size.

The deformation bands modeled are represented using local structural refinement, where they represent the proposed outcrop model with high fidelity. Several aspects were included in the deformation band modeling. For example, we detailed the average thickness of each deformation band system relative to its orientations based on our field measurements. The specific average thickness values utilized in our modeling were (Table 2): (1) 10.6 mm for the NE–SW-striking deformation band system; (2) 5.0 mm for the N–S-striking deformation band system; and (3) 11.3 mm for the E–W-striking deformation band system. Likewise, we also used average porosity and permeability values (Figure 4.5) for the different deformation band systems in relation to their orientations. We chose the arithmetic mean because it considers all the sample data collected, more fully representing the region under study. The specific porosity and permeability values utilized in our modeling were (Table 2): (1) 10.220% and 0.524 mD for the NE–SW-striking deformation bands system; (2) 3.151% and 0.608 mD for the N–S-striking deformation bands system; (3) 13.523% and 1.037 mD for the E–W-striking deformation band system; and (4) 23.438% and 34.729 mD for the host rock.

Orientation of Deformation Bands	Porosity (%)	Permeability (mD)	Average thickness (mm)
NE	10.220	0.524	10.6
E-W	13.523	1.037	11.3
N-S	3.151	0.608	5.0
Host rock	23.438	34.729	-

Table 2. Characteristics used in the outcrop model include the petrophysical properties and thickness for the three families of deformation bands and the host rock.

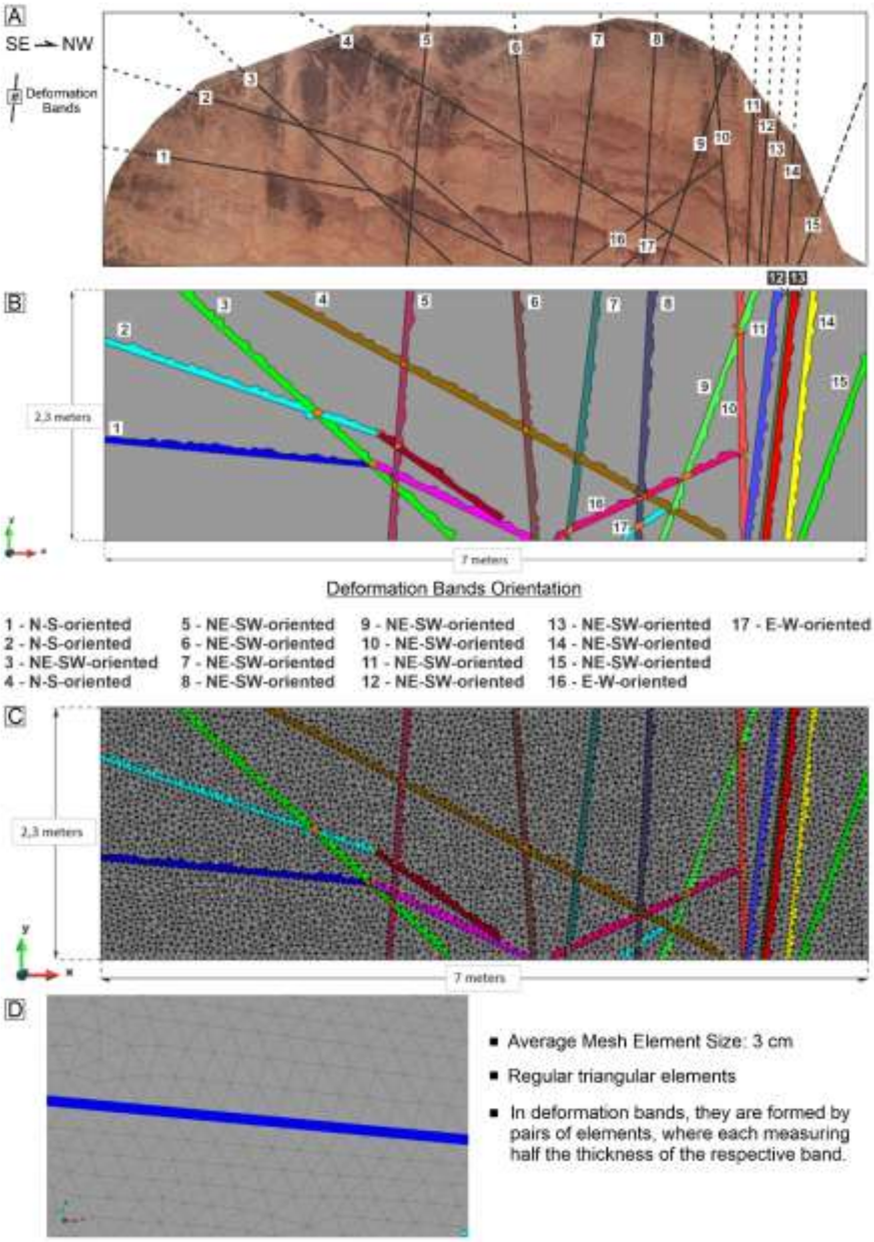

- Average Mesh Element Size: 3 cm
- Regular triangular elements
- In deformation bands, they are formed by pairs of elements, where each measuring half the thickness of the respective band.

Figure 4.7. (A) Outcrop wall image showing the location of the main deformation bands (black lines) mapped and extrapolated to build the geological model of the Melancias outcrop. (B) Configuration of the model generated for the outcrop showing the respective identified bands and (C) finite element mesh generated for the geological model of the Melancias outcrop. (D) Model details, including the triangular finite elements used to model the deformation bands (blue area) and the host rock (grey area). Note that the deformation bands are not shown at true thickness scale for a better visual representation.

4.4.4. Fluid flow simulation of the Melancias outcrop model

After creating the FEM mesh of the wall of the Melancias outcrop, we performed four scenarios for a single-phase numerical test (water)as discussed above. We used a finite element simulator that solves the problem of fluid flow in porous media and calculates the equivalent global permeability of the section in both horizontal and vertical directions. We applied a gradient pressure of 1 and 0 MPa to the boundaries of the geological model relative to the direction of the fluid flow in each case (Figure 4.8).

In scenario 1.1, for the case of a horizontal pressure gradient, the fluid flow simulation showed that fluid flow occurs in a more horizontal or oblique direction, with a tendency to follow path parallel to the deformation bands (Figure 4.9). However, the deformation bands at a high angle to the horizontal fluid flow (> 60°) (e.g., deformation bands 5 to 15 in Figure 4.7B) act as orthogonal; these bands are mainly responsible for the equivalent permeability value lower than the rock permeability, effectively imposing a partial barrier condition to fluid flow. The fluid flow is also influenced by the arrangement of the deformation bands, which promotes more effective sealing behavior in some regions. However, the pressure field increases over time until the fluid crosses the partial barrier and drops as the flow reaches other areas of the medium, with flow then occurring until a steady state is reached.

Scenario 2.1 shows an analysis of a pressure gradient inducing a vertical direction flow (Figure 4.10). In general, this case shows that a steady state is obtained more quickly than in scenario 1.1. This behavior is largely due to the vertical to sub-vertical dip of the deformation bands (e.g., deformation bands 5 to 15 in Figure 4.7B) being parallel to the flow direction, thus, offering less resistance to fluid displacement.

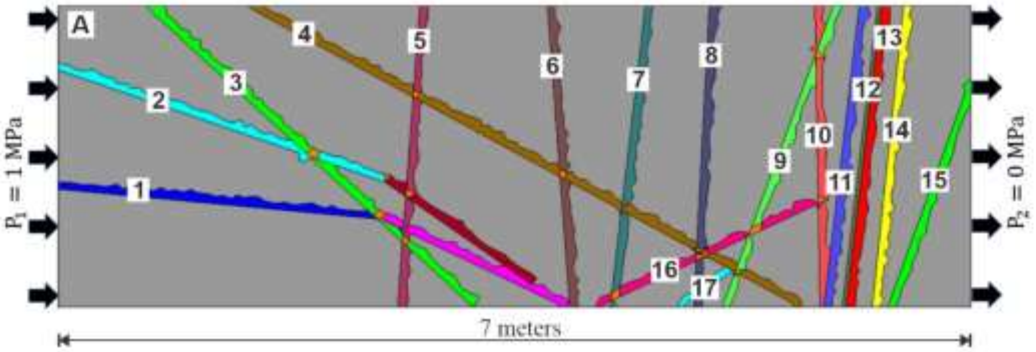

Scenario 1.1: Horizontal flow with measured host rock permeability

Scenario 1.2: Horizontal flow with exaggerated host rock permeability

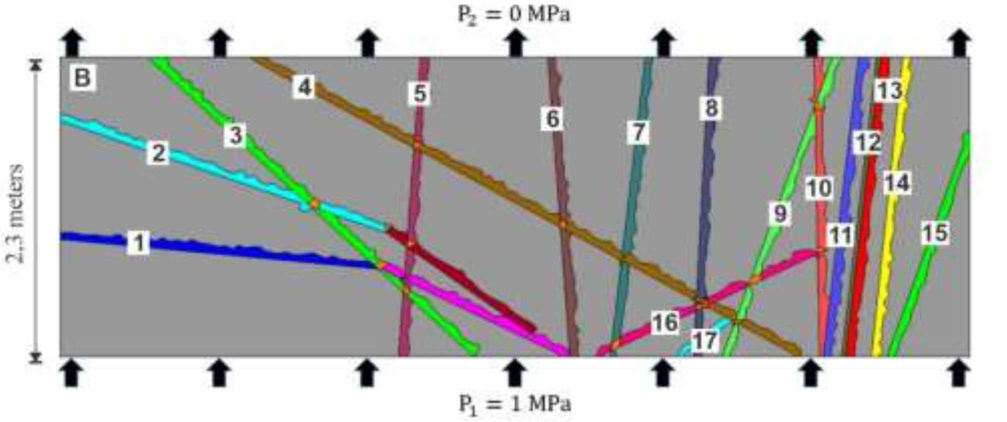

Scenario 2.1: Vertical flow with measured host rock permeability

Scenario 2.2: Vertical flow with exaggerated host rock permeability

Figure 4.8. Boundary conditions used in each simulated scenario: (A) horizontal (scenarios 1.1 and 1.2) and (B) vertical (scenarios 2.1 and 2.2) fluid flow. Note that the deformation bands are not shown at true thickness scale for a better visual representation.

Considering both cases, we reported in scenario 1.1 that the pressure levels are more distributed due to the greater extent of the flow, which takes longer to reach a steady state (step 200) than scenario 2.1, where a steady state is reached by step 50. In scenario 1.1, we observed six pressure levels (I to VI in Figure 4.9), with a slight contrast between them in contrast to scenario 2.1, where we recorded three levels of pressure (I to III in Figure 4.10) with sharper pressure contrasts. This probably occurs due to the flow-perpendicular deformation bands close to the injection boundary, which generate pressure accumulation zones. These dissipate energy more quickly inside the reservoir after fluid breakthrough, as observed in scenario 2.1.

In this study, we used the same host rock permeability to calculate the equivalent permeability of both components (vertical and horizontal). However, limitations in the petrophysical analysis of the plugs did not allow us to measure the directional permeability. The calculated equivalent permeability values (Table 3are 30.88 mD for scenario 1.1 for the horizontal fluid flow (kx) and 29.87 mD for scenario 2.1 for the vertical fluid flow (ky).

Permeability component	Permeability of the host rock (mD)	Equivalent permeability (mD)
Kx (mD) – Horizontal	34.729	30.88
Ky (mD) – Vertical		29.87

Table 3. Indication of the value of equivalent permeabilities of the host rock according to the permeability component.

Furthermore, we constructed sections parallel to the flow gradient to show how the deformation bands directly influence fluid flow in the rock and observe the pressure field measurements when crossing these structures (Figures 4.11 and 4.12). However, we observed that the drop in pore pressure is insufficiently expressive due to the relatively low contrast between the average permeability values (Figure 4.5) of the deformation bands and the host rock, which was two orders of magnitude or less. For this reason, we considered scenarios 1.2 and 2.2, which use the same configuration as scenarios 1.1 and 2.1 (i.e., domain, structures, mesh, boundary condition, and deformation bands permeability), however, the host rock permeability was increased by one order of magnitude. We analyzed the horizontal flow (Figure 4.11, scenarios 1.1 and 1.2) and vertical flow (Figure 4.12, scenarios 2.1 and 2.2), from which sections A and B, respectively, were drawn. In section A (Figure 4.11), we observed minor pore pressure drops (on the order of 0.02 MPa) when crossing each deformation band, evidencing the influence of the deformation bands, for the case of an imposed horizontal pressure gradient. In section B (Figure 4.12), the observed pore pressure drops when crossing each deformation band are greater in the vertical pressure gradient scenario. However, for both cases (Figures 4.11 and 4.12), the pore pressure drop is more pronounced and clearer in the simulated cases where the host rock's k value was increased by one order of magnitude (i.e., from 34.729 to 347.290 mD).

We also calculated the equivalent permeability for both the horizontal and vertical flow directions (respectively kx and ky in Table 4), considering the one order of magnitude increase in host rock permeability (scenarios 1.2 and 2.2). From this, the calculated equivalent permeability values (Table 4) for both scenarios were 134.04 mD for the horizontal fluid flow (kx) and 163.59 mD for the vertical fluid flow (ky).

Increased permeability component	Permeability of the host rock (mD)	Equivalent permeability (mD)
Kx (mD) – Horizontal	347.290	134.04
Ky (mD) – Vertical		163.59

Table 4. Indication of the value of equivalent permeabilities of the host rock according to the permeability component considering the increase of one order of magnitude of the host rock permeability.

4.5. Discussion

4.5.1. Deformation bands structural analysis and their role in fluid flow

In siliciclastic reservoirs, several structural aspects are considered for assessing the impact of the deformation bands on fluid flow, such as their thickness, spatial distribution, 3D connectivity, orientation, and intensity of deformation (Fossen & Bale, 2007; Fossen et al., 2007; Rotevatn et al., 2007; Torabi & Fossen, 2009; Faulkner et al., 2010; Wilkins et al., 2019; Awdal et al., 2020). Our structural results have enabled us to constrain the following aspects: (1) the complex geometry and anastomosing behavior of deformation bands high variability in the strike/dip; (2) the spatial distribution and intensity of the deformation bands; and (3) the deformation bands' thickness.

Various studies have reported that the interactions between deformation bands with different orientations, complex geometry, and anastomosing behavior influence fluid flow in siliciclastic reservoirs (e.g., Fossen & Bale, 2007; Fossen et al., 2007; Zuluaga et al., 2016; Fossen et al., 2017; Romano et al., 2020). The intersection between deformation bands of different orientations may impose compartmentalization, thus acting as a major hindrance for fluid flow (Fossen & Bale, 2007; Fossen et al., 2007; Rotevatn et al., 2007; Zuluaga et al., 2016). In this context, we observed that the deformation bands in the Melancias outcrop exhibit anastomosing behavior (Figures 4.3 and 4.4) with high variability in their orientation and dip (stereonet in Figure 4B). Accordingly, we classified our deformation bands into three populations according to their orientations: (1) NE–SW; (2) E–W; and (3) N–S (Figures 4.7A and 4.7B). Our characterization of the anastomosed arrangement of the deformation bands in the outcrop studied agrees well with previous studies carried out in the RPB (e.g., Françolin et al., 1994; Nogueira et al., 2015; Araujo et al., 2018; Maciel et al., 2018; Nicchio et al., 2018; Pontes et al., 2019; Nogueira et al., 2021; Torabi et al., 2021; Oliveira et al., 2022; Ramos et al., 2022; Silva et al., 2022). For the same outcrop, Nogueira et al. (2015) characterized an arrangement similar to a negative flower structure. The anastomosed arrangement, the large variation in the orientations, and dips variability (ranging from 34° to sub-vertical) of the deformation bands in the Melancias outcrop are important aspects controlling the bands' behavior as partial barriers or conduits for fluid flow. However, diverse aspects, including the fluid flow parameters (e.g., petrophysical properties and flow direction), must also be addressed before evaluating these points in isolation (see section 5.3).

Another issue that impacts fluid flow in siliciclastic reservoirs affected by deformation bands is the intensity of deformation, interpreted as the frequency of the deformation bands per length unit (Gibson, 1998; Sigda et al., 1999; Fossen & Bale, 2007; Fossen et al., 2007; Fachri et al., 2013; Fossen et al., 2017; Romano et al., 2020) as well as the intensity of the deformational mechanism, such as the degree of cataclasis (Ballas et al., 2012; Saillet & Wibberley, 2013; Nogueira et al., 2021). In our study, the spatial distribution of the deformation band exhibits an average frequency of 11 bands/m; however, we also identified a high-density cluster zone containing 27 deformation bands/m (Figure 4.4C). Araujo et al. (2018) analyzed three other fault zones in the RPB and reported values of 17 to 48 deformation bands per meter close to the fault cores. Furthermore, Pontes et al. (2019) and Nogueira et al. (2021) suggest that the Melancias outcrop consists of a complex fault zone where multiple well-developed cluster zones occur, promoting the ultracataclastic deformation intensity developed in these fault cores.

In our case, we interpret that the peak density of 27 deformation bands/m in a cluster zone comprises a probable fault core. Therefore, our geological model for the numerical simulation represents two distinct architectural elements of a fault zone. The first consists of the fault damage zone (deformation bands 1 to 9 in Figure 4.7), and the second, specifically the area between 0.5 and 1.5 m (deformation bands 10 to 15 in Figure 4.7), comprises a cluster zone with an intensity of deformation bands (Araujo et al., 2018; Pontes et al., 2019) and deformation (Pontes et al., 2019; Nogueira et al., 2021) consistent with those of previously described fault cores in the RPB. We observe that deformation band clustering zones (or deformation band fault zone cores) tend to organize the deformation bands (in terms of orientation), decreasing the intersection between deformation bands with different dips (Figure 4.8). This behavior has implications for the construction of geological models because the high structural complexity of a cluster zone (or fault core) can be represented through a group of deformation bands with similar dips (Figure 4.8).

Finally, several studies have reported that deformation bands thickness is one of the main issues to be considered when assessing the impact of the bands on the fluid flow (e.g., Fossen & Bale, 2007; Fossen et al., 2007; Torabi & Fossen, 2009; Saillet & Wibberley, 2013; Fossen et al., 2017). We note that the average thickness of individual deformation bands in the Melancias outcrop is 11.59 mm and follows a power-law distribution for the cumulative frequency of deformation bands versus deformation bands thickness (Figure 4.4D). Pontes et al. (2019) observed a similar power law in two fault zones of the RPB, including the same outcrop studied in this work. Accordingly, this finding has implications for the distribution of deformation band thickness in DFN models. However, we also note that the thickness of deformation bands varies according to their orientation. For example, the NE–SW-striking and E–W-striking deformation bands exhibit average thicknesses of 10.6 and 11.3 mm, respectively, whereas the N–S-striking deformation bands show an average thickness of 5.0 mm (Table 2). Notably, the individual deformation bands in the studied outcrop exhibit average thickness higher than those reported in previous studies in other locations, which suggest that the single deformation bands normally exhibit thicknesses of 1 to 2 mm, occasionally reaching values of up to 10 mm (Fossen et al., 2007; Fossen & Bale, 2007). There are two probable reasons for this difference. The first consists of the host rock properties, including grain size, grain sorting, cementation, and mineralogy, among others, where the deformation bands tend to be in coarse-grained host rock (Fossen et al., 2007). The Melancias outcrop is composed mainly of poorly sorted coarse sandstones and conglomerates (Nogueira et al., 2021), likely explaining the greater thickness of the deformation bands observed in this study.

The second probable reason for this difference is related to the deformation bands of the Melancias outcrop comprising a cluster zone with a deformation intensity similar to that of a fault core. Fossen & Bale (2007) indicate that the deformation band clusters are wider, usually on the order of centimeters or decimeters. In addition, other studies in the RPB suggest that the deformation bands' thickness ranges from 1 mm (single deformation bands) to 175 mm (cluster of deformation bands) (Araujo et al., 2018; Nicchio et al., 2018; Pontes et al., 2019). Thus, the average thickness (11.59 mm) and the average thickness values by the orientation of the deformation bands (NE–SW-striking: 10.6 mm; E–W- striking: 11.3 mm; N–S-striking: 5.0 mm) reported in our study are consistent with those of both single and cluster deformation bands in the previous studies described above, mainly those developed in the RPB.

Furthermore, some studies (Fossen & Bale, 2007; Saillet & Wibberley, 2013; Fossen et al., 2017) have suggested that the optimal way to analyze the deformation bands' thickness is by considering the cumulative thickness (i.e., the sum of the thickness of deformation bands along the scanline). In this context, Fossen & Bale (2007) reported that the cumulative thickness of deformation bands can reach some decimeters. We also analyzed the cumulative thickness of the deformation bands in the Melancias outcrop, which has a value of 1,019.92 mm along the 8 meters of the scanline (Figure 4.4). Thus, the cumulative thickness of the deformation bands in the cluster zones/fault core reported in our study is consistent with the observations of Fossen & Bale (2007). Another alternative for analysis of the deformation bands' thickness is to use the average thickness by to the orientation of the bands. In cases where the deformation bands thickness needs to be explicitly added for discrete elements, this option may be more appropriate.

4.5.2. Petrophysical of the deformation bands and their role for the fluid flow

The presence of deformation bands in granular rocks is responsible for reducing the porosity and permeability of host rocks, with consequent impacts on fluid flow in carbonate and siliciclastic reservoirs (Antonellini & Aydin, 1994; Aydin et al., 2006; Fossen & Bale, 2007; Ballas et al., 2015). These reductions are generally directly dependent and may reach two to three orders of magnitude in permeability (Torabi & Fossen, 2009; Ballas et al., 2012; Wilkins et al., 2019; Awdal et al., 2020) and one order of magnitude in porosity (Antonellini & Aydin, 1994; Torabi & Fossen, 2009;

Ballas et al., 2012; Del Sole et al., 2020). However, in some cases, these reductions may reach four to six orders of magnitude in permeability (Fossen & Bale, 2007; Rotevatn et al., 2007; Torabi & Fossen, 2009; Ballas et al., 2012; Saillet & Wibberley, 2013) and up to two orders of magnitude in porosity (Antonellini et al., 1994; Peralta Gomes et al., 2018; Gambino et al., 2019; Pontes et al., 2019; Pizzati et al., 2020; Nogueira et al., 2021).

The petrophysical values of the deformation bands and host rocks found in the present study are directly dependent and exhibit reductions similar to those reported in previous studies. For instance, the deformation bands average porosity in our study (NE–SW-striking deformation bands: 10.220%; E–W-striking deformation bands: 13.523% mD; N–S-striking deformation bands: 3.151% mD) is up to one order of magnitude lower than the average porosity of the host rock (23.438%) (Figure 4.5A). However, we report individual porosity reductions reaching up to two orders of magnitude in relation to the host rock porosity (ranging from 24.979 to 0.158%; Figure 4.5A and Table 1). Zhou et al. (2012) and Kashif et al. (2019) reported that the porosity influences fluid flow due to sandstone permeability being strongly affected by the pore throat connectivity. Usually, the reduction in porosity in deformation bands occurs due to comminution of the internal grains (Torabi et al., 2013; Gambino et al., 2019; Nogueira et al., 2021). We recorded this type of porosity reduction in the tomography images performed in our study (Figure 4.6).

Likewise, the deformation bands average permeability recorded in our study (NE–SW-striking deformation bands: 0.524 mD; E–W-striking deformation bands: 1.037 mD; N–S-striking deformation bands: 0.608 mD) is approximately two to three orders of magnitude lowest lower than the average permeability of the host rock (34.729 mD) (Figure 4.5B). However, we report individual permeability reduction values reaching up to four orders of magnitude relative to the host rock permeability (ranging from 60.40 to 0.0040 mD – Figure 4.5B and Table 1). Therefore, the porosity and permeability values in the Melancias outcrop are in agreement with those reported in most previous studies. These studies suggest that porosity and permeability reductions across deformation bands are commonly one and two to three orders of magnitude, respectively, but can reach up to two and six orders of magnitude, respectively (e.g., Fossen & Bale, 2007; Torabi & Fossen, 2009; Ballas et al., 2012; Antonellini et al., 2014; Nogueira et al., 2021).

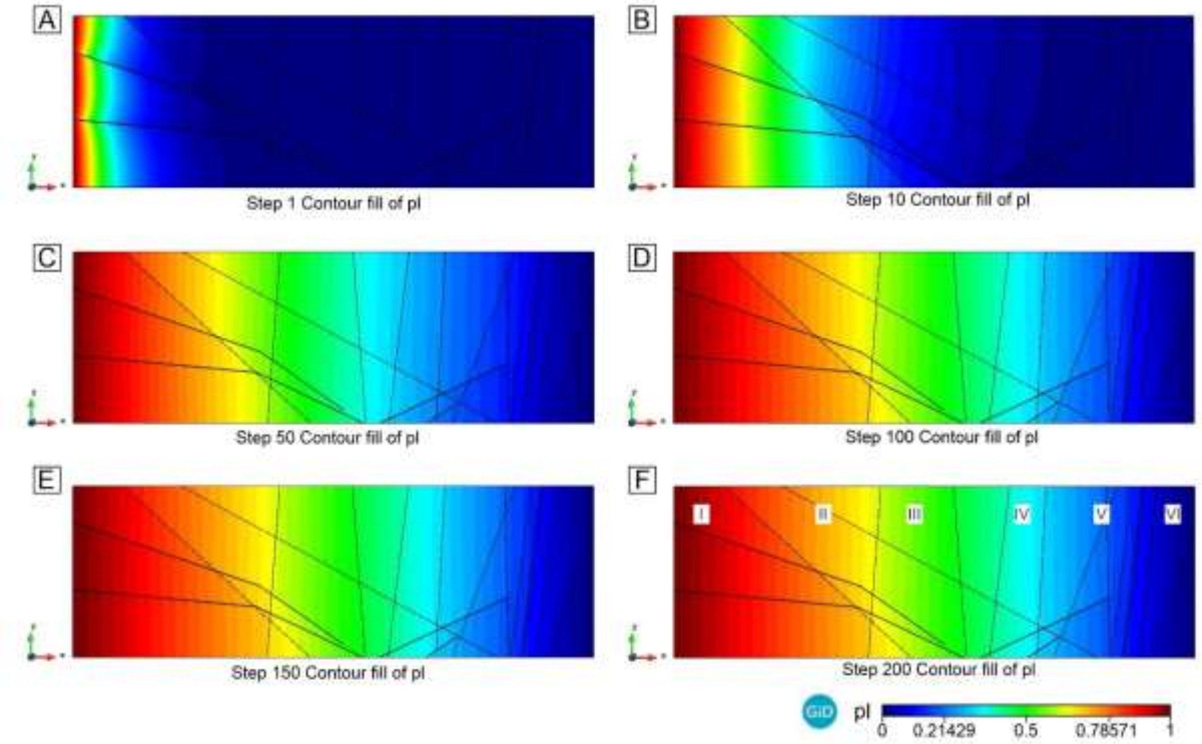

Figure 4.9. Pressure field for horizontal fluid flow (scenario 1.1) at six different times. Pressure (MPa) show at step (A) 1, (B) 10, (C) 50, (D) 100, (E) 150, and (F) 200. Each step represents the simulation time, where 1 step is equal to 1 second. The black lines show the deformation bands. For more details about the deformation bands, see Figure 4.7. For the boundary conditions used in this simulation, see Figure 4.8A.

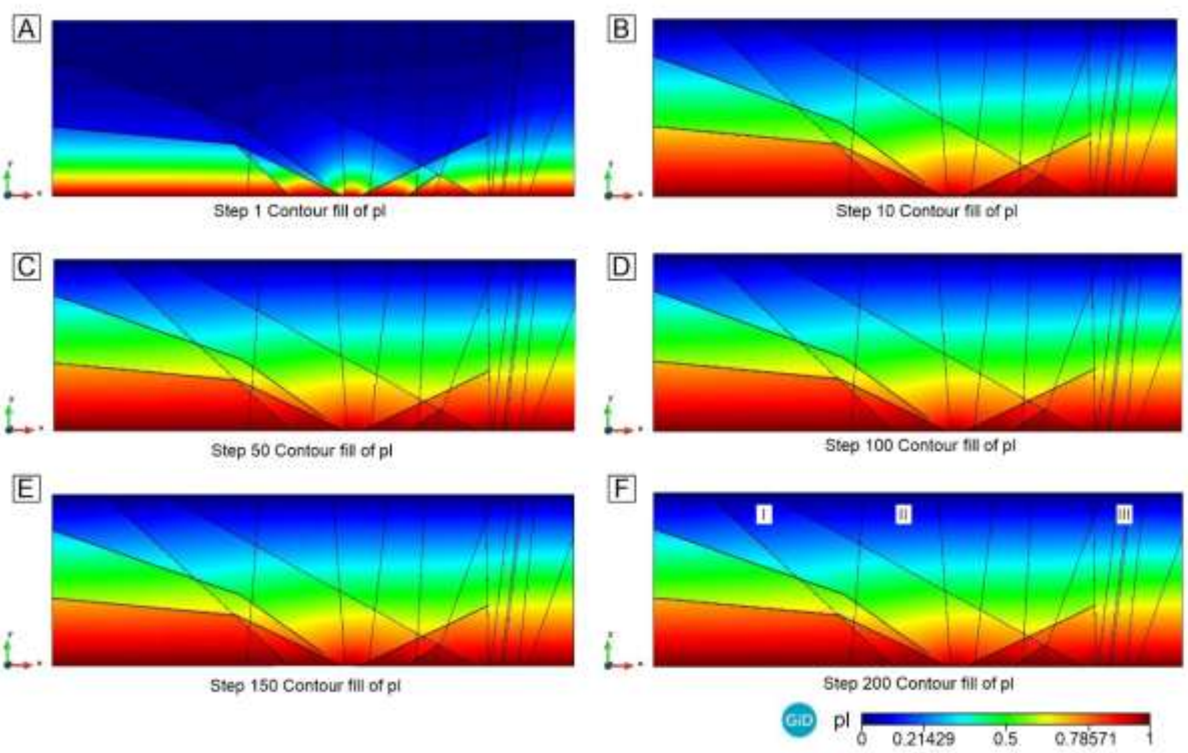

Figure 4.10. Flow simulation in the vertical direction along six different times (Scenario 2.1). Fluid flow simulation in the (A) Step 1, (B) Step 10, (C) Step 50, (D) Step 100, (E) Step 150, and (F) Step 200. Fluid pressure values are in MPa. The black lines comprise the deformation bands. For more details about the deformation bands, see Figure 4.7. For the boundary conditions used in this simulation, see Figure 4.8B.

Although our results about the petrophysical properties reduction are in accordance with most previous studies, we question whether our measures may represent an underestimate. For instance, the diameter of the plug samples is 3.54 cm, while the average deformation band thickness is 11.59 mm. Therefore, the measurements of our samples represent an average of both host rock and deformation band properties. Some studies have discussed this issue (e.g., Antonellini & Aydin, 1994; Gibson, 1998) and suggested this problem could be mitigated through the use of digital petrophysics by analysis of thin section images. For this reason, we compared our petrophysical properties obtained from plug cores to the petrophysical properties of Nogueira et al. (2021), who utilized digital petrophysics through image analysis of thin sections from the same outcrop (Figure 4.5D). Nogueira et al. (2021) reported porosity and permeability reductions in the deformation bands relative to the host rock of up to one order of magnitude and up to six orders of magnitude, respectively. Our plug-based petrophysical analysis shows a reduction of up two orders of magnitude in the porosity and up to four orders of magnitude in the permeability values. Pontes et al. (2019) also reported a reduction of up to two orders of magnitude in porosity values from the same outcrop investigated in our study. In terms of permeability, Nogueira et al. (2021) compared the permeability reduction of the deformation bands relative to pristine sandstones. When the permeability of the deformation bands from our study are compared with the permeability of the pristine sandstones analyzed by Nogueira et al. (2021) (Figure 4.5C), we also observe the same six orders of magnitude reduction. Therefore, despite the differences presented above, when comparing the petrophysical properties of the deformation bands with those of pristine host rocks, the variations found in our study utilizing plugs samples are similar to the results reported by Nogueira et al. (2021) using digital petrophysics thin section image analysis.

On this basis, from the porosity and permeability reductions relative to the host rock in our study, we suggest that the deformation bands of the Melancias outcrop could partially compartmentalize the reservoir during the fluid flow simulation presented in this study.

4.5.3. Implications of the deformation bands on the fluid flow in sandstone

In the last two sections, we discussed several structural and petrophysical properties that indicated that the deformation bands of the Melancias outcrop are likely candidate partial barriers to fluid flow. In this context, we would like to highlight two major points: (1) the anastomosing behavior and intersections between deformation bands of different orientations are described as a major hindrance to fluid flow, which may impose reservoir compartmentalization (Fossen & Bale, 2007; Fossen et al., 2007; Rotevatn et al., 2007; Zuluaga et al., 2016); and (2) the magnitude of the permeability contrast between the deformation bands and the host rock (Fossen & Bale, 2007; Rotevatn et al., 2007; Zuluaga et al., 2016; Qu & Tveranger, 2016).

We report that the anastomosed arrangement and intersection between deformation bands with differing orientations may impose reservoir compartmentalization (I to VI in Figure 4.9 and I to III in Figure 4.10). This compartmenting effect can be observed through the pore pressure profile (Figures 4.11 and 4.12). The clearest barrier effect of bands 1 to 4 is recorded for vertical fluid flow – the fluid pressure profile jump is more significant for vertical flow (Scenario 1.1 –

Figure 4.12) than for horizontal flow (Scenario 2.1 – Figure 4.11), indicating the more effective vertical resistance of these bands against fluid flow. The bands demonstrate pressure differences in the interband rock, indicating compartmentalization of different regions of the fault zone.

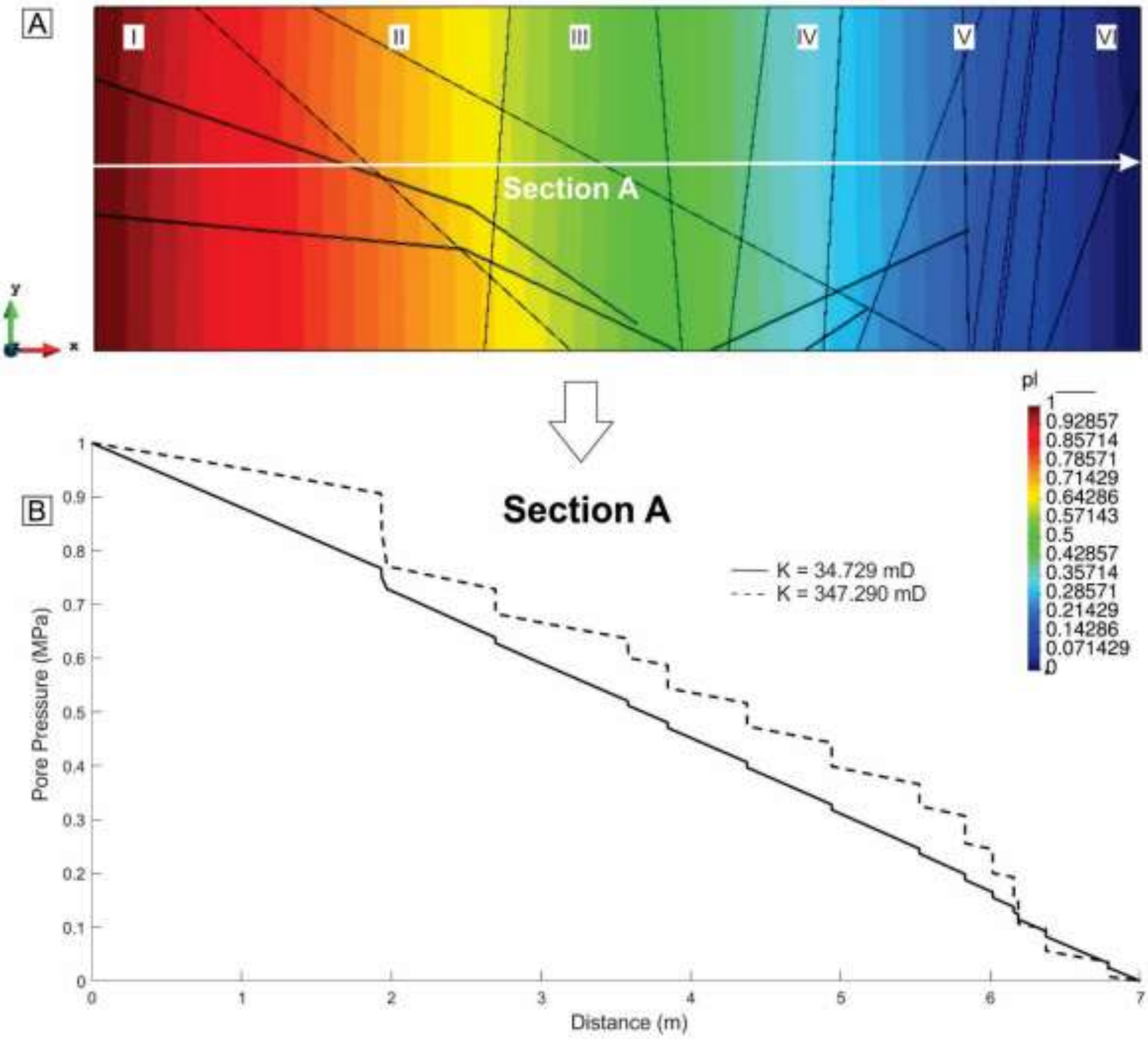

Figure 4.11. (A) Step 150 of case 1 along section A used to construct the (B) performance graph showing the horizontal case (continuous line) and the case with increased permeability (dashed line). The K relates to samples collected without deformation bands (host rock). Fluid pressure values are in MPa.

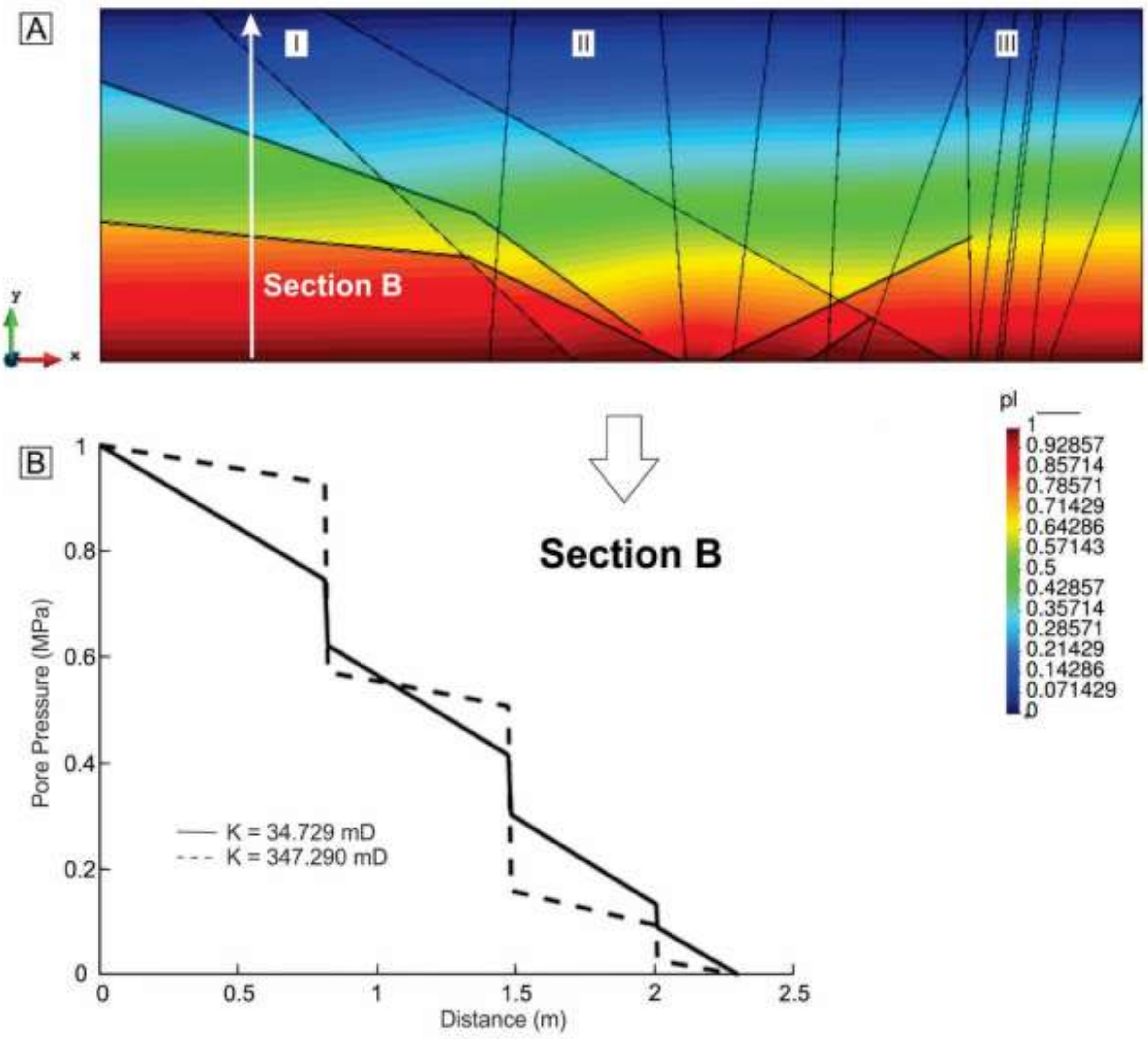

Figure 4.12. (A) Step 150 of case 2 along section B used to construct the (B) performance graph showing the vertical case (continuous line) and the case with increased permeability (dashed line). The K relates to samples collected without deformation bands (host rock). Fluid pressure values are in MPa.

The equivalent permeability tensor components, kx and ky, showed similar values (Table 3), however, the vertical component has a lower value than the horizontal one. We suggest that this relates to the influence of bands 1 to 5 in both fluid flow directions and the difference in dimensions of the section in the horizontal and vertical directions. Thus, for this outcrop, the band patterns resist fluid displacement for both horizontal and vertical directions. We would expect a considerable difference between the upscaled equivalent permeability components, kx and ky, in the absence of bands 1 to 5. the value of kx tends to be slightly lower (kx=32.49 mD) than ky (ky=31.414 mD) because the vertical bands present direct resistance to fluid flow in the horizontal direction but are parallel to vertical flow. The upscaling process for determining the equivalent permeability tensor allows an adequate and accurate comprehension of this hydraulic response. Another important aspect is that the measured upscaled equivalent permeability was slightly lower than that of the host rock matrix; this is due to the difference between the host rock and deformation band permeability values for this outcrop. In this case, the difference is almost two orders of magnitude (Table 3).

Based on previous studies, the contrast between the permeability of the host rock and deformation bands can be considered a major control on the behavior of deformation bands as sealing structures and their partial barrier effects in fluid flow (Rotevatn & Fossen, 2011; Qu & Tveranger, 2016; Botter et al., 2017). Therefore, we simulated an additional scenario (Figures 4.11 and 4.12) to evaluate the contrast between the permeability of the deformation bands and the host rock. As described above, we increased the average permeability of the host rock by one order of magnitude (from 34.729 to 347.290 mD) and performed two new numerical simulations with the same conditions as the previous models (Figures 4.9 and 4.10). We observed that independent of the flow direction (horizontal or vertical), the deformation bands impose a partial barrier to water flow. For instance, the pore pressure drops mark the effect of the deformation bands during the numerical simulation of the fluid flow due to the contrast of up to two orders of magnitude between the average permeability of the deformation bands and host rock (continuous black line in Figures 4.11B and 4.12B). However, these drops in the pore pressure are more evident when an additional order of magnitude contrast was added between the average permeability of the deformation bands and the host rock (dashed black line in Figures 4.11B and 4.12B). Therefore, the contrast of three orders of magnitude enhances the partial barrier effects of the deformation bands on the fluid flow irrespective of whether the pressure gradient is horizontal or vertical.

Furthermore, we report that in the case of imposing a pressure gradient in the vertical direction, the pore pressure drops (dashed black line in Figure 4.12B) are more evident. We interpret that this is likely related to the higher equivalent permeability value in the ky direction than the kx direction (Table 4). For this reason, we suggest that determining an equivalent property is an adequate strategy to translate this effect into a reservoir model.

Additionally, we observe that an aspect rarely addressed in previous studies is a detailed analysis of the strike and the dip of the deformation bands with respect to the fluid flow direction (e.g., Balsamo et al., 2012; Bense et al., 2013; Qu et al., 2017; Awdal et al., 2020; Del Sole et al., 2020; Romano et al., 2020). In the fluid flow simulation of the Melancias outcrop, we note that the horizontal case presents greater compartmentalization throughout the model, occurring in six pressure levels due to the numerous deformation bands oriented obliquely or perpendicular to the flow direction. In contrast, the vertical case presents only three pressure levels. In this instance, most of the deformation bands are parallel to the flow direction, causing compartmentalization only in areas where the deformation bands are oblique to the flow. Likewise, Awdal et al. (2020) and Del Sole et al. (2020) suggest that the distribution of the deformation bands vertically and laterally exerts an important control on fluid flow, such as a slowdown effect, primarily occurring when the flow direction is oblique to the deformation bands. In contrast, the deformation bands can act as frontiers for a preferential flow pathway through compartmented rock zones (i.e., inter-band zones) when the fluid flow is parallel to these structures. The same fluid flow pattern is reported at microscale in grainstones, where deformation bands can generate connected channels contributing to permeability only parallel to the bands (Antonellini & Aydin, 1994; Antonellini et al., 2014; Zambrano et al., 2018). Likewise, some studies have indicated that fault damage zones usually act as complex conduit–barrier systems for flow along and across the fault, respectively (e.g., Jourde et al., 2002; Balsamo et al., 2012; Bense et al., 2013), whit flow mainly occurring along the fault. This behavior may have fundamental implications for aquifer management in semiarid climate regions (e.g., Sigda et al., 1999; Sigda & Wilson, 2003; Medeiros et al., 2010; Hadley et al., 2020), such as the northeast of Brazil.

Finally, although our results show the partial barrier effect caused by the deformation bands influenced the fluid flow, we report that the bands do not fully compartmentalize the reservoir in the analyzed scenarios. Similar results have also been reported in previous studies where the structural arrangement of the deformation bands and the contrast between the average permeability of the deformation bands and the host rock are equivalent to those observed in the Melancias outcrop (e.g., Antonellini & Aydin, 1994; Fossen & Bale, 2007; Fossen et al., 2007; Medeiros et al., 2010; Ballas et al., 2012; Zuluaga et al., 2016; Awdal et al., 2020; Nogueira et al., 2021). Based on the findings of this study from the RPB, deformation bands clearly impose several effects on fluid flow, mainly when there are numerous intersections between bands with varying dips and when the permeability contrast of the bands relative to the host rock is largest. Additionally, we have highlighted the importance of evaluating the interaction between the orientation and the dip of the deformation bands relative to the fluid orientation during flow.

4.6. Conclusions

The present study performed structural and petrophysical analyses to support our 2D modeling and numerical simulation to evaluate the influence of deformation bands during water flow in sandstone. Our data are consistent with several previous studies, which suggested that fluid flow in siliciclastic reservoirs is strongly affected by the presence of deformation bands. Therefore, we propose the following conclusions from this present study:

1 – The variable orientation of deformation bands (anastomosed arrangement) and the degree of connectivity are the main aspects that determine the bands' behavior during water flow.

2 – The petrophysical analysis showed that a reduction in porosity of up to two orders of magnitude and permeability of up to four orders of magnitude imposed by the deformation bands relative to the host rock controls the influence of the bands during water flow.

3 – The jump in fluid pressure profiles caused by the deformation bands due to discontinues in the permeability field highlights the partial barrier effect caused by the bands, indicating their influence during water flow but demonstrating that the bands also do not fully compartmentalize the reservoir.

4 – The upscaled equivalent permeability tensor presents components subtly lower than the host rock values. However, these upscaled properties showed a considerable reduction in the cases where the permeability difference was three orders of magnitude, thereby enhancing the influence of the bands during water flow. Despite this, the bands also do not fully compartmentalize the reservoir in these scenarios. The control exerted by the permeability contrast between the host rock and deformation bands is an essential aspect to consider when integrating geological characterization and numerical model.

5 – The orientation of the deformation bands relative to the orientation of fluid flow can determine whether the bands will act as partial or total barriers. When the fluid flow is parallel to the deformation bands, the bands will tend to act as frontiers and promote a fluid flow corridor along the deformation bands' length. In contrast, if the fluid flow is oblique to the deformation bands, the bands tend to act as partial barriers.

6 -. The equivalent permeability tensor from a flow-based upscaling process in a high fidelity model can be used as a benchmark for comparison with different upscaled permeability calculation methods for damage zones with deformation bands.

11 - We propose that the equivalent permeability calculation can be used when considering deformation structures crossing the entire cell where a good part of a reservoir cell can present a discontinuity of these structures along the fault zone trace.

References

Alvarez, L.L., Guimarães, L.J.N., Gomes, I.F., Beserra, L., Pereira, L.C., Miranda, T.S., Maciel, B., Barbosa, J. A., 2021. Impact of Fracture Topology on the Fluid Flow Behavior of Naturally Fractured Reservoirs. Energies 14, 5488. https://doi.org/10.3390/en14175488

Antonellini, M., Aydin, A., 1994. Effect of Faulting on Fluid Flow in Porous Sandstones: Petrophysical Properties. AAPG Bulletin 78, 355–377. https://doi.org/10.1306/BDFF90AA-1718-11D7-8645000102C1865D

Antonellini, M., Aydin, A., Pollard, D.D., 1994. Microstructure of deformation bands in porous sandstones at Arches National Park, Utah. Journal of Structural Geology 16, 941-959. https://doi.org/10.1016/0191-8141(94)90077-9

Antonellini, M., Cilona, A., Tondi, E., Zambrano, M., Agosta, F., 2014. Fluid flow numerical experiments of faulted porous carbonates, Northwest Sicily (Italy). Marine and Petroleum Geology 55, 186-201. https://doi.org/10.1016/j.marpetgeo.2013.12.003

Awdal, A., Suramairy, R., Singh, K., Fabre, G., Alsop, G. I., 2020. Deformation bands and their impact on fluid flow: Insights from geometrical modelling and multi-scale flow simulations in sandstones. Journal of Structural Geology 141, 104215. https://doi.org/10.1016/j.jsg.2020.104215

Aydin, A., 1978. Small faults formed as deformation bands in sandstone. Pure and Applied Geophysics 116, 913-930. https://doi.org/10.1007/978-3-0348-7182-2_22

Aydin, A., Borja, R.I., Eichhubl, P., 2006. Geological and mathematical framework for failure modes in granular rock. Journal of Structural Geology 28, 83–98. https://doi.org/10.1016/j.jsg.2005.07.008

Araujo, R.E.B., Bezerra, F.H.R., Nogueira, F.C.C., Balsamo, F., Carvalho, B.R.B.M., Souza, J.A.B., Melo, A.C.C., 2018. Basement control on fault formation and deformation band damage zone evolution in the Rio do Peixe Basin, Brazil. Tectonophysics 745, 117-131. https://doi. org/10.1016/j.tecto.2018.08.011

Ballas, G., Soliva, R., Sizun, J.-P., Benedicto, A., Cavailhes, T., Raynard, S., 2012. The importance of the degree of cataclasis in shear bands for fluid flow in porous sandstone, Provence, France. AAPG Bulletin 96, 2167-2186. https://doi.org/10.1306/04051211097

Ballas, G., Fossen, H., Soliva, R., 2015. Factors controlling permeability of cataclastic deformation bands and faults in porous sandstone reservoirs. Journal of Structural Geology 76, 1-21. 76. https://doi.org/10.1016/j.jsg.2015.03.013

Balsamo, F., Storti, F., Grocke, D., 2012. Fault-related fluid flow history in shallow marine sediments from carbonate concretions, Crotone Basin, south Italy. Journal of the Geological Society 169, 613-626. https://doi.org/10.1144/0016-76492011-109

Braathen, A., Tveranger, J., Fossen, H., Skae, T., Cardozo, N., Semshaug, S., Bastesen, E. Sverdrup, E., 2009. Fault facies and its application to sandstone reservoir. AAPG Bulletin 93, 891-917. https://doi.org/10.1306/03230908116

Belayneh, M., Geiger, S., Matthai, S. K., 2006. Numerical simulation of water injection into layered fractured carbonate reservoir analogs. AAPG Bulletin 90, 1473-1493. https://doi.org/10.1306/05090605153

Bense, V.F., Gleeson, T., Loveless, S.E., Bour, O., Scibek, J., 2013. Fault zone hydrogeology. Earth-Science Reviews 127, 171-192. http://dx.doi.org/10.1016/j.earscirev.2013.09.008

Bourbiaux, B., 2010. Fractured Reservoir Simulation: a Challenging and Rewarding Issue. Oil & Gas Science and Technology – Rev. IFP 65, 227-238. https://doi.org/10.2516/ogst/2009063

Botter, C., Cardozo, N., Qu, D., Tveranger, J., Kolyukhin, D., 2017. Seismic characterization of fault facies models. Interpretation 5, SP9-SP26. https://doi.org/10.1190/INT-2016-0226.1

Childs, C., Manzocchi, T., Walsh, J.J., Bonson, C.G., Nicol, A., Schopfer, M.P.J., 2009. A geometric model of fault zone and fault rock thickness variations. Journal of Structural Geology 31, 117–127. https://doi.org/10.1016/j.jsg.2008.08.009

Choanji, T., Rita, N., Yuskar, Y., Pradana, A., 2018. Connectivity relationship of fluid flow on deformation band analog study at Petani Formation, Riau, Indonesia. Bulletin of Scientific Contribution: Geology. 15, 193-198. https://doi.org/10.24198/bsc%20geology.v15i3.15096

Choi, J., Edwards, P., Ko, K., Kim, Y-S., 2016. Definition and classification of fault damage zones: A review and a new methodological approach. Earth-science Reviews 152, 70-87. http://dx.doi.org/10.1016/j.earscirev.2015.11.006

Conceição, J.C.J., Zalán, P.V., Wolff, S., 1988. Mecanismo, Evolução e cronologia do rifte sul-atlântico (Mechanism, evolution and chronology of South Atlantic Rifting). Boletim de Geociências da Petrobras, Rio de Janeiro 2 (2/4), 255-265.

de Castro, D.L., Oliveira, C.D., Gomes Castelo Branco, R.M., 2007. On the tectonics of the Neocomian Rio do Peixe Rift Basin, NE Brazil: lessons from gravity, magnetics, and radiometric data. Journal of South American Earth Sciences 24, 184-202. https://doi.org/10.1016/j.jsames. 2007.04.001

de Souza, D.H.S., Nogueira, F.C.C., Vasconcelos, D.L., Torabi, A., Souza, J.A.B., Nicchio, M.A., Pérez, Y.A.R., Balsamo, F., 2021. Growth of cataclastic bands into a fault zone: A multiscalar process by microcrack coalescence in sandstones of Rio do Peixe Basin, NE Brazil. Journal of Structural Geology 146, 104315. https://doi.org/10.1016/j.jsg.2021.104315

Del Sole, L., Antonellini, M., Calafato, A., 2020. Characterization of sub-seismic resolution structural diagenetic heterogeneities in porous sandstones: Combining ground-penetrating radar profiles with geomechanical and petrophysical in situ measurements (Northern Apennines, Italy). Marine and Petroleum Geology 117, 104-375. https://doi.org/10.1016/j.marpetgeo.2020.104375

Durlofsky, L.J., 2005. Upscaling and Gridding of Fine Scale Geological Models for Flow Simulation. 8th International Forum on Reservoir Simulation Iles Borromees, Stresa, Italy, June 20-24.

Fachri, M., Rotevatn, A., Tveranger, J.,2013. Fluid flow in relay zones revisited: Towards an improved representation of small-scale structural heterogeneities in flow models. Marine and Petroleum Geology 46, 144–164. https://doi.org/10.1016/j.marpetgeo.2013.05.016

Falcão, F., Barroso, J., Murad, J., Pereira, P., Vargas, E., Juvinao, A., Muller, A., Roehl, D., Quevedo, R., Mejia, C., Guimarães, L., Beserra, L., Alvarez, L., Cleto, P., Manzoli, O., 2018. Synthetic Benchmark for the Computation of Equivalent Properties in Coupled Flow and Geomechanics Conditions for a Fractured Carbonate Rock. In ARMA Symposium, DFNE 18-0151_0228_000496.

Faulkner, D.R., Jackson, C.A.L., Lunn, R.J., Schilische, R.W., Shipton, Z.K., Wibberley, C.A.J., Withjack, M.O., 2010. A review of recent developments concerning the structure, mechanics and fluid flow of fault zones. Journal of Structural Geology 32, 1557-1575. https://doi.org/10.1016/j.jsg.2010.06.009

Fisher, Q.J., Knipe, R.J., 2001. The permeability of faults within siliciclastic petroleum reservoirs of the North Sea and Norwegian Continental Shelf. Marine and Petroleum Geology 18, 1063–1081. https://doi.org/10.1016/S0264-8172(01)00042-3

Flemisch, B., Berre, I., Boon, W., Fumagalli, A., Schwenck, N., Scotti, A., Stefansson, I., Tatomir, A., 2018. Benchmarks for single-phase flow in fractured porous media. Advances in Water Resources 111, 239-258. https://doi.org/10.1016/j.advwatres.2017.10.036

Fossen, H., Johansen, T., Hesthammer, J., Rotevatn, A., 2005. Fault interaction in porous sandstone and implications or reservoir management; examples from southern Utah. AAPG Bulletin. 89. 1593-1606. https://doi.org/10.1306/07290505041

Fossen, H., Bale, A., 2007. Deformation bands and their influence on fluid flow. AAPG Bulletin 91, 1685-1700. https://doi.org/10.1306/07300706146

Fossen, H., Schultz, R., Shipton, Z.K., Mair, K., 2007. Deformation bands in a sandstone e a review. Journal of the Geological Society 164, 755-769. https://doi.org/10.1144/0016-76492006-036

Fossen, H., Soliva, R., Ballas, G., Trzaskos, B., Cavalcante, C., Schultz, R.A., 2017. A review of deformation bands in reservoir sandstones: geometries, mechanisms and distribution. In: Badley, A., Dee, S.J., Wennberg, O.P. (Eds.). Subseismic-Scale Reservoir Deformation. Journal of the Geological Society, Special Publications 459, 9–33. https://doi.org/10.1144/SP459.4

Foxford, K.A., Walsh J.J., Watterson, J., Garden, I.R., Gusctt S.C., Burley, S.D., 1998. Structure and content of the Moab Fault Zone, Utah, U.S.A., and its implications for fault seal prediction. In: Jones, G., Fisher, Q., Knipe, R.J. (Eds.). Faulting, Fault Sealing and Fluid Flow in Hydrocarbon Reservoirs. Geological Society, London, Special Publications 147, 87-103. https://doi.org/10.1144/GSL.SP.1998.147.01.06

Françolin, J.B.L., Szatmari, P., 1987. Mecanismo de rifteamento da porção oriental da margem brasileira. Revista Brasileira de Geociências 17, 196-207.

Françolin, J.B.L. Analyse structurale du bassin du Rio do Peixe (Brésil). 1992 - Centre Armoricaine d'Étude Structurale des Socles, Université de Rennes. Tese de Doutorado. 240p.

Françolin, J.B.L., Cobbold, P.R., Szatmari, P., 1994. Faulting in the Early Cretaceous Rio do Peixe (NE Brazil) and its significance for the opening of the Atlantic. Journal of Structural Geology 16, 647-661.

Gambino, S., Fazio, E., Maniscalco, R., Punturo, R., Lanzafame, G., Barreca, G., Butler, R.W.H., 2019. Fold-related deformation bands in a weakly buried sandstone reservoir analogue: A multi-disciplinary case study from the Numidian (Miocene) of Sicily (Italy). Journal of Structural Geology 118, 150-164. https://doi.org/10.1016/j.jsg.2018.10.005

Gibson, R.G., 1998. Physical character and fluid-flow properties of sandstone-derived fault zone. Geological Society, London, Special Publication 127, 83-97. https://doi.org/10.1144/GSL.SP.1998.127.01.07

Guimarães, L. do N., Gens, A., Olivella, S., 2007. Coupled Thermo-Hydro-Mechanical and Chemical Analysis of Expansive Clay Subjected to Heating and Hydration. Transport in Porous Media. https://doi.org/10.1007/s11242-006-0014-z

Hadley, D.R., Abrams, D.B., Roadcap, G.S., 2020. Modeling a large-scale historic aquifer test: insight into the hydrogeology of a regional fault zone. Ground Water 58(3), 453-463. https://doi.org/10.1111/gwat.12922

He, C., Durlofsky, L.J., 2006. Structured flow-based gridding and upscaling for modeling subsurface flow. Advances in Water Resources 29(12),1876-1892. https://doi.org/10.1016/j.advwatres.2005.12.012

Healy, D., Jones, R.R., Holdsworth, R.E., 2006. Polymodal faulting by crack or anticrack interaction. AGU Fall Meeting Abstracts. 1, 449.

Healy, D, Blenkinsop, T.G., Timms, N.E., Meredith, P.G., Mitchell, T.M., Cooke, M.L., 2015. Polymodal faulting: time for a new angle on shear failure. Journal of Structural Geology 80, 57-71. https://doi.org/10.1016/j.jsg.2015.08.013

Jourde, H., Flodin, E.A, Aydin, A., Durlofsky, L.J., Wen, X.H. 2002. Computing permeability of fault zones in eolian sandstone from outcrop measurements. AAPG Bulletin 86(7), 1187-1200. https://doi.org/10.1306/61EEDC4C-173E-11D7-8645000102C1865D

Kashif, M., Cao, Y., Yuan, G., Asif, M., Saved, K., Mendez, J.N., Khan, D., Miruo, L., 2019. Pore size distribution, their geometry and connectivity in deeply buried Paleogene Es1 sandstone reservoir, Nanpu Sag, East China. Petroleum Science 16, 981-1000. https://doi.org/10.1007/s12182-019-00375-3

Knipe, R.J., 1998. Faulting, fault sealing and fluid flow in hydrocarbon reservoirs: an introduction. Geological Society, London, Special Publication 147, 7-21. https://doi.org/10.1144/GSL.SP.1998.147.01.01

Lehner, F.K., Pilaar, W.F., 1997. The emplacement of clay smears in synsedimentary normal faults: inferences from field observations near Frechen, Germany. In: Moller-Pedersen, P., Koestler, A.G. (Eds.) Hydrocarbon Seals: Importance for Exploration and Production. Norwegian Petroleum Society, Special Publications 7, 39-50. https://doi.org/10.1016/S0928-8937(97)80005-7

Leveille, G.P., Knipe, R.J., More, C., Ellis, D., Dudley, G., Jones, G., Fisher, Q.J, Allinson, G., 1997. Compartmentalization of Rotliegendes gas reservoirs by sealing faults, Jupiter fields area, southern North Sea. In: Ziegler, K., Turner, P., Daines, S.R. (Eds.) Petroleum Geology of the North Sea: Future Potential. Geological Society, London, Special Publications 123, 87-104. https://doi.org/10.1144/GSL.SP.1997.123.01.06

Lima Filho, M.F., 1991. Evolução tectono-sedimentar da Bacia do Rio do Peixe - PB. Dissertação Mestrado – Universidade Federal de Pernambuco. Recife. 99 p.

Lima Filho, M. L., 2001. Mapa faciológico da Bacia do Rio do Peixe, Estado da Paraíba. In: 6º SIMPÓSIO SOBRE O CRETÁCEO DO BRASIL, Rio Claro. Boletim. Rio Claro: UNESP, 103-106.

Maciel, I. B., Dettori, A., Balsamo, F., Bezerra, F.H.R., Vieira, M.M., Nogueira, F.C.C., Salvioli-Mariani, E., Sousa, J.A.B., 2018. Structural Control on Clay Mineral Authigenesis in Faulted Arkosic Sandstone of the Rio do Peixe Basin, Brazil. Minerals 8, 1-17. https://doi.org/10.3390/min8090408

Matos, R.M.D., 1992. The Northest Brasilian rift system. Tectonics 11, 4, 776-791. https://doi.org/10.1029/91TC03092 Matos, R.M.D., 2000. Tectonic evolution of the Equatorial South Atlantic. In: Mohriak, W., Talwani, M. Atlantic rifts and continental margins. Geophysical Monograph 115, 331-354. https://doi.org/10.1029/GM115p0331

Medeiros V.C., Amaral C.A., Rocha D.E.G.A., Santos R.B., 2005. Mapa geológico dos Estados da Paraíba, Rio Grande do Norte e Ceará, escala 1:250.000. Programa Geologia do Brasil - PGB, CPRM.

Medeiros, W.E., do Nascimento, A.F., Alves da Silva, F.C., Destro, N., Demétrio, J.G.A., 2010. Evidence of hydraulic connectivity across deformation bands from field pumping tests: two examples from Tucano Basin, NE Brazil. Journal of Structural Geology 32, 1783-1791. https://doi.org/10.1016/j.jsg.2009.08.019

Mendonça Filho, J.G., 2006. Aspectos Geoquímicos do óleo da Bacia de Sousa (Cretáceo Inferior), Nordeste do Brasil: Contexto Geológico. São Paulo, UNESP, Geociências 25, 91-98.

Moinfar, A., Narr, W., Hui, M, Mallison, B., Lee, S.H., 2011. Comparison of Discrete-Fracture and Dual-Permeability Models for Multiphase Flow in Naturally Fractured Reservoirs. SPE Reservoir Simulation Symposium, SPE 142295, The Woodlands, Texas, USA.

Nicchio, M.A., Nogueira, F.C.C., Balsamo, F., Souza, J.A.B., Carvalho, B.R.B.M., Bezerra, F.H.R., 2018. Development of cataclastic foliation in deformation bands in feldspar rich conglomerates of the Rio do Peixe Basin, NE Brazil. Journal of Structural Geology 107, 132-141. https://doi.org/10.1016/J.JSG.2017.12.013

Nogueira, F.C.C., Marques, F.O., Bezerra, F.H.R., de Castro, D.L., Fuck, R.A., 2015. Cretaceous intracontinental rifting and post-rift inversion in NE Brazil: insights from the Rio do Peixe Basin. Tectonophysics 644, 92–107.

Nogueira, F.C.C., Nicchio, M.A., Balsamo, F., Souza, J.A.B., Silva, I.V.L., Bezerra, F.H.R., Vasconcelos, D.L., Carvalho, B.R.B.M., 2021. The influence of the cataclastic matrix on the petrophysical properties of deformation bands in arkosic sandstones. Marine and Petroleum Geology 134, 104825. https://doi.org/10.1016/j.marpetgeo.2020.104825

Oliveira, L.S.B., Nogueira, F.C.C., Vasconcelos, D.L., Balsamo, F., Bezerra, F.H.R., Pérez, Y.A.R., 2022. Mechanical stratigraphy influences deformation band pattern in arkosic sandstones, Rio do Peixe Basin, Brazil. Journal of Structural Geology 155, 104510. https://doi.org/10.1016/j.jsg.2022.104510

Olivella, S. Carrera, G.A., Alonso, E.E., 1996. Numerical formulation for a simulator (CODE_BRIGHT) for the coupled analysis of saline media. Engineering Computations 13, 87-112. https://doi.org/10.1108/02644409610151575

Ortega, O.J., Marrett, R.A., Laubach, S.E., 2006. A scale-independent approach to fracture intensity and average spacing measurement. AAPG Bulletin 90, 193-208. https://doi.org/10.1306/08250505059

Parry, W.T., Chan, M.A., Beitler, B., 2004. Chemical bleaching indicates episodes of fluid flow in deformation bands in sandstone. AAPG Bulletin 88, 175-191. https://doi.org/10.1306/09090303034

Peralta Gomes Jr, C., Fossen, H., Almeida, R.P., Salmoni, B., 2018. Subseismic deformation in the Vaza-Barris Transfer Zone in the Cretaceous Recôncavo-Tucano-Jatobá rift system, NE Brazil. Journal of Structural Geology 117, 81-95. https://doi.org/10.1016/j.jsg.2018.09.007

Pittman, E.D., 1981. Effect of fault-related granulation on porosity and permeability of quartz sandstones, Simpson Group (Ordovician) Oklahoma. AAPG Bulletin 65, 2381-2387. https://doi.org/10.1306/03B5999F-16D1-11D7-8645000102C1865D

Pizzati, M., Balsamo, F., Storti, F., 2020. Displacement-dependent microstructural and petrophysical properties of deformation bands and gouges in poorly lithified sandstone deformed at shallow burial depth (Crotone Basin, Italy). Journal of Structural Geology 137, 104069. https://doi.org/10.1016/j.jsg.2020.104069

Ponte, F.C., Hashimoto, A.T., Dino, R., 1991. Geologia das bacias sedimentares mesozoicas do interior do nordeste do Brasil.

Ponte, F.C., Ponte Filho, F.C., 1996. Estrutura geológica e evolução tectônica da Bacia do Araripe. DNPM, Recife - PE, 68 p.

Pontes, C.C.C., Nogueira, F.C.C., Bezerra, F.H.R., Balsamo, F., Miranda, T.S., Nicchio, M.A., Souza, J.A.B., Carvalho, B.R.B.M., 2019. Petrophysical properties of deformation bands in high porous sandstones across fault zones in the Rio do Peixe Basin, Brazil. International journal of rock mechanics and mining sciences 114, 153-163. https://doi.org/10.1016/j.ijrmms.2018.12.009

Pourmalek, A., Newell, A.J, Shariatipour, S.M., Butcher, A.S., Milodowski, A.E., Bagheri, M., Wood, A.M., 2021. Deformation bands in high-porosity sandstones: Do they help or hinder CO2 migration and storage in geological formations? International Journal of Greenhouse Gas Control 107, 103292. https://doi.org/10.1016/j.ijggc.2021.103292

Qu, D., Tveranger, J., 2016. Incorporation of deformation band fault damage zones in reservoir models. AAPG Bulletin 100, 423-443. https://doi.org/10.1306/12111514166

Qu, D., Tveranger, J., Fachri, M., 2017. Influence of deformation-band fault damage zone on reservoir performance. Interpretation 5, 41-56. http://dx.doi.org/10.1190/INT-2016-0229

Ramos, G.V., Vasconcelos, D.L., Marques, F.O., de Castro, D.L., Nogueira, F.C.C., Bezerra, F.H.R., Perez, Y.A.R., Souza, J.A.B., Medeiros, V.C., 2022. Relations between inherited basement fabric and fault nucleation in a continental setting: The Rio do Peixe Basin, NE Brazil. Marine and Petroleum Geology 139, 105635. https://doi.org/10.1016/j.marpetgeo.2022.105635

Renard, P., De Marsily, G. 1997. Calculating equivalent permeability: a review. Advances in water resources 20(5-6), 253-278. https://doi.org/10.1016/S0309-1708(96)00050-4

Roesner H.E., Lana C.C., Le Herissé A., Melo J.H.G. 2011. Bacia do Rio do Peixe (PB). Novos resultados biocronoestratigráficos e paleoambientais. In: Carvalho I.S., Srivastava N.K., Strohschoen Jr O., Lana C.C. (Eds.) Paleontologia: Cenários de Vida, 3. Rio de Janeiro. Interciência, 135-141.

Romano, C.R., Zahasky, C., Garing, C., Minto, J.M., Benson, S.M., Shipton, Z.K., Lunn, R.J., 2020. Subcore scale fluid flow behavior in a sandstone with cataclastic deformation bands. Water Resources Research American Geophysical Union (AGU) 56, 10–20. http://dx.doi.org/10.1029/2019wr026715

Rotevatn, A., Fossen, H., Hesthammer, J., Howell, J.A., 2007. Are relay ramps conduit for fluid flow? Structural analysis of a relay ramp in Arches National Park, Utah. In Lonergan, L., Jolly, R.J.H., Sanderson, D.J., Rawnsley, K. (Eds.), Fractured Reservoirs, Geological Society, London, Special Publications 270, 55-71. http://dx.doi.org/10.1144/GSL.SP.2007.270.01.04

Rotevatn, A., Tveranger, J., Howell, J.A., Fossen, H., 2009. Dynamic investigation of the effect of a relay ramp on simulated fluid flow: geocellular modelling of the Delicate Arch Ramp, Utah. Petroleum Geoscience 15, 45-48. https://doi.org/10.1144/1354-079309-779

Rotevatn, A., Fossen, H., 2011. Simulating the effect of subseismic fault tails and process zones in a siliciclastic reservoir analogue: Implications for aquifer support and trap definition. Marine and Petroleum Geology 28, 1648-1662. https://doi.org/10.1016/j.marpetgeo.2011.07.005

Saillet, E., Wibberley, C.A.J., 2013. Permeability and flow impact of faults and deformation bands in high-porosity sand reservoirs: Southeast Basin, France, analog. AAPG Bulletin 97, 437-464. https://doi.org/10.1306/09071211191

Schueller, S., Braathen, A., Fossen, H., Tveranger, J., 2013. Spatial distribution of deformation bands in damage zones of extensional faults in porous sandstones: statistical analysis of field data. Journal Structural Geology 52, 148-162. https://doi.org/10.1016/j. jsg.2013.03.013

Sénant, J., Popoff, M., 1991. Early Cretaceous extension in northeast Brazil related to the South Atlantic opening. Tectonophysics 198, 35-46. https://doi.org/10.1016/0040-1951(91)90129-G

The geometry and thickness of deformation-band fault core and its influence on sealing characteristics of deformation-band fault zones. AAPG Memoir 85, 181-195. https://doi.org/10.1306/1033723M853135

Sigda, J.M., Goodwin, L.B., Mozley, P.S., 1999. Permeability alteration in small-displacement faults in poorly lithified sediments: Rio Grande Rift, Central New Mexico. Faults and Subsurface Fluid Flow in The Shallow Crust. American Geophysical Union 113, 51–68. http://dx.doi.org/10.1029/gm113p0051

Sigda, J.M., Wilson, J.L., 2003. Are faults preferential flow paths through semiarid and arid vadose zones? Water Resources Research 39(8), 1225–1239. https://doi.org/10.1029/2002WR001406

Silva, J.G.F da., Córdoba, V.C., Caldas, L.H.O., 2014. Proposta de novas unidades litoestratigráficas para o Devoniano da Bacia Rio do Peixe, Nordeste do Brasil. Brazilian Journal of Geology 561-578. https://doi.org/10.5327/Z23174889201400040004

Silva, J.P., Gomes, I.F., Santos, R.F.V.C., Miranda, T.S., Guedes, R.P., Barbosa, J.A., Guimarães, E.X., Beserra, L.B., Guimarães, L.J.N., 2021. Topological analysis of fracture networks integrated with flow simulation models for equivalent fracture permeability estimation. Journal of Structural Geology 147, 104338. https://doi.org/10.1016/j.jsg.2021.104338

Silva, M.E., Nogueira, F.C.C., Pérez, Y.A., Vasconcelos, D.L., Stohler, R.C., Sanglard, J.C.D., Balsamo, F., Bezerra, F.H.R., Carvalho, B.R.B.M., Souza, J.A.B., 2022. Permeability modeling of a basin-bounding fault damage zone in the Rio do Peixe Basin, Brazil. Marine and Petroleum Geology 135, 105409. https://doi.org/10.1016/j.marpetgeo.2021.105409

Szatmari, P., Françolin, J.B.L., Zanotto, O., Wolff, S., 1987. Evolução tectônica da margem equatorial brasileira. Revista Brasileira de Geociências 17, 180-188.

Torabi, A., Fossen, H., 2009. Spatial variation of microstructure and petrophysical properties along deformation bands in reservoir sandstones. AAPG Bulletin 93, 919-938. https://doi.org/10.1306/03270908161

Torabi, A., Fossen, H., Braathen, A., 2013. Insight into petrophysical properties of deformed sandstone reservoirs. AAPG Bulletin 97, 619-637. https://doi.org/10.1306/10031212040

Torabi, A., Ellingsen, T.S.S., Johannessen, M.U., Alaei, B., Rotevatn, A., Chiarella, D., 2020. Fault zone architecture and its scaling laws: where does the damage zone start and stop? Geological Society, London, Special Publications 496, 99-124. https://doi.org/10.1144/SP496-2018-151

Torabi, A., Balsamo, F., Nogueira, F.C.C., Vasconcelos, D.L., Silva, A.C.E., Bezerra, F.H.R., Souza, J.A.B., 2021. Variation of thickness, internal structure and petrophysical properties in a deformation band fault zone in siliciclastic rocks. Marine and Petroleum Geology 133, 105297. https://doi.org/10.1016/j.marpetgeo.2021.105297

Tueckmantel, C., Fisher, Q., Grattoni, C., Aplin, A., 2012. Single and two-phase fluid flow properties of cataclastic fault rocks in porous sandstone. Marine and Petroleum Geology 29, 129-142. https://doi.org/10.1016/j.marpetgeo.2011.07.009

Underhill, J.R., Woodcock, N.H., 1987. Faulting mechanisms in high porosity sandstones: New Red Sandstone, Arran, Scotland. In: Jones, M.E., Preston, R.M.F., (Eds.) Deformation of sediments and sedimentary rocks. Geological Society, London, Special Publication 29, 91-105. https://doi.org/10.1144/GSL.SP.1987.029.01.09

Unsal, E., Matthai, S.K., Blunt, M.J., 2010. Simulation of multiphase flow in fractured reservoirs using a fracture-only model with transfer functions. Computational Geosciences 14, 527-538. https://doi.org/10.1007/s10596-009-9168-4

Vasconcelos, D., Marques, F. O., Nogueira, F. C. C., Perez, Y. A. R., Bezerra, F. H. R., Stohler, R. C., Souza, J. A. B., 2021. Tectonic inversion assessed by integration of geological and geophysical data: The intracontinental Rio do Peixe Basin, NE Brazil. Basin Research 33, 705-728. https://doi.org/10.1111/bre.12491

Wilkins, S.J., Davies, R.K., Naruk, S.J., 2019. Subsurface Observations of Deformation Bands and Their impact on Hydrocarbon Production Within the Holstein field, Gulf of Mexico, USA. Geological Society, London, Special Publications 496, 223-252. https://doi.org/10.1144/SP496-2018-139

Zambrano, M., Tondi, E., Mancini, L., Arzilli, F., Lanzafame, G., Materazzi, M., Torrieri, S., 2017. 3D Pore-network quantitative analysis in deformed carbonate grainstones. Marine and Petroleum Geology 82, 251-264. https://doi.org/10.1016/j.marpetgeo.2017.02.001

Zambrano, M., Tondi, E., Mancini, L., Lanzafame, G., Trias, F.X., Arzilli, F., Materazzi, M, Torrieri, S., 2018. Fluid flow simulation and permeability computation in deformed porous carbonate grainstones. Advances in Water Resources 115, 95-111. https://doi.org/10.1016/j.advwatres.2018.02.016

Zou, C., Zhu, R., Liu, K., Su, L., Bai, B., Zhang, X., Yuan, X., Wang, J. 2012. Tight gas sandstone reservoirs in China: characteristics and recognition criteria. Journal of Petroleum Science and Engineering88, 82-91. https://doi.org/10.1016/j.petrol.2012.02.001

Zuluaga, L.F., Rotevatn, A., Keilegavlen, E., Fossen, H., 2016. The impact of deformation bands on simulated fluid flow within fault-propagation fold trap types: lessons from the San Rafael Monocline, Utah (USA). AAPG Bulletin 100, 1523-1540. https://doi.org/10.1306/04151614153

Capítulo 5

Fluid flow in a deformation band fault zone in Brazil northeast: Implications for modelling and numerical simulation in Siliciclastic rocks

This manuscript was submitted to the Journal Marine and Petroleum Geology on November 27, 2024. Submission code: JMPG-D-24-01809

5. Fluid flow in a deformation band fault zone in Brazil northeast: Implications for modelling and numerical simulation in Siliciclastic rocks

Franklyn Macedo de Souza [a]; Igor Fernandes Gomes [a]; Francisco Cézar Costa Nogueira [b]; David Lino Vasconcelos [b]; Yoe Alain Reyes Perez [c]; Amanda Evaristo [d]; Jorge André Braz de Souza [e] ; Gabriel Honorio [b]; José Agnelo Soares [b]

[a] Civil Engineering Post-Graduation Program, Federal University of Pernambuco, Recife, PE, 50740-530, Brazil
[b] Federal University of Campina Grande, Campina Grande, PB, Brazil
[c] Federal University of Rio Grande do Norte, Natal, RN, Brazil
[d] Halliburton, Rio de Janeiro, Brazil
[e] Petrobras Research Center (CENPES), Rio de Janeiro, Brazil

Abstract

Deformation bands are known to affect petrophysical properties and the fluid flow of reservoirs. This study aims to model and simulate a deformation band fault zone in siliciclastic rocks in an outcrop in the Rio do Peixe Basin. We compiled previous structural and petrophysical data, combined with new data (permeability and porosity), and an electrical resistivity survey for subsequent inversion, obtaining porosity values, thus allowing the structural and petrophysical modeling for fluid flow numerical simulation. For the outcrop modeling, performed in finite elements, we used the fault facies analysis divided into five facies (H: >10 DB/m; M: 6-10 DB/m; L2: 3–5 DB/m; L1: 1–2 DB/m; and NS: 0 DB/m) with the predominance is of facies L1 and L2. The porosity and permeability analysis shows that values in the cluster region are lower than in the region between bands. The permeability reaches a reduction of up to 7 orders of magnitude when comparing the average value in the cluster and the average value in the region between bands. The high sampling rate of electrical resistivity data provided efficiency and lower costs compared to plug sample laboratory analyses, allowing porosity models in analogous outcrops. The numerical simulation showed that, depending on the well configuration, the clusters act partially as barriers and partially as conduits for fluid flow, varying according to the simulated flow scenario and the relative direction of the flow with respect to the structures. Therefore, this study contributes to understanding the behavior of deformation bands for fluid flow.

Keywords: Deformation bands, Porous sandstones, Permeability, Porosity, Modeling, Fluid flow.

5.1. Introduction

Deformation in porous sandstones is initially accommodated by the development of small-scale structures known as deformation bands (DB) (Fossen et al., 2007). These structures are known for local changes in the petrophysical, geomechanical, geometric, and textural properties of the host rocks (Fossen et al., 2007; Torabi et al., 2008; Pontes et al., 2019; Nogueira et al., 2021). DBs can occur hierarchically, such as an isolated band, commonly referred to as a single band, or they can coalesce to form band nucleations, termed clusters, or, in a more advanced state of deformation, develop into complex fault zones called slip surfaces (Fossen et al., 2007; Fossen and Bale, 2007). The fault zones composed of clusters and single bands are commonly considered barriers (baffles) to fluid flow in porous media (Torabi et al., 2021; Stohler et al., 2022) and can act as seals and/or traps within a petroleum system. Therefore, understanding their formation and growth processes is essential for an accurate representation of the hydraulic properties of fault zones in porous sandstone and carbonate reservoirs (Fossen and Bale, 2007; Ogilvie and Glover, 2001; Ballas et al., 2015; Souza et al., 2022).

One of the main problems with the presence of DBs in reservoirs is that they are not visible at seismic scale (Fossen et al., 2017), limiting their study to well analysis, specifically through core studies, since image and resistivity logs in wells are not capable of identifying these structures. Another commonly used method is the study of outcrop analogs, which provides the primary data source for understanding and parameterizing the presence of these features, enabling analysis at various observation scales (Griffiths et al., 2016; Qu et al., 2017; Silva et al., 2022; Palhano et al., 2023). This allows for an accurate representation of the distribution of these structures in subsurface reservoir models. The distribution of these structures allows the construction of a fault facies model where, through P10 (number of bands per meter), it is possible to classify the facies of a given point, considering the approach proposed by Qu and Tveranger (2016). Outcrops as reservoir analogs are applicable when they can be considered geologically compatible (Howell et al., 2014; Hurst et al., 2016). In this context, sandstones from the Antenor Navarro Formation in the Rio do Peixe Basin (RPB) have frequently been used as an important analog for the study of compartmentalized siliciclastic reservoirs (e.g., Araujo et al., 2018; Maciel et al., 2018; Nicchio et al., 2018; Pontes et al., 2019; Nogueira et al., 2021; De Souza et al., 2021; Oliveira et al., 2022; Silva et al., 2022; Souza et al., 2022; Palhano et al., 2023).

In a recent publication, Torabi et al. (2021) conducted a characterization of a DB fault zone present in the RPB (Figure 1A). This study complemented a prior structural characterization by De Sousa et al. (2021), identifying the geometry along the fault. Torabi et al. (2021) also characterized the variation in permeability and porosity along and across the fault. This study concluded that fluid flow tends to be more restricted across the central portion of the fault and to increase cross-fault flow through adjacent connected segments. This fault zone is composed of several linkage zones, which have been described in the literature as areas that tend to be preferential pathways for fluid flow (e.g., Rotevatn et al., 2007, 2009; Fachri et al., 2013a,b).

The main objectives of this work were to build an outcrop-scale model of this DB fault zone investigated by Torabi et al. (2021) and incorporate new permeability data along with an inversion of resistivity data obtained from the outcrop. We intend to analyze: (1) How can an inversion of a resistivity survey be used to build porosity models. (2) How fault facies may be used to understand the distribution of deformation along and across a DB fault zone. (3) The potential of a DB fault zone to act as a seal. (4) The roles of linkage zones as preferential pathways for fluid flow.

To achieve this purpose, we used structural and petrophysical data (porosity and permeability) published by Torabi et al. (2021) and Silva (2022). In addition, we acquired new in-situ permeability data to improve the distribution of these properties and conducted a 3D resistivity survey to perform an inversion that associates this geophysical survey with porosity data. The fundamental purpose is to estimate the subsurface resistivity distribution at various investigation depths. According to Orellana (1972), the recorded value of this potential difference and the associated current is related to the apparent resistivity of the soil and the geometric arrangement of the electrodes, with the depth of investigation being directly proportional to the spacing between the current electrodes. Finally, we performed structural modeling of the outcrop and petrophysical properties (porosity and permeability) to conduct a numerical fluid flow simulation analysis in the context of a DB fault zone.

5.2. Geological settings

The RPB (Figure 1A), located in northeastern Brazil, is part of a set of small to medium-sized intracontinental basins formed during the breakup of Pangea (Matos, 1992; Françolin et al., 1994; Nogueira et al., 2004, 2015). With an area of approximately 1,250 km², the RPB consists of three subsidence regions or sub-basins: Brejo das Freiras, Sousa, and Pombal (Françolin et al., 1994; de Castro et al., 2007; Nogueira et al., 2015; Ramos et al., 2024). These sub-basins include three half-grabens controlled by the Portalegre, Malta, and Rio Piranhas faults, which are brittle reactivations of the Portalegre, Patos, and Rio Piranhas shear zones, respectively, during the opening of the RPB in the Lower Cretaceous (~145-125 Ma) (de Castro et al., 2007; Nogueira et al., 2015; Nicchio et al., 2022; Ramos et al., 2022). Additionally, recent studies have reported that the RPB experienced light to moderate tectonic inversion along the major faults of the rift phase, associated with far-field stresses from the combined push of the Atlantic Ridge and Andean Orogeny (Nogueira et al., 2015; Vasconcelos et al., 2021; Bezerra et al., 2023). According to these studies, this deformation occurred during the post-rift phase of the RPB (80 Ma to the present). However, no specific period or possible cycles are well established due to the lack of datable post-rift units, fault rock dating data and because the stress field associated with the inversion has been the same throughout the post-rift phase (Nogueira et al., 2015; Vasconcelos et al., 2021).

Regarding the stratigraphic framework, the RPB is composed of fluvial, lacustrine, and alluvial fan deposits, named the Antenor Navarro Formation, Sousa Formation, and Rio Piranhas Formation (Figure 1B), respectively (Carvalho et al., 2013). These three formations constitute the lithostratigraphic unit known as the Rio do Peixe Group. In addition, recent studies have identified two new formations of Devonian age (~420-407 Ma) (Roesner et al., 2011; Silva et al., 2014; Vasconcelos et al., 2021; Rapozo et al., 2021). According to these authors, the Pilões and Triunfo Formations, which together form the Santa Helena Group, comprise siltstones and shales at the base (Pilões Formation) and quartz sandstones and conglomerates at the top (Triunfo Formation), both deposited in a fluvial-deltaic environment. Therefore, a significant depositional hiatus between the Lower Devonian and the Lower Cretaceous (rift phase) remains unclear and requires further study.

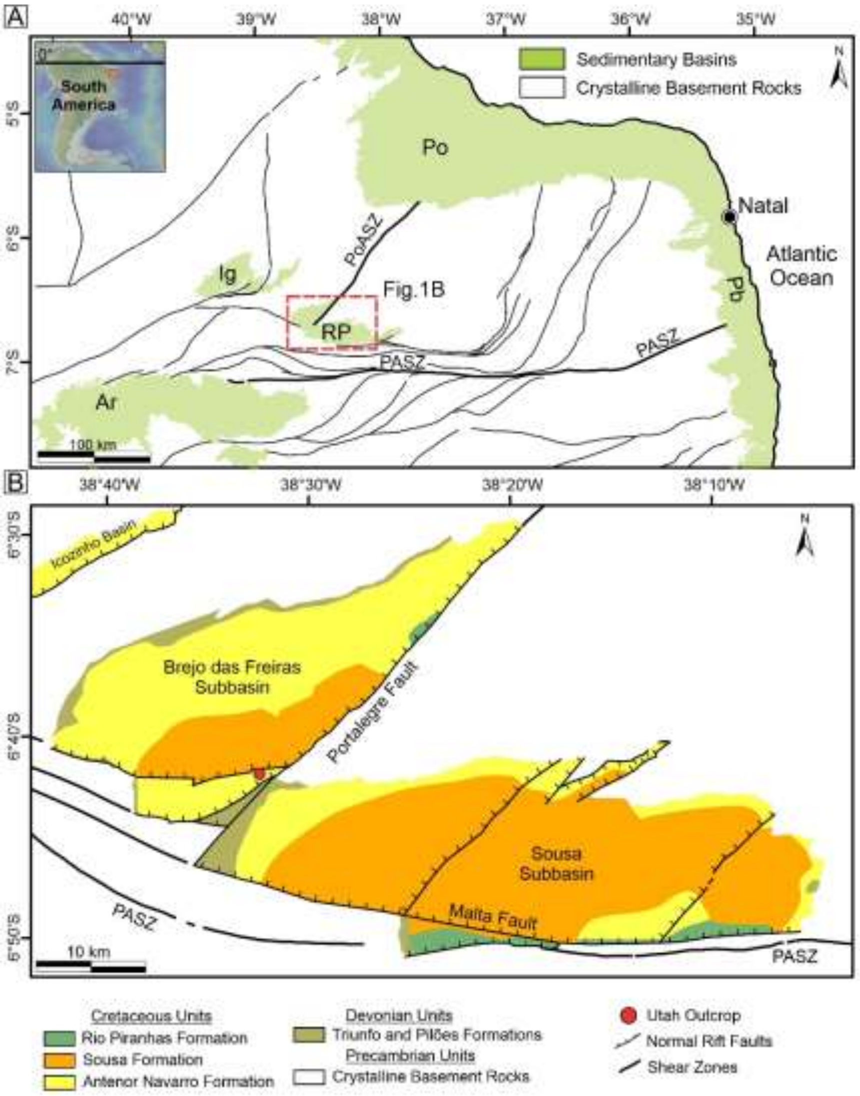

Figure 5.1. (A) Map of the major sedimentary basins in NE Brazil. Sedimentary basins: Ar = Araripe Basin; Ig = Iguatu Basin; Pb = Paraíba Basin; Po = Potiguar Basin; RP = Rio Peixe Basin. Shear zones: PSZ = Patos Shear Zone; PoASZ = Portalegre Shear Zone. (B) Geological-structural map of the Rio do Peixe Basin with the outcrop location analyzed in this study. Adapted from Françolin et al. (1994), Nogueira et al. (2015), and Freitas et al. (2023).

The study area focused on an outcrop in the Brejo das Freiras Sub-basin (red circle in Figure 1). This outcrop consists of conglomeratic arkosic sandstones from the

Antenor Navarro Formation, deposited during the syn-rift phase of the RPB that occurred in the Lower Cretaceous (~145-125 Ma). The outcrop features DBs in the form of clusters, with vertical exposure and relief enhancement relative to the adjacent rock of more than two meters in height, as well as DBs in the form of single faults (Pontes et al., 2019; De Souza et al., 2021; Torabi et al., 2021). This outcrop is located near two segments of the Portalegre Fault (Vasconcelos et al., 2021; Lucas et al., 2023; Ramos et al., 2024) with different orientations: NE–SW and E–W. Additionally, Pontes et al. (2019) classified the deformation in this outcrop as a single fault zone, which, according to these authors, consists of a fault zone with only one core and differs from complex fault zones with multiple fault cores. According to Torabi et al. (2021), this core is the main cluster of this outcrop.

5.3. Methodology

The methodology is divided into five steps: (1) Compilation of DB mapping (De Sousa et al., 2021); (2) Compilation and acquisition of petrophysical data (Febbrari, 2017; Torabi et al., 2021; Silva, 2022); (3) Acquisition of resistivity data; (4) Structural, sedimentary facies, and petrophysical modeling; and (5) Numerical fluid flow simulation.

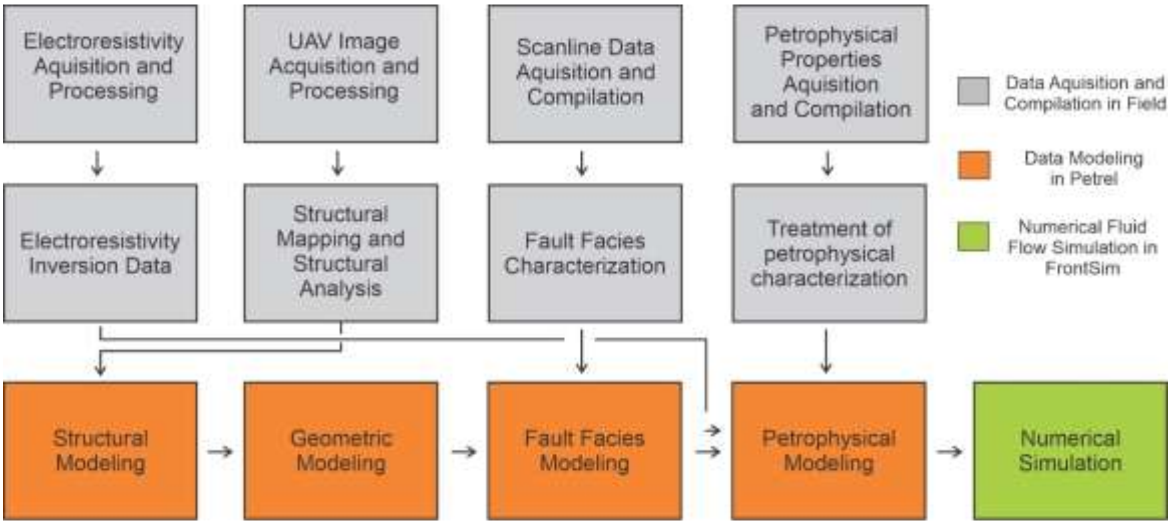

Figure 5.2. Flowchart with the activities developed for generating geological models and flow simulation.

5.3.1. Resistivity Model

A vertical electrical sounding (VES) survey was conducted with a multi-level gradient electrode arrangement to construct the resistivity model. The minimum electrode spacing was 10 meters. The equipment used was a single-channel resistivity meter, Bodenseewerk model 30L. This method investigates the electrical properties, measuring resistivity at different depths and applying an electric current to the ground through electrodes, varying the distance between them to obtain measurements that reflect changes in the geological layers.

Six 2D lines were conducted, three oriented approximately N-S and three oriented approximately E-W (Figure 3). E-W lines have a length of 250 meters. Two N-S lines are 200 meters long, while the other is 300 meters long. The reason for these differences is the difficulty of access caused by vegetation and/or topographic variations. After acquiring the VES data, the data were processed and inverted, generating 2D geoelectrical sections. The data were initially processed using Res2Dinv software, which is used to invert electrical resistivity data to obtain 3D models of the resistivity distribution. Then, the values were imported into the Voxler software, which allows for 3D visualization of the resistivity data using the geostatistical kriging method.

Figure 5.3. Map showing the location of the 2D sections (solid white lines) and the 3D block (dashed white square) related to the resistivity data overlaid on a drone image and Google Earth.

5.3.2. Structural Mapping

The verification of the structural mapping (De Souza et al., 2021) was carried out in the field with the support of high-resolution aerial drone images (Figure 4). The main bands of the outcrop were identified according to their direction. De Souza et al. (2021) used the interpretations of the linkage structures to characterize the DBs (Figure 4).

The structural characterization of the DBs in the field was based on fifteen scanlines compiled from Torabi et al. (2021). The number of bands per unit length, thickness, direction, and spacing between bands were measured on these scanlines.

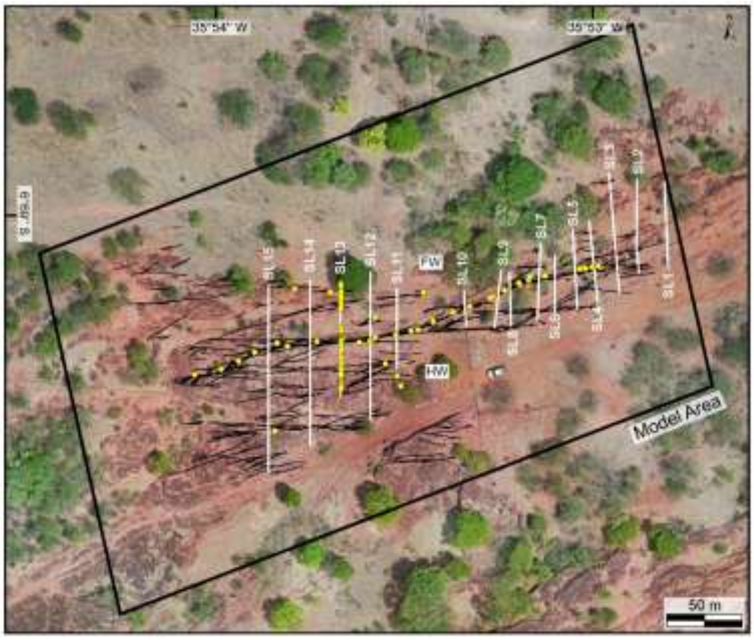

Figure 5.4. Drone image of the studied outcrop with the structural mapping from De Souza et al. (2021), with the interpretation of the DBs (black lines) and the location of the scanlines (white lines), along with the permeability measurements (yellow circles) used in this study, including those from Torabi et al. (2021). FW – Footwall; HW – Hanging Wall.

5.3.3. Fault Facies

After compiling the structural mapping, we conducted a fault facies classification. This characterization aims to analyze the spatial relationship of the fault facies perpendicular to the cluster and the proportion variation, which will be used as input data during petrophysical modeling (Silva, 2022). For the fault facies classification, five classes were defined based on the deformation density values obtained from the structural characterization and the classification proposed by Qu and Tveranger (2016), as follows: >10 DB/m, facies H; 6-10 DB/m, facies M; 3–5 DB/m, facies L2; 1–2 DB/m, facies L1; and 0 DB/m, facies ND. To better delineate the single structures, the original class L (1-5 DB/m) proposed by Qu and Tveranger (2016) was subdivided into two new classes (L1 and L2).

To model the fault facies, we determined that they would be governed by a set of discrete elements generated from the scanline's interpretation. The fault zone and the surrounding area were then delineated and analyzed through the scanlines that intersected it, considering the frequency of DBs per meter (P10) and the adapted classification from Qu and Tveranger (2016). After discretizing all the points, the area was modeled and populated using geostatistics in regions where data was unavailable.

5.3.4. Acquisition and Compilation of Permeability Data

The permeability data from this study used a portable air permeameter, TinyPerm 3 – New England Research, Inc. This equipment provides permeability values in the range of 10-4 to 10 Darcy and has an investigation depth of up to 4 times the inner radius of the rubber probe, which is 18 mm deep (Alikarami et al., 2013; Skurtveit et al., 2021). The compiled permeability data consist of 69 points (yellow circles in Figure 4), of which 40 are located in the cluster, 10 in single structures, and 19 in the space between bands. Additionally, new measurements were taken at 14 points: 2 in the space between bands, 2 in single bands, and 10 in the clusters. In total, we used 304 measurements in the cluster zone and 142 measurements in the space between bands. The measurements in the single bands were not considered for the model.

5.3.5. Porosity and Permeability Model

We used data obtained from VES to construct the porosity model. This method involves controlled vertical electric currents and measuring the resulting electrical resistivity. From the variations in resistivity, it is possible to infer the composition and structure of the geological layers.

The resistivity values were used in Archie's formula (Equation 2) to establish a correlation between porosity, water resistivity, formation resistivity, and water saturation. However, two exponents in the equation must be known: saturation (n) and cementation (m). Archie (1942) suggests that the parameters range between 1.8 and 2.0 for consolidated sandstones and approximately 1.3 for unconsolidated sandstones. Cementation coefficients can exceed 2.5 and even reach up to 5 in carbonates where the pore space is smaller (Tiab and Donaldson, 2004). Thus, a cementation coefficient two is commonly used in most studies.

A new term in the numerator of Archie's equation, known as the tortuosity factor, was introduced. This factor aims to correct the equation for the effects of variations in pore throat cementation, pore structure, and grain size (Winsauer, 1952).

Archie (1942) also demonstrated the relationship between water saturation and formation resistivity. In a formation containing oil and/or gas, both non-conductors of electricity, with a certain amount of water, resistivity is a function of water saturation. Thus, it was determined that the resistivity index (RI) would be the quotient between the total resistivity (Rt) and the resistivity of the rock fully saturated with water.

Eq. 1: $$IR = \frac{Rt}{Ro}$$

This index will be 1 when the formation is fully saturated with water.

In general, Archie's formula is expressed as follows:

Eq. 2: $$Sw^n = \frac{a}{\emptyset^m} * \frac{Rw}{Rt}$$

To arrive at the final result and obtain the porosity values (Ø), was assumed that the reservoir is fully saturated with water (Sw=1), that the tortuosity factor (a) is 0.82, that Rw (water resistivity) is known from the pumping test conducted in the same outcrop, Rt is already available from the data inversion, m is the cementation exponent (assuming consolidated sandstone with m = 2), and n is related to the water saturation exponent.

For the porosity and permeability modeling in the Schlumberger Petrel® software, the workflow and routines were based on modifications to the classical steps well established by Pyrcz and Deutsch (2014), Ringrose and Bentley (2021), Stohler et al. (2022), and Silva et al. (2022).

The first step in generating the geological models involved inserting the point cloud data representing the topographic variations obtained through the drone (Figure 5A). Then, it was possible to select the study area (170 x 100 m, black rectangle in Figure 5A) and construct the model's top. A copy of the top surface was created and lowered 40 meters below, making this the model's base. This depth was defined based on the electrical resistivity survey, which identified the water level at approximately 40 meters. Only the structure identified as the main cluster in the structural mapping inside the model was inserted (Figure 5B).

Next, the 3D structural grid was constructed, and the main fault of the outcrop was incorporated into the model. Based on the structural analysis of the DBs, it was defined that the created model would have cells of 1 x 1 x 1 m (I, J, K); it would be divided into eight different vertical zones, and the faults inserted into the model would have an average dip of 80º, creating a grid with a total of 277,680 cells (Figure 5C). After, property scaling was performed. In this phase, the porosity and permeability were linked to points with attributes in a cell of the generated model. The software calculates the arithmetic mean of these point values for cells with two incident points. Geostatistical techniques are used to populate the model in locations where no data is available. Sequential Gaussian Simulations (SGS) were employed as the algorithm for this propagation, using a spherical variogram with an anisotropy range of 75/25/20, and the orientation of the principal direction is 81Az. Subsequently, the polygons resulting from the structural interpretation were used to create a geometric property model encompassing three distinct elements: E–W cluster, NE–SW cluster, and space between bands. The fault facies model was used as a guide for populating the properties model after this dispersion.

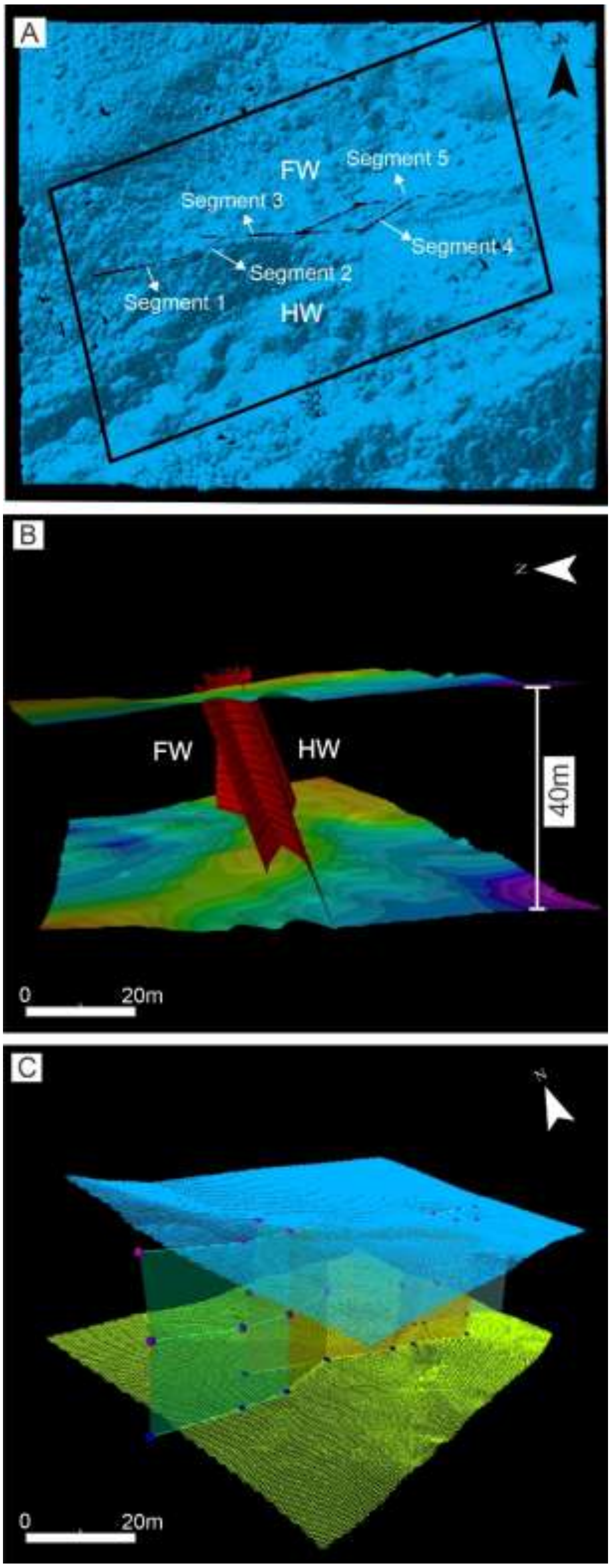

Figure 5.5. (A) Point cloud with altitude generated from drone image acquisition with the delineation of the modeled study area and segments of the main fault; (B) Study area located in the point cloud obtained from the drone survey; (C) Top and bottom of

the model with the location of the identified main cluster. FW – Footwall; HW – Hanging Wall.

The porosity values obtained through Archie's equation transformation of the electrical resistivity data were considered for constructing the porosity model. After conversion, these values were imported into the software as attribute points, totaling around 950,000 points. Spatially, each porosity value had coordinates (x, y, and z). The electrical resistivity survey did not cover some areas of the outcrop, and to populate the model, geostatistical methods were used, as in previous cases. Therefore, since this model contains almost 1 million points, it is safe to deduce that it is well-populated and distributed, justifying a reduced use of geostatistical methods.

Permeability data were distributed in the model, and SGS was used among the pixel-oriented stochastic algorithms for this purpose. The permeability model was adjusted to use the preferred direction of the DBs as a correction in positioning the spherical variogram. The data distribution followed a LogNormal distribution, thus widening the range without losing representativeness, and porosity was used as a secondary variable for co-kriging the model. Finally, vertical variations in permeability were considered to maintain high fidelity in the model.

5.3.6. Fluid flow simulation

For the numerical simulation, four distinct scenarios were simulated considering different arrangements of injection and production wells leading to scenarios with fluid flow: (1) crossing the cluster; (2) not crossing the cluster; (3) combining the two previous scenarios; and (4) crossing the cluster in two areas (Figure 6). Thus, the main aim of these scenarios is to analyze the sealing and flow-conducting potential of a DB fault zone, where the cluster corresponds to the fault (Pontes et al., 2019), as well as to assess the potential for preferential flow pathways in linkage zones (De Souza et al., 2021).

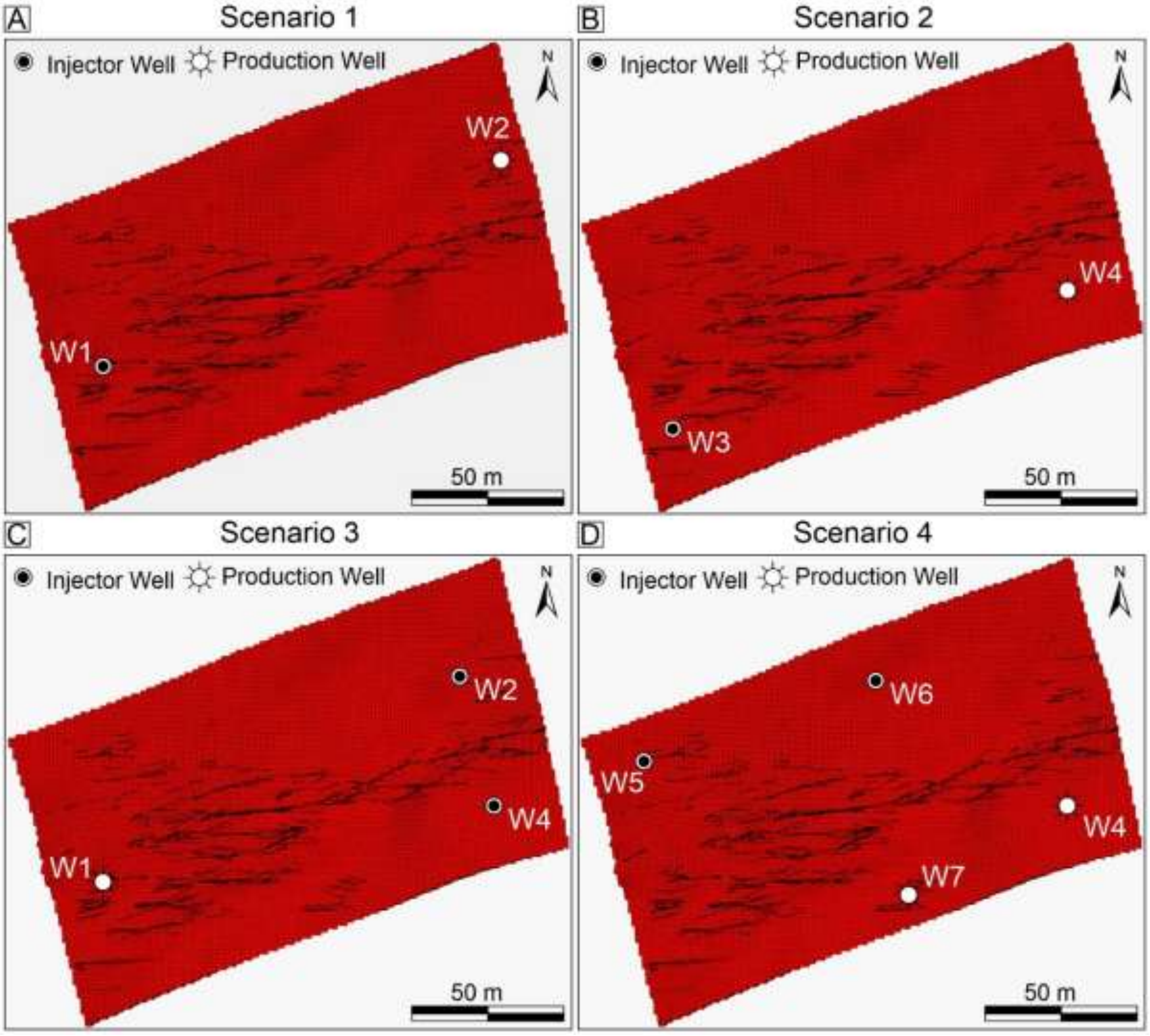

Figure 5.6. Numerical fluid flow simulation scenarios. (A) Scenario 1 with flow crossing the cluster; (B) Scenario 2 with flow not crossing the cluster; (C) Scenario 3 with flow combining Scenarios 1 and 2; (D) Scenario 4 with flow crossing the cluster zone at two distinct points.

We used the previously described porosity and permeability models as input data in the Schlumberger Frontsim Streamline Reservoir Simulation software. The adopted fluid model is a black-oil biphasic type, with the minimum reservoir pressure set equal to the bubble point pressure. These and other dynamic properties are summarized in Table 1.

Table 1. Dynamic flow simulation properties

Maximum Simulation Time	10 years	
Reporting Frequency	15 days	
Rock Compressivity	0,000056 1/bar	
Rock Reference Pressure	103,05 bar	
Oil API	26	
Bubble Point	0,5 bar	
Exp Corey	Water	4
	Oil-water	3
Saturation at Endpoints	Sorw	0,2
	Swcr	0,22
Relative Permeability Endpoints	Kromax	1
	Krw	0,8
Water Salinity	30000 ppm	
Top of the Model	295 m	
Water-oil Contact (OWC)	200 m	
Capillary Pressure (OWC)	0 bar	

Reference Depth	287 m	
Reference Pressure	103,05 bar	
Flow Rate	Injection	0,17 m^3/d
	Production	0,15 m^3/d
Pressure at the bottom of the well	Injectors	200 bar

5.4. Results

5.4.1. Mapping, Structural Analysis and Fault Facies

De Sousa et al. (2021) and Torabi et al. (2021) defined and mapped the fault zone in the study area regarding its main fault and its terminations. The present work utilized the results of the mapping, as well as the scanlines performed. According to these studies, the main cluster is composed of five segments (Figure 5A), with two segments-oriented NE-SW (segments 2 and 4) linking with three segments oriented E-W (segments 1, 3, and 5). Overall, the cluster has a preferred E-W orientation and has maximum and minimum thicknesses of 136 cm and 11.8 cm, respectively.

The frequency analysis of DBs from the scanlines was also compiled (Supplementary Material 1). The scanlines perpendicular to the main bands set showed frequencies ranging from 0 DB/m to 16 DB/m. The thickness of the bands varied between 0.215 mm and 80 mm, while the distance between bands ranged from a maximum of 769 cm to a minimum of 0.5 cm (Torabi et al., 2021).

Based on the classification by Qu and Tveranger (2016), we observed that the main cluster is predominantly composed of H, M, and L2, with facies H being the most prevalent among these three. To better delineate the single structures, the original class L (1-5 DB/m) proposed by Qu and Tveranger (2016) was subdivided into two new classes (L1 and L2), as approximately 45% of all deformation present in the outcrop analyzed in this study is concentrated in this class (Figure 7).

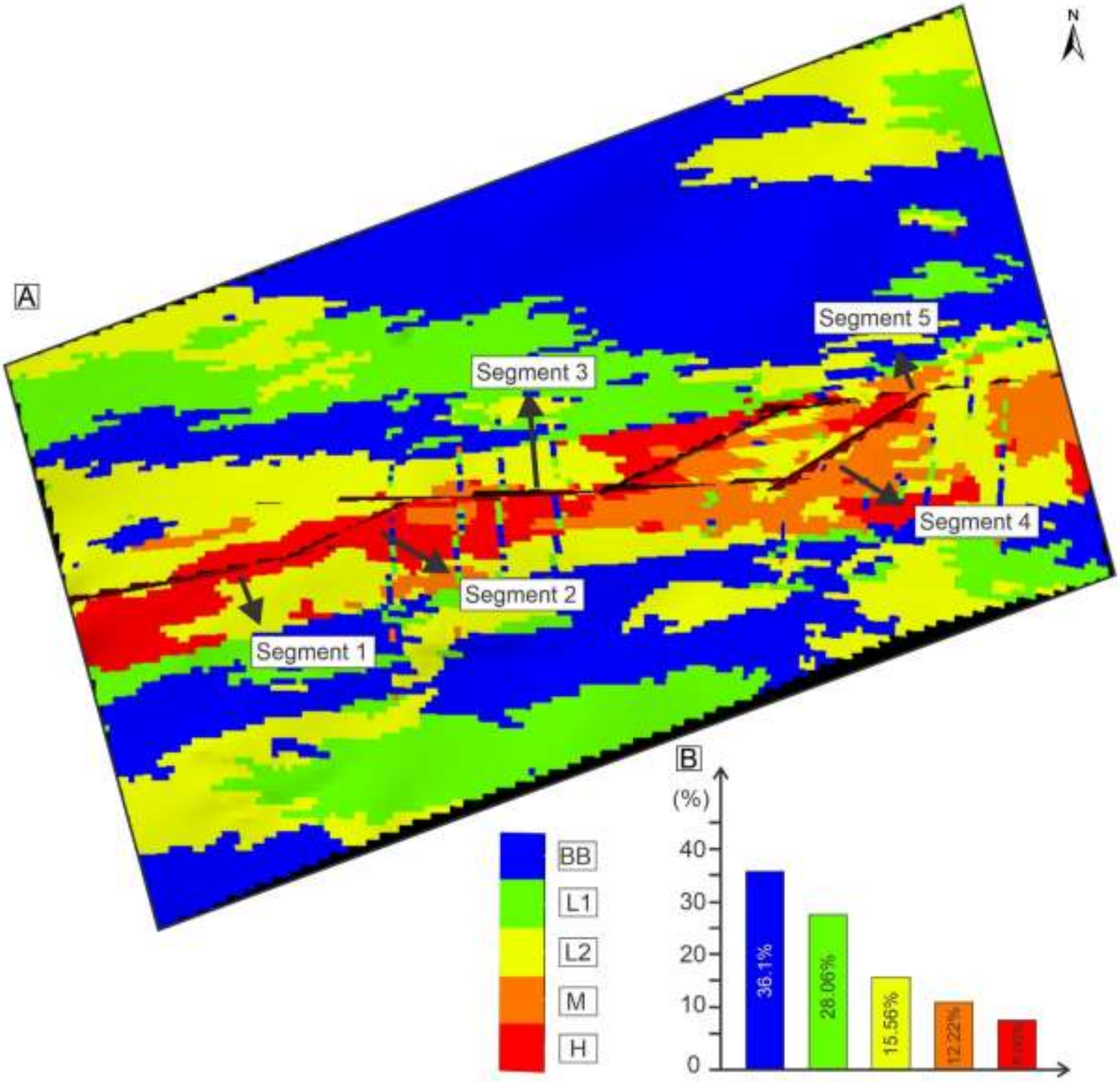

Figure 5.7. (A) Facies model constructed for the studied outcrop, where the distribution of facies and the delineation of the cluster and its segments can be observed. (B) Distribution of the modeled facies in the outcrop under study, with their respective percentages.

The cluster was defined as the starting point, and the fault facies were classified meter by meter along the scanlines. Finally, these classifications were integrated to determine the proportion of the observed facies classes with distance from the cluster. Facies H is present in the studied outcrop and can be observed only within the main cluster (Figure 8), while facies M is well represented in the cluster and its surroundings. The frequency of these facies decreases gradually with distance from the cluster.

Facies L2 shows similar behavior to facies M, increasing frequency as it approaches the clusters. However, it can also be observed in other areas of the outcrop. Facies L1 can be seen throughout the outcrop without a clear pattern.

On the other hand, Facies ND has the highest overall frequency in the outcrop, with its frequency increasing as we move away from the clusters. It is noted that, in some areas far from the main cluster, the presence of facies L2 is observed. This is due to the presence of mapped clusters not included in the model due to the lack of petrophysical data in these regions. Within the cluster region, point-wise, it is possible to see a reference of facies different from the interpolated data due to the geostatistical methods used. Different facies are observed from the interpolation at some points due to the macroregion having more influence than the measurement point.

5.4.2. Analysis of Electrical Resistivity

In the study area, several resistivity anomalies are observed (Figure 8). These anomalies are associated with regions with changes in porosity values or different fluids within the rock, such as the water table level. The map and three-dimensional model show the main cluster aligned with some portions of these high-resistivity zones. Additionally, we note that the resistivity anomalies are predominantly oriented in the E-W direction. However, when examining the anomalies in-depth, we observe that the contrast between resistivity anomalies marks the main cluster. For example, in a vertical view of the western portion of the study area (Figure 8B), anomalies around 175 ohm/m are in contact with anomalies around 100 ohm/m, indicating a possible continuation of the cluster map on the surface into the subsurface. Similarly, in the eastern portion of the study area (Figure 8C), anomalies around 225 ohm/m are in contact with anomalies close to 125 ohm/m, suggesting the location of the cluster in the subsurface.

Thus, the acquired electrical resistivity data were also used to construct the porosity model, providing good coverage of the proposed model.

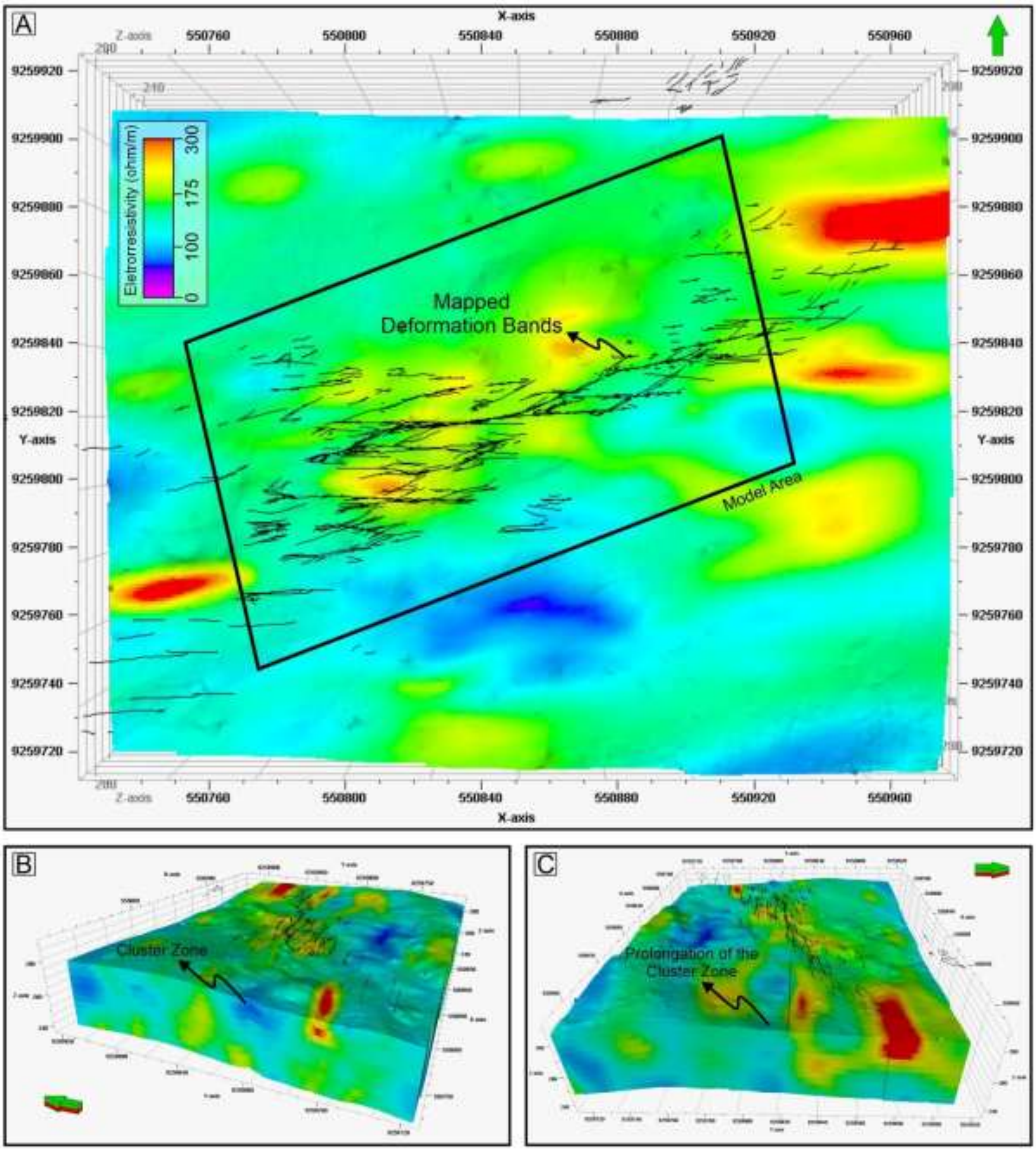

Figure 5.8. 3D resistivity model with views (A) in plan, (B) in the western portion of the cluster, and (C) in the eastern portion of the cluster.

5.4.3. Petrophysical Modeling

The generated porosity model (Figure 9 A and B) showed values ranging from 10% to 32%, with regions containing the cluster exhibiting reduced porosity values. In contrast, the regions between the bands displayed higher porosity, varying from 22%

to 32%. From the west to the central areas of the cluster, the porosity varies little (roughly 10 to 18%). However, in the east area of the cluster, the porosity reaches values close to 24%. This change is more effective in the east area, where the E-W segments of the cluster connect to the NE-SW segments.

Additionally, the highest values in this area (roughly 20%) are situated exactly in the area between these segments (see I in Figure 9B). Also, minor porosity values are associated with secondary clusters in the southern and northern parts of the model (see II and III in Figure 9B). The highest values in the spaces between bands are in the southern area (see IV in Figure 9B), away from the cluster zone. However, high values are also reported to be relatively close to the cluster zone (see IV in Figure 9B).

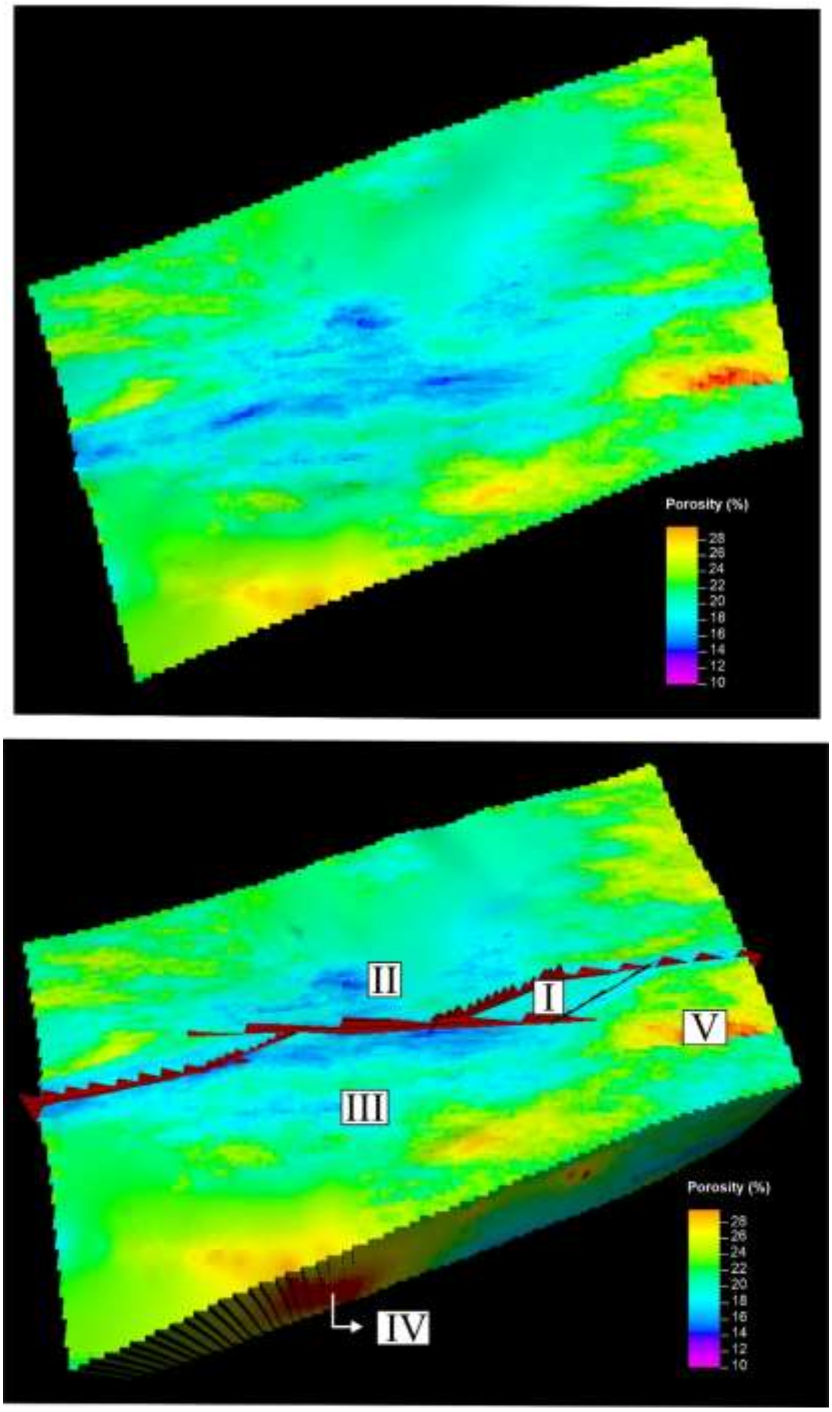

Figure 5.9. Generated porosity models for the study area, where (A) shows a top view with a surface view, and (B) displays a three-dimensional view of the model with porosity distribution and cluster location, highlighting its influence on the reduction of properties.

The permeability data were analyzed for the cluster and regions between bands (host rock). In this context, it is possible to observe that points in the cluster have lower permeability values than those between bands (Figure 10). This variation reaches two orders of magnitude when comparing the average values measured in the cluster (87.4 mD) with those measured in the region between bands (3,103.7 mD). However, the difference between these values reaches seven orders of magnitude when comparing the maximum value measured in the region between bands (34,496.67 mD) with the minimum value measured in the cluster (0.008 mD).

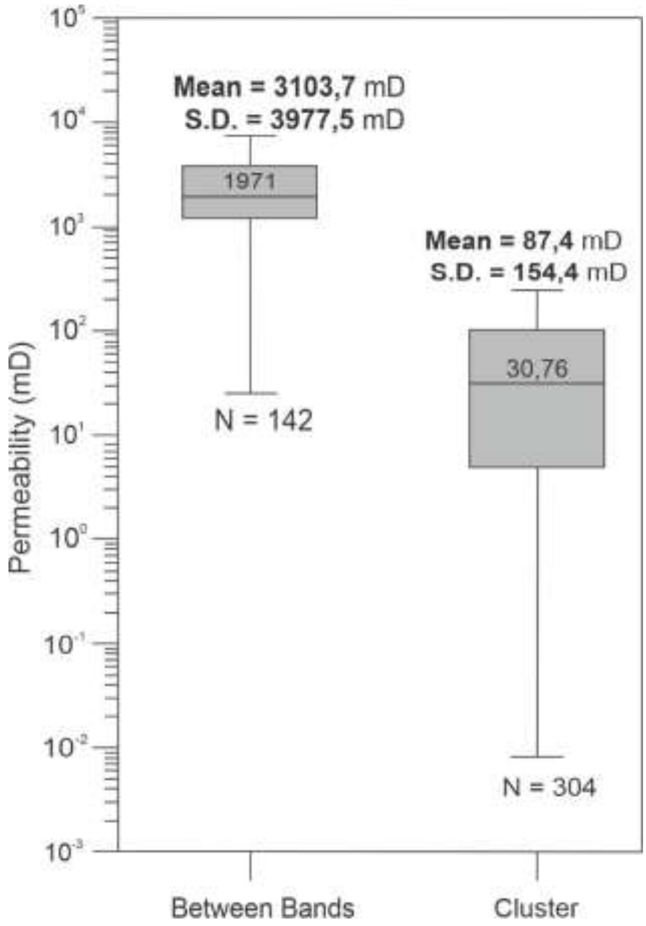

Figure 5.10. Graph of permeability variation for the cluster and the region between bands. The extremities from the boxes represent minimum and maximum values, and the center lines inside the boxes mean the median. S.D. – Standard Deviation.

The petrophysical properties of the model, permeability and porosity, behave heterogeneously, where near the cluster zone, values are low, and as one moves away from the cluster, the values increase. This contrast is very noticeable in Figure 11, where permeability values start around 200 mD and reach 2500 mD. In the central portion of the cluster (Figure 11A), some values deviate from the average values, which occurred due to a permeability acquisition line being collected at these points, where the cluster thickness is smaller, resulting in higher permeability values, as well as due to proximity to a linkage structure that might be increasing permeability in this region. In the areas farther from the cluster, values up to 10 times higher than those measured in the cluster are observed, demonstrating the influence of these structures in reducing permeability values. Vertically (Figure 11B), there is a very heterogeneous permeability distribution, where lower permeability regions are well-defined, as observed on the surface.

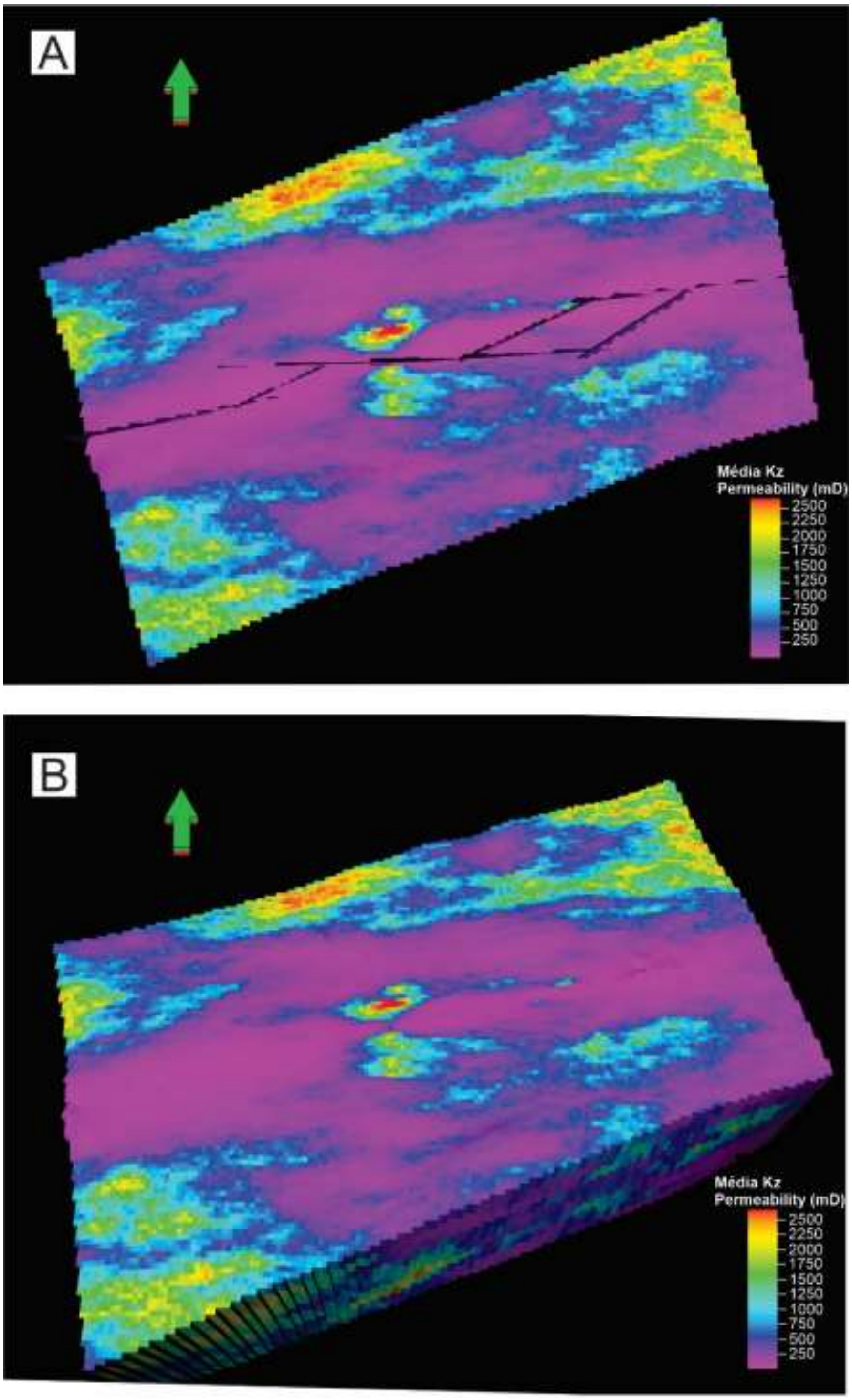

Figure 5.11. Permeability models generated for the study area, where (A) shows the top view with the cluster demarcation, and (B) provides a three-dimensional view of the model with permeability distribution along the Z-axis.

5.4.4. Numerical Fluid Flow Simulation

We performed a numerical fluid flow simulation of 4 scenarios to evaluate whether the DB fault zone acts as a conduit or barrier for fluid flow (Figures 12, 13, 14, and 15). Due to the model's dimensions (mesoscale/outcrop scale), the simulations of fluid injection had a maximum duration of 60 days. Therefore, we chose to display the stages every 5 days, where t=1 indicates the start of injection, t=2 indicates 5 days, and so on.

In the initial stages of Scenario 1 (P1 in Figures 12A, 12B, and 12C), the fluid flow tends to stay parallel to the cluster zone. By Stage 4 (Figure 12D and E), the fluid has crossed the cluster in two regions: the first near the injector well (P2 in Figure 12D) and the second in the central region of the cluster (P3 in Figure 12D). However, the fluid continued to advance eastward parallel to the cluster. In Stage 7 (Figure 12F), the fluid crosses the cluster through the linkage zone with its front P1, reaching the water breakthrough point after 30 days from the start of injection. The P2 fluid front reaches the producer well in 35 days (Figure 12H) and the P3 front in 40 days (Figure 12I). Additionally, we noted that an area between the injector well and the cluster did not experience water saturation, indicating that fluid flow in this area was ineffective (see I and II in Figure 12I).

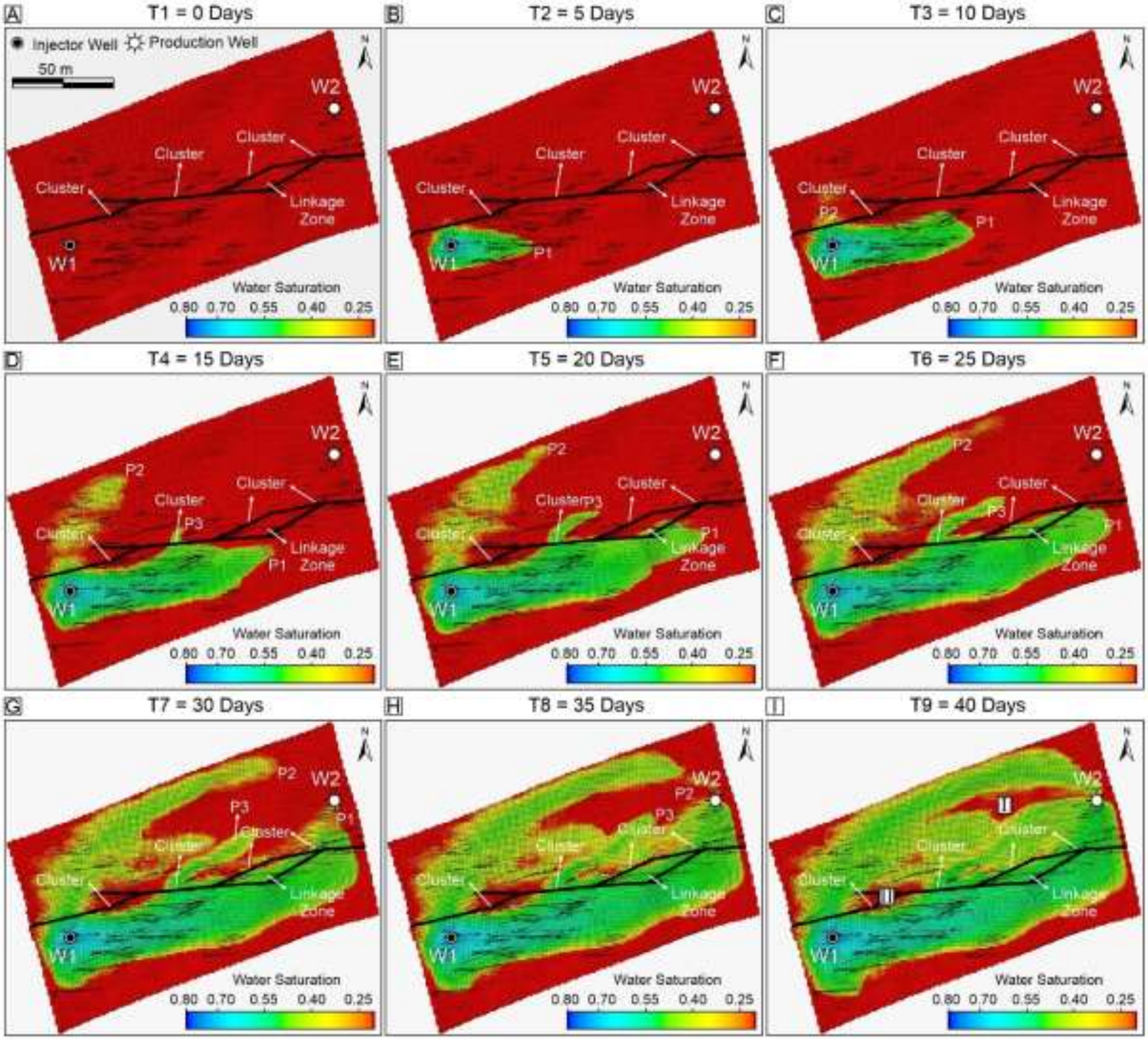

Figure 5.12. Fluid flow simulation results for Scenario 1 showing the water saturation for: (A) initial stage; (B) 5 days; (C) 10 days; (D) 15 days; (E) 20 days; (F) 25 days; (G) 30 days, where we can observe the start of water breakthrough with the P1 wavefront; (H) 35 days with the arrival of the P2 wavefront at the producer well; and (I) 40 days with the arrival of the P3 wavefront at the producer well.

At the start of Scenario 2 (Figure 13A), injection (Figure 13B) presents two wavefronts, P1 and P2. P1 skirts the cluster, while P2 skirts the edge of the model. In the third stage (Figure 13C e D), the P1 front is much more advanced than P2, with some fluid migrating towards the cluster and most flowing directly towards the producer well W4. The P2 front experienced a delay. In the final stage (Figure 13E), the fluid breaks through the cluster barrier in the central portion (P3 in Figure 13E) and reaches water breakthrough after 20 days from the start of injection, with the P1 and P2 fronts merging and no longer distinguishable from each other (P1/P2 in Figure 13E).

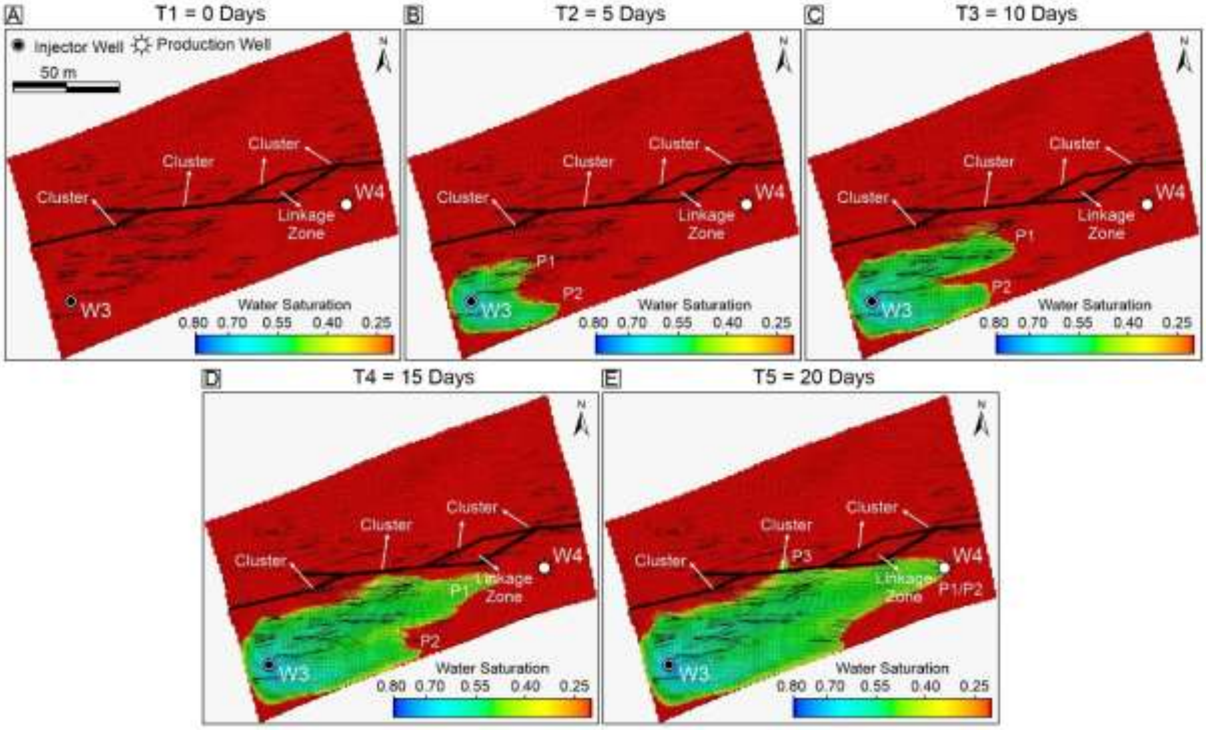

Figure 5.13. Fluid flow simulation results for scenario 2 showing the water saturation for: (A) initial stage; (B) 5 days; (C) 10 days; (D) 15 days; (E) 20 days, where we can observe the start of water breakthrough.

In Scenario 3 (Figure 14A), the front P1 advances toward the producer well more quickly than the front P2 (Figure 14B). Then, front P1 reaches water breakthrough within 15 days, while P2 continues to produce (Figure 14D). In the T5 and T6 (Figures 14E and 14F), front P2 continues advancing toward the well, but a new flow front, named P3, develops. In T9 (Figure 14I), a new front named P4 is formed, directed towards a central portion of the cluster. Then, fronts P2 and P4 cross the cluster in distinct areas, with P4 merging with front P1, making them indistinguishable (Figure 14J). In the final stage (Figure 14K), after 50 days of injection and 35 days after front P1, front P2 reaches the producer well, while front P3 does not. Additionally, several areas around the cluster stand out for not being saturated with water (e.g., I and II in Figure 14K).

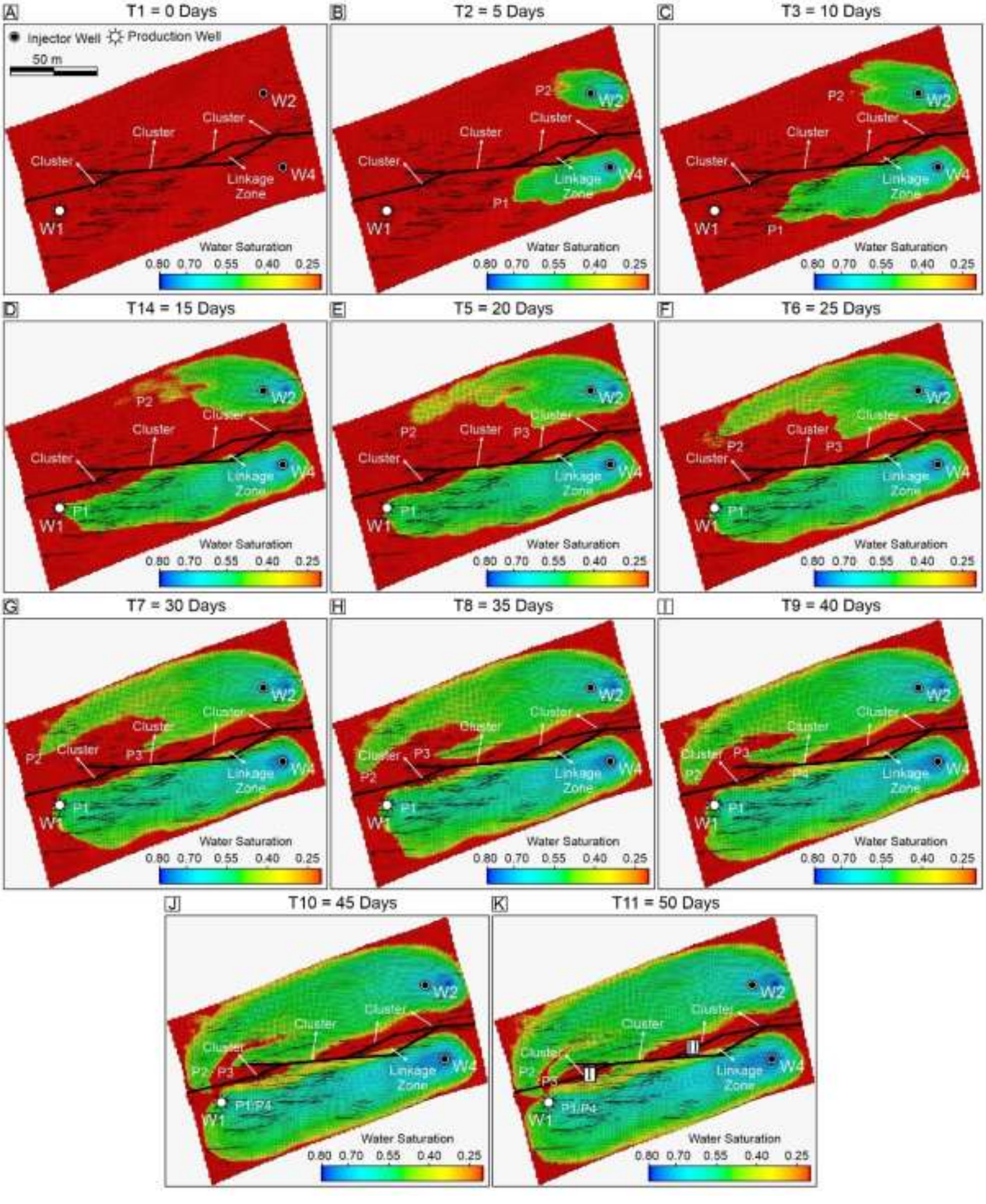

Figure 5.14. Fluid flow simulation results for Scenario 3 showing the water saturation for: (A) initial stage; (B) 5 days; (C) 10 days; (D) 15 days with the start of water breakthrough with front P1; (E) 20 days; (F) 25 days; (G) 30 days with fluid behavior after 30 days and the start of water breakthrough with front P1; (H) 35 days; (I) 40 days; (J) 45 days; (K) 50 days with fluid from well P2 reaching water breakthrough.

Scenario 4 (Figure 15A) shows that the flow fronts P2 and P3 from well W6 are advanced compared to front P1 from well W5, filling much of the northeastern portion (Figure 15B). In the next stage (Figure 15C), three wavefronts from well W6 (P2, P3, and P4) cross the cluster and two linkage zones, filling the entire space they occupy and reaching water breakthrough through front P3 after 10 days, with water reaching well W4. In the fourth stage (Figure 15D), front P2 also reaches the producer well, and front P1 crosses the cluster through a linkage zone towards producer well W7. Finally, in the fifth stage (Figure 15E), wavefront P1 reaches water breakthrough at well W7, and in the sixth stage (Figure 15F), the entire southeast portion of the cluster is filled. Additionally, when the fluid flow tends to be orthogonal to the cluster, this structure tends to behave as a partial barrier. For example, in Scenario 4 (Figure 15), where the fluid flows radially (I in Figure 15B) until it reaches the cluster zone (II in Figure 15C), after reaching it, the flow ceases to behave radially and becomes elongated near the cluster due to the cluster's characteristics partially blocking the continuity of the fluid. When analyzing the development of the wavefronts, it was observed that the front originating from well 6 develops more quickly than from well 5 (Figure 15B). This is due to the favorable petrophysical corridor, with low deformation, good porosity, and permeability, allowing for its expansion towards the linkage zones.

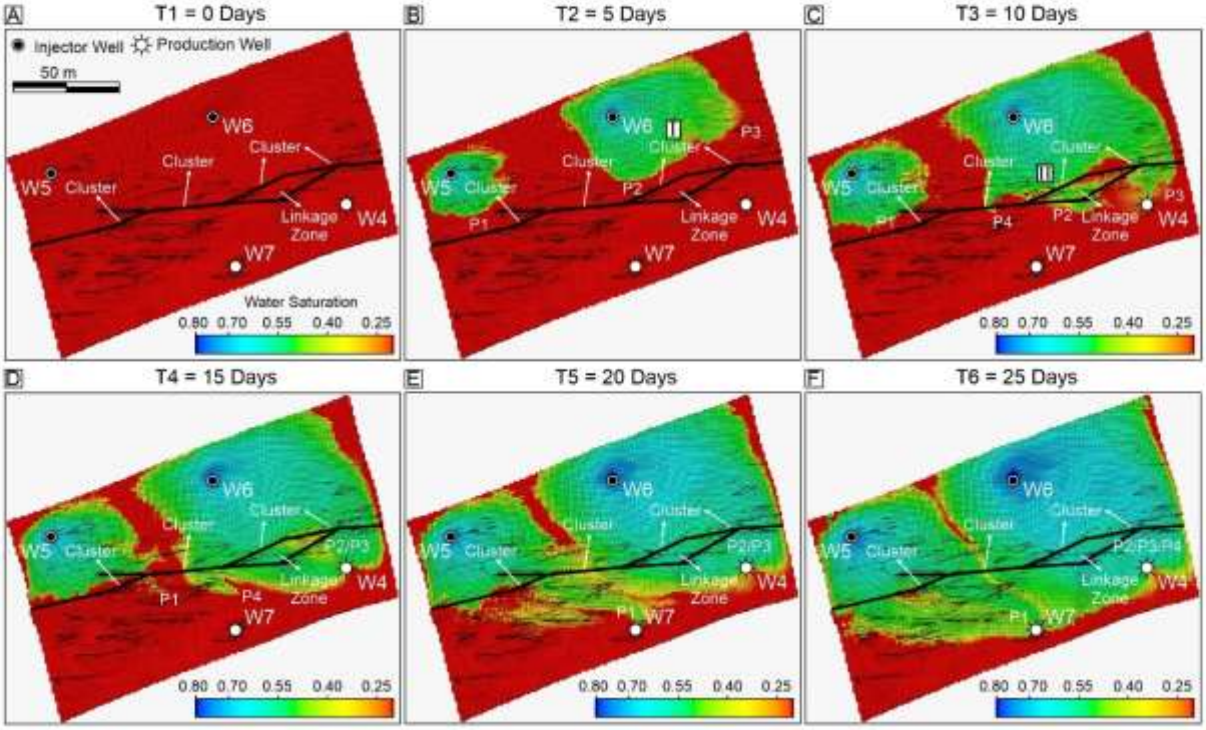

Figure 5.15. Fluid flow simulation results for scenario 4 showing the water saturation for: (A) initial stage; (B) 5 days; (C) 10 days with the onset of water breakthrough; (D) 15 days; (E) 20 days, with the model reaching water breakthrough from well W5; and (F) end of 25 days.

5.5. Discussions

5.5.1. Resistivity Inversion and Fault Facies Applied to Petrophysical Modelling

One of the biggest challenges in modeling lies in the strategy adopted for populating the petrophysical properties. Several studies have presented strategies based on the use of fault facies (e.g., Fachri et al., 2013a,b; Botter et al., 2016b; Qu and Tveranger, 2016; Silva et al., 2022), the calculation of equivalent permeability (e.g., Silva et al., 2022; Souza et al., 2022), and the influence of fault throw (e.g., Stohler et al., 2022). In our study, we applied fault facies modeling to understand the structural behavior of the studied fault zone (Figure 7). This model served as a guideline for populating the petrophysical properties. However, porosity was populated based on an inversion of electrical resistivity data using Archie’s formula, which was then used as a trend for populating the permeability values.

We compared our porosity values obtained from inversion with those derived from mercury intrusion analysis in the same study area. Torabi et al. (2021) identified that the porosity measured in plugs within the cluster region varies between 7% and 15%, with an average close to 11%. In our model, the porosity values near the cluster range from 14% to 18%, potentially exceeding 20% as one moves away from the cluster towards the undeformed host rock. Additionally, the relatively high porosity values exceeding 20% in the undeformed host rock align with the values presented by Nogueira et al. (2021), which surpass 20% and can reach values over 30% for undeformed host rock in another outcrop of the same lithological unit as our study. Therefore, we consider that our porosity modeling based on the inversion of electrical resistivity data is consistent with the results of Nogueira et al. (2021) and Torabi et al. (2021).

A significant differentiating factor in our study is the sampling rate. Using electrical resistivity data, our model was constructed with a high sampling rate, making it more efficient than plug samples for laboratory analyses. Additionally, the cost and time of acquiring electrical resistivity data are lower compared to laboratory analyses, allowing for studies of analogous outcrops from a modeling perspective. This procedure is similar to seismic data inversions, which use such workflow as a step towards permeability modeling with the porosity obtained through inversion as a trend (e.g., Khoshdel et al., 2022). However, we emphasize that it is essential to consider the influence of the aquifer on the electrical resistivity values, which can affect the porosity values obtained during the inversion process. In our case, the aquifer was estimated to be at a depth of 40 m, suggesting that it did not affect the shallower portions of the outcrop, where comparisons were made with results obtained from laboratory sample analyses.

Regarding permeability, the values recorded around the cluster range from 250 mD to 500 mD (Figure 10). Compared to the values reported by Torabi et al. (2021), which range from 0.1 mD to 75 mD, our results show a higher average by one to two orders of magnitude. This difference may be associated with the study methodology, where Torabi et al. (2021) used values from a mini gas permeameter with an investigation depth of about 18 mm. Our permeability values using a mini gas permeameter also show values below 1 mD and, therefore, are similar to previous studies.

Cluster zones are known as reduction of porosity and permeability zone, where several studies reported a significative reduction of these flow properties moving towards the deformation zones (Alikarami et al., 2013; Del Sole et al., 2020; Pizzati et al., 2020; Silva et al., 2022; Lucas et al., 2023). In their work, Torabi et al. (2021) focused on studying the most deformed zone of the outcrop, specifically the fault core. However, in measurements taken in the areas farther from the cluster, this study recorded values above 1000 mD and close to 10000 mD. These values are consistent with the average values observed in our permeability model (Figure 10). This behavior is also reported in other studies, which suggest an increase of up to 4 orders of magnitude moving away from the deformed zone (Pizzati et al., 2020; Silva et al., 2022; Lucas et al., 2023). Additionally, Torabi et al. (2021) noted that regions with fewer DBs tend to have higher permeability values. In our study, fault facies were used as a trend for modeling, incorporating these permeability effects. Therefore, using the scanlines from previous studies, classifying fault facies can contribute to a more accurate population of the petrophysical properties in our study area.

5.5.2. Influence of Linkage Structures on the Fluid Flow

Various published studies have allowed for some conclusions to be drawn, including the following: Logarithmic decay is observed in the frequency of the DBs as they move away from the core of the faults towards the protolith (Araujo et al., 2018; Silva et al., 2022); DBs occur in single fault zones (a single fault core) or complex zones (multiple fault cores) (Pontes et al., 2019); Control of grain size affects the thickness and frequency of DBs, such that clusters of DBs and sliding surfaces are observed only in coarse sandstones to conglomerates (Araujo et al., 2018); An increase in uniaxial compressive strength in the bands compared to the host rocks and the undeformed rock (Pontes et al., 2019; Oliveira et al., 2022); A reduction in porosity of up to two orders of magnitude compared to the undeformed rock (Pontes et al., 2019; Nogueira et al., 2021; Oliveira et al., 2022; Souza et al., 2022); A reduction in permeability of up to five orders of magnitude compared to the host rock and up to six orders of magnitude compared to the undeformed rock (Nogueira et al., 2021; Oliveira et al., 2022; Silva et al., 2022; Souza et al., 2022).

Studies with numerical simulations have shown that the presence of a cluster with DBs and the linkage zones between the different segments that form a cluster directly impact fluid flow behavior (Rotevatn et al., 2009; Medeiros et al., 2010; Botter et al., 2016a; Souza et al., 2022). Usually, the cluster zone tends to be a barrier to the fluid flow (or at least delay the flow), promoting a tortuous flow path when encountering the cluster, which tends to counter the structure (Medeiros et al., 2010; Torabi et al., 2021). However, in areas with the interaction between different fault segments, the linkage zones tend to be a conduit to the fluid flow (Rotevatn et al., 2009; Botter et al., 2016a).

In our study, when conducting a numerical simulation of fluid flow by inducing the flow to cross the cluster (Figures 12, 13, and 14), it is observed that the cluster behaves partially as a barrier but also partially as a conduit. For example, in Scenario 1, three main fluid flow wavefronts are formed. The first tends to align parallel to the cluster, indicating its role as a conduit for fluid flow. However, a second and third-wave front crosses the cluster. These second and third fluid flow wavefronts experienced delays of double and triple the time, respectively, compared to the first. This behavior, where the cluster directs the fluid flow parallel to its orientation, is also recorded in Scenarios 2 and 3 (Figures 13 and 14).

Similar results were obtained by Medeiros et al. (2010) and Souza et al. (2022). Medeiros et al. (2010) demonstrated the existence of hydraulic connectivity through a fault zone dominated by cataclastic DBs in the Tucano Basin, Northeastern Brazil. Meanwhile, Souza et al. (2022) analyzed the impact of DBs on fluid flow through 2D numerical modeling and simulation, using an equivalent permeability tensor in siliciclastic reservoirs. Both studies showed that clusters of DBs tend to act as partial barriers to fluid flow. This behavior is mostly controlled by the permeability contrast between the deformed and undeformed rock and by the direction of fluid flow relative to the strike of the structures (parallel flow or orthogonal flow).

Linkage zones are areas where two or more structures connect or Interact (Pollard and Aydin, 1984; Fossen and Rotevatn, 2016; Peacock et al., 2016), which may or may not be secondary to the main deformation. They are characterized by high structural complexity and are locations where fluid flow tends to cross (Kim et al., 2004; Lucas et al., 2023). These zones may experience an increase in effective permeability and pressure relief areas, causing fluids to seek out these low-pressure zones to move through (Rotevatn et al., 2009; Zuluaga et al., 2016; Botter et al., 2016a). However, they are not always conducive to fluid flow. For example, in Case 3, the linkage zones function as a partial barrier, directing fluid toward the production well. In this case, the injection wells, aligned vertically on opposite sides of the cluster, create a pressure differential in the region, preventing the sweep zones of the two wells from overlapping during the injection.

When linkage zones are present near injection wells, as exemplified in Scenario 3, it is observed that the fluid has greater difficulty crossing the zone towards the production well due to the high thickness and concentration of deformation in this region. This causes the injected fluid to flow parallel to the cluster, as seen in Scenario 2. It can also be observed that in Scenarios 1 and 3, the injection wells are close to the main cluster, with the main difference between them being the presence of a linkage zone, which is much closer in Scenario 3 and more distant in Scenario 1.

Another factor strongly influencing the results is the permeability contrast between the bands, cluster, and the space between bands. In the case of single-band structures, this contrast is lower. As presented by Rotevatn et al. (2009), DBs must have low permeability to affect fluid flow and reservoir productivity, as is the case with clusters. This behavior occurs because porosity and permeability tend to be higher as one moves away from the cluster and in the linkage zones of the segments that form this cluster. However, points of higher permeability are possible in the center of the cluster, as seen in all scenarios (see P3 in Figures 12 and 13 and P4 in Figures 14 and 15). We found that in the middle of the cluster, there is a zone of higher rock permeability; through this point, the fluid crosses at some point. This indicates that considering the homogeneous or constant permeability distribution along the fault zone can lead to a false barrier effect response.

Several factors, such as (i) the thickness of the damage zone, (ii) the ratio of fault facies (deformation intensity), (iii) the extent of the clusters of fault facies, and (iv) the frequency of DBs (distribution of deformation intensities), can explain this heterogeneous behavior in deformation zones (Fachri et al., 2013a,b). Furthermore, when this flow is biphasic, capillary pressure will also be relevant (Manzocchi et al., 2002; Fossen et al., 2007). Furthermore, permeability measurements show reduced link structure values compared to the central E-W segment. This result is consistent with the analyses conducted by Torabi et al. (2021), which highlight the direct proportional relationship between the frequency of bands and the thickness of the fault core with petrophysical variations. In other words, the thicker the fault core, the lower the permeability value.

For future work, it is suggested that the thickness of the damage zone in the model be increased, thus providing another control factor in the simulation. The addition of the damage zone thickness could be useful for analyzing the sealing capacity of faults composed of DBs and their impact on the productivity of oil wells (Harper and Moftar, 1985; Harper and Ludin, 1997; Rotevatn et al., 2009; Qu and Tveranger, 2016; Rotevatn et al., 2017; Stohler et al., 2022).

5.6. Conclusions

The present study performed structural and petrophysical modeling to analyze the fluid flow through numerical fluid flow simulations. These numerical simulations were used to understand the influence of DB fault zone during water flow in sandstone. Our data are consistent with several previous studies, which suggested that fluid flow in siliciclastic reservoirs is strongly affected by fault zones. However, heterogeneities in the cluster zone, such as the linkage zones and the cluster thickness, can act as preferred fluid flow paths. Based on this, the present study suggests the following notes:

• The main contrast of porosity along the cluster zone is recorded in the area of the linkage between the segments of the cluster. Regarding the permeability, the main contrast is recorded in the thinnest area of the cluster, as Torabi et al. (2021) reported. Also, high contrasts of permeability are reported close to the linkage zone.

• The high sampling rate of electrical resistivity data provided efficiency and lower costs compared to plug sample laboratory analyses, allowing for studies of analogous outcrops. Our porosity modeling based on the inversion of electrical resistivity data is consistent with the results of Nogueira et al. (2021) and Torabi et al. (2021).

• A porosity model derived from electrical resistivity data can be used as a tendency to populate the permeability models, similar to seismic inversion. Also, fault facies models could be useful in understanding the structural heterogeneity of the cluster zone and determining the areas where the cluster could act with higher rock permeability.

• Permeability values around the cluster were higher than previously reported, and a significant variation between values recorded around the cluster and in more distant areas was reported, highlighting the structural complexity of fault zones. Higher values were recorded in areas with fewer DBs and thinnest cluster zones. In this thinnest zone, a higher rock permeability was reported, and it is at this point that the fluid crosses in all our fluid flow simulation scenarios. This indicates that considering the homogeneous or constant permeability distribution along the fault zone can lead to a false barrier effect response.

• For the fluid flow analysis, we can observe that clusters of DBs act partially as barriers and partially as conduits for fluid flow, varying according to the simulated flow scenario and the relative direction of the flow with respect to the structures. The fluid flow generally aligns parallel to the cluster but faces additional difficulties when the flow is orthogonal.

• The hydraulic connectivity through fault zones is influenced by the connectivity of segments and linkage zones, where zones of high structural complexity can increase effective permeability.

Acknowledgements

We thank Petrobras, which funded the DEBRIP Project (TC-5850.0109438.18.9) coordinated by F.C.C. Nogueira (UFCG). F.M.S thanks the DEBRIP Project for his PhD Grant. Y.A.R.P., G.B.H., and D.L.V. thank the DEBRIP Project for their Research Grant. F.C.C. Nogueira and D.L. Vasconcelos are grateful to Conselho Nacional de Desenvolvimento Científico e Tecnológico (CNPq) for the research fellowships and associated grants. We thank Schlumberger for providing Petrel software license to the Federal University of Campina Grande (UFCG) during 2019-2022.

References

Alikarami, R., Torabi, A., Kolyukhin, D., Skurtveit, E., 2013. Geostatistical relationship between mechanical and petrophysical properties of deformed sandstone. International Journal of Rock Mechanics and Mining Sciences 63, 27–38. https://doi.org/10.1016/j.ijrmms.2013.06.002

Araujo, R.E.B., Bezerra, F.H.R., Nogueira, F.C.C., Balsamo, F., Carvalho, B.R.B.M., Souza, J.A.B., Sanglard, J.C.D., de Castro, D.L., Melo, A.C.C., 2018. Basement control on fault formation and deformation band damage zone evolution in the Rio do Peixe Basin, Brazil. Tectonophysics 745, 117–131. https://doi.org/10.1016/j.tecto.2018.08.011

Archie, G.E., 1942. The Electrical Resistivity Log as an Aid in Determining Some Reservoir Characteristics. 942054-G SPE Journal Paper. https://doi.org/doi.org/10.2118/942054-G

Ballas, G., Fossen, H., Soliva, R., 2015. Factors controlling permeability of cataclastic deformation bands and faults in porous sandstone reservoirs. Journla of Strucutral Geology 76, 1–21. https://doi.org/10.1016/j.jsg.2015.03.013

Bezerra, F.H.R., Marques, F.O., Vasconcelos, D.L., Rossetti, D.F., Tavares, A.C., Maia, R. P., de Castro, D.L., Nogueira, F.C.C., Medeiros, W.E., 2023. Review of tectonic inversion of sedimentary basins in NE and N Brazil: analysis of mechanisms, timing and effects on structures and relief. Journal of South American Earth Sciences 126, 104356 https://doi.org/10.1016/j.jsames.2023.104356

Botter, C., Cardozo, N., Hardy, S., Lecomte, I., Paton, G., Escalona, A., 2016a. Seismic characterization of fault damage in 3D using mechanical and seismic modelling. Marine and Petroleum Geology 77, 973–990. https://doi.org/10.1016/j.marpetgeo.2016.08.002

Botter, C., Cardozo, N., Lecomte, I., Rotevatn, A., Paton, G., 2016b. The impact of faults and fluid flow on seismic images of a relay ramp over production time. Petroleum Geoscience 23, 17–28. ttps://doi.org/10.1144/petgeo2016-027.

Carvalho, I.S., Mendes, J.C., Costa, T., 2013. The role of fracturing and mineralogical alteration of basement gneiss in the oil exudation in the Sousa Basin (Lower Cretaceous), Northeastern Brazil. Journal of South American Earth Sciences 47, 47–54. https://doi.org/10.1016/j.jsames.2013.06.001

de Castro, D.L., Oliveira, D.C., Castelo Branco, R.M.G., 2007. On the tectonics of the Neocomian Rio do Peixe rift basin, NE Brazil: lessons from gravity, magnetic and radiometric data. Journal of South American Earth Sciences 4, 184–202. https://doi.org/10.1016/j.jsames.2007.04.001

de Souza, D.H.S., Nogueira, F.C.C., Vasconcelos, D.L., Torabi, A., Souza, J.A.B., Nicchio, M.A., P´ erez, Y.A.R., Balsamo, F., 2021. Growth of cataclastic bands into a fault zone: a multiscalar process by microcrack coalescence in sandstones of Rio do Peixe Basin, NE Brazil. Journal of Structural Geology 146, 104315. https://doi.org/10.1016/j.jsg.2021.104315

Del Sole, L., Antonellini, M., Calafato, A., 2020. Characterization of sub-seismic resolution structural diagenetic heterogeneities in porous sandstones: combining ground-penetrating radar profiles with geomechanical and petrophysical in situ measurements (Northern Apennines, Italy). Marine and Petroleum Geology 117, 104375. https://doi.org/10.1016/j.marpetgeo.2020.104375

Fachri, M., Tveranger, J., Braathen, A., Schueller, S., 2013a. Sensitivity of fluid flow to deformation-band damage zone heterogeneities: a study using fault facies and truncated Gaussian simulation. Journal of Structural Geology 52, 60–79. https://doi.org/10.1016/j.jsg.2013.04.005.

Fachri, M., Rotevatn, A., Tveranger, J., 2013b. Fluid flow in relay zones revisited: towards an improved representation of small-scale structural heterogeneities in flow models. Marine and Petroleum Geology 46, 144–164. https://doi.org/10.1016/j.marpetgeo.2013.05.016.

Febbrari, C., 2017. Fault Zone Petrophysical Properties in Poorly Lithified Sandstone of the Rio Do Peixe Basin, Brazil. Master thesis. University of Parma, Italy.

Fossen, H., Bale, A., 2007. Deformation bands and their influence on fluid flow. AAPG (Am. AAPG Bulletin 91, 1685–1700. https://doi.org/10.1306/07300706146.

Fossen, H., Rotevatn, A., 2016. Fault linkage and relay structures in extensional settings – a review. Earth-Science Reviews 154, 14–28. https://doi.org/10.1016/j.earscirev.2015.11.014

Fossen, H., Soliva, R., Ballas, G., Trzaskos, B., Cavalcante, C., Schultz, R.A., 2017. A review of deformation bands in reservoir sandstones: geometries, mechanisms and distribution. In: Ashton, M., Dee, S.J., Wennberg, O.P. (Eds.), Subseismic-Scale Reservoir Deformation, 459. Journal of Geological Society of London, Special Publications, 9–33. https://doi.org/10.1144/SP459.4

Françolin, J.B.L., Cobbold, P.R., Szatmari, P., 1994. Faulting in the early cretaceous Rio do Peixe Basin (NE Brazil) and its significance for the opening of the atlantic. Journal of Structural Geology 16, 647–661. https://doi.org/10.1016/0191-8141(94)90116-3

Freitas, R.B.R.M., Nogueira, F.C.C., Vasconcelos, D.L., Honório, G.B., Nicchio, M.A., Stohler, R.D.C., Souza, J.A.B., 2023. 3D topological analysis in deformation bands: Insights for structural characterization and impact on permeability. Journal of Structural Geology 176, 104959. https://doi.org/10.1016/J.JSG.2023.104959

Griffiths, J., Faulkner, D.R., Alexander, P.E., Worden, R.H., 2016. Deformation band development as a function of intrinsic host-rock properties in Triassic Sherwood Sandstone. Geological Society, London, Special Publications 435, 161–176. https://doi.org/10.1144/SP435.11

Harper, T.R, Ludin, E.R., 1997. Fault seal analysis: reducing our dependence on empiricism. Hydrocarbon Seals - Importance for Exploration and Production. Norwegian Petroleum Society Special Publications 7, 149–164. https://doi.org/10.1016/S0928-8937(97)80013-6

Harper, T.R., Moftah, I., 1985. Skin effect and completion options in the Ras Budran Reservoir. In: Society of Petroleum Engineers Middle East Oil Technical Conference and Exhibition. SPE, 13708, 211–226. https://doi.org/10.2118/13708-MS

Howell, J.A., Martiniuis, A.W., Good, T.R., 2014. The application of outcrop analogues in geological modelling: A review, present status and future outlook. Geological Society, London, Special Publications 387, 1–25. https://doi.org/10.1144/SP387.12

Hurst, A., Huuse, M., Duranti, D., Vigorito, M., Jameson, E., Schwab, A., 2016. Application of outcrop analogues in successful exploration of a sand injection complex, Volund Field, Norwegian North Sea. Geological Society Special Publication 436, 75–92. https://doi.org/10.1144/SP436.3

Khoshdel, H., Javeherian, A., Saberi, M.R., Varnousfaderani, S.R., Shabani, M., 2022. Permeability estimation using rock physics modeling and seismic inversion in a carbonate reservoir. Journal of Petroleum Science and Engineering 219, 111128. https://doi.org/10.1016/j.petrol.2022.111128

Kim, Y.S., Peacock, D.C.P., Sanderson, D.J. (2004). Fault damage zones. Journal of Structural Geology 26, 503–517. https://doi.org/10.1016/j.jsg.2003.08.002

Lucas, L.C.V., Vasconcelos, D.L., Balsamo, F., Silva, M.E., Nogueira, F.C.C., Stohler, R.C., Bezerra, F.H.R., Honório. G.B., Nicchio, M.A., Vaz, I.C., Souza, J. A. B. (2023). Interaction and linkage of basin-boundary fault segments control deformation bands distribution and damage zone permeability. Journal of Structural Geology 176, 104958. https://doi.org/10.1016/j.jsg.2023.104958

Maciel, I. B., Dettori, A., Balsamo, F., Bezerra, F. H. R., Vieira, M. M., Nogueira, F. C. C., Salvioli-Marini, E., & Sousa, J. A. B. (2018). Structural control on clay mineral authigenesis in faulted arkosic sandstone of the Rio do Peixe Basin, Brazil. Minerals 8, 408. https://doi.org/10.3390/min8090408

Manzocchi, T., 2002. The connectivity of two-dimensional networks of spatially correlated fractures. Water Resources Research 38, 1–20. ttps://doi.org/10.1029/2000WR000180

Matos, R.M.D. 1992. The Northeastern Brazilian Rift System. Tectonics 11, 766–791. https://doi.org/10.1029/91TC03092

Medeiros, W.E., do Nascimento, A.F., Alves da Silva, F.C., Destro, N., Demétrio, J.G.A., 2010. Evidence of hydraulic connectivity across deformation bands from field pumping tests: two examples from Tucano Basin, NE Brazil. Journal of Structural Geology 32, 1783-1791. https://doi.org/10.1016/j.jsg.2009.08.019

Nicchio, M.A., Nogueira, F.C.C., Balsamo, F., Souza, J.A.B., Carvalho, B.R.B.M., Bezerra, FH.R., 2018. Development of cataclastic foliation in deformation bands in feldspar-rich conglomerates of the Rio do Peixe Basin, NE Brazil. Journal of Structural Geology 107, 132–141. https://doi.org/10.1016/j.jsg.2017.12.013

Nicchio, M.A., Balsamo, F., Cifelli, F., Nogueira, F.C.C., Aldega, L., Bezerra, F.H.R., Vasconcelos, D.L., Souza, J.A.B., 2022. An Integrated Structural and Magnetic Fabric Study to Constrain the Progressive Extensional Tectonics of the Rio do Peixe Basin, Brazil. Tectonics 41, e2022TC007244. https://doi.org/10.1029/2022TC007244

Nogueira, F.C.C., Oliveira, M.S., Castro, D.L., 2004. Reconhecimento aeromagnético e gravimétrico do arcabouço estrutural da Bacia Rio do Peixe - PB. Geologia, 17(1), 74–87.

Nogueira, F.C.C. Marques, F.O., Bezerra, F.H.R., de Castro, D.L., Fuck, R.A., 2015. Cretaceous intracontinental rifting and post-rift inversion in NE Brazil: Insights from the Rio do Peixe Basin. Tectonophysics 644- 645, 92-107. https://doi.org/10.1016/j.tecto.2014.12.016

Nogueira, F.CC., Nicchio, M.A., Balsamo, F., Souza, J.A.B., Silva, I.V.L., Bezerra, F.H.R., Vasconcelos, D.L., Carvalho, B.R.B.M., 2021. The influence of the cataclastic matrix on the petrophysical properties of deformation bands in arkosic sandstones. Marine and Petroleum Geology 124, 104825. https://doi.org/10.1016/j.marpetgeo.2020.104825

Ogilvie, S. R., Glover, P.W.J., 2001. The petrophysical properties of deformation bands in relation to their microstructure. Earth and Planetary Science Letters 193, 129–142. https://doi.org/10.1016/S0012-821X(01)00492-7

Oliveira, L.S.B., Nogueira, F.C.C., Vasconcelos, D.L., Balsamo, F., Bezerra, F.H.R., Pérez, Y.A.R., 2022. Mechanical stratigraphy influences deformation band pattern in arkosic sandstones, Rio do Peixe Basin, Brazil. Journal of Structural Geology 155, 104510. https://doi.org/10.1016/j.jsg.2022.104510

Orellana, E., 1972. Prospecion geoeletrica en corriente continua. Ed. Paraninfo, Madrid. 523 p.

Palhano, L.C., Nogueira, F.C.C., Marques, F.O., Vasconcelos, D.L., Bezerra, F.H.R., Souza, J.A.B., Nicchio, M.A., Perez, Y.A.R. Balsamo, F., 2023. Influence of hydrothermal silicification on the physical properties of a basin-boundary fault affecting arkosic porous sandstones, Rio do Peixe Basin, Brazil. Marine and Petroleum Geology 148, 106062. https://doi.org/10.1016/j.marpetgeo.2022.106062

Peacock, D.C.P., Nixon, C.W., Rotevatn, A., Sanderson, D.J., Zuluaga, L.F., 2016. Glossary of fault and other fracture networks. Journal of Structural Geology 92, 12–29. http://dx.doi.org/10.1016/j.jsg.2016.09.008

Pizzati, M., Balsamo, F., Storti, F., 2020. Displacement-dependent microstructural and petrophysical properties of deformation bands and gouges in poorly lithified sandstone deformed at shallow burial depth (Crotone Basin, Italy). Journal of Structural Geology 137, 104069. https://doi.org/10.1016/j.jsg.2020.104069

Pollard, D.D., Aydin, A., 1984. Propagation and linkage of oceanic ridge segments. Journal of Geophysical Research: Solid Earth 89, 10017–10028. https://doi.org/10.1029/JB089iB12p10017

Pontes, C.C.C, Nogueira, F.C., Bezerra, F.H R., Balsamo, F., Miranda, T.S., Nicchio, M.A., Souza, J.A.B., Carvalho, B.R.B.M., 2019. Petrophysical properties of deformation bands in high porous sandstones across fault zones in the Rio do Peixe Basin, Brazil. International Journal of Rock Mechanics And Mining Science 114, 153–163. https://doi.org/10.1016/j.ijrmms.2018.12.009

Pyrcz, M.J., Deutsch, C.V., 2014. Geostatistical Reservoir Modeling. University Press, Oxford, 2nd Edition, New York, p. 448.

Qu, D., Tveranger, J., 2016. Incorporation of deformation band fault damage zones in reservoir models. AAPG Bulletin 100, 423–443. https://doi.org/10.1306/12111514166

Qu, D., Tveranger, J., Fachri, M., 2017. Influence of deformation-band fault damage zone on reservoir performance. Interpretation 5, 41–56. https://doi.org/10.1190/INT-2016-0229.1

Ramos, G.V., Vasconcelos, D.L., Marques, F.O., de Castro, D.L., Nogueira, F.C.C., Bezerra, F.H.R., Perez, Y.A.R., Souza, J.A.B., Medeiros, V.C., 2022. Relations between inherited basement fabric and fault nucleation in a continental setting: The Rio do Peixe Basin, NE Brazil. Marine and Petroleum Geology 139, 105635. https://doi.org/10.1016/j.marpetgeo.2022.105635

Ramos, G.V., de Castro, D.L., Vasconcelos, D.L., Nogueira, F.C.C., Bezerra, F.H.R., & Nicchio, M.A., 2024. Tectonophysics 871, 230173. https://doi.org/10.1016/j.tecto.2023.230173

Rapozo, B.F., Cordoba, V.C., Antunes, A.F., 2021. Tectono-stratigraphic evolution of a cretaceous intracontinental rift: example from Rio do Peixe Basin, northeastern Brazil. Marine and Petroleum Geology 126, 104899. https://doi.org/10.1016/j.marpetgeo.2021.104899

Ringrose, P., Bentley, M., 2021. Reservoir Model Design, A Practitioner's Guide. Second Edition. Springer Nature Switzerland AG, 322p. https://doi.org/10.1007/978-94-007-5497-3

Roesner H.E., Lana C.C., Le Herissé A., Melo J.H.G., 2011. Bacia do Rio do Peixe (PB). Novos resultados biocronoestratigráficos e paleoambientais. In: Carvalho I.S., Srivastava N.K., Strohschoen Jr O., Lana C.C. (Eds.) Paleontologia: Cenários de Vida, 3. Rio de Janeiro. Interciência, 135-141.

Rotevatn, A., Fossen, H., Hesthammer, J., Howell, J.A., 2007. Are relay ramps conduit for fluid flow? Structural analysis of a relay ramp in Arches National Park, Utah. In Lonergan, L., Jolly, R.J.H., Sanderson, D.J., Rawnsley, K. (Eds.), Fractured Reservoirs, Geological Society, London, Special Publications 270, 55-71. http://dx.doi.org/10.1144/GSL.SP.2007.270.01.04

Rotevatn, A., Tveranger, J., Howell, J.A., Fossen, H., 2009. Dynamic investigation of the effect of a relay ramp on simulated fluid flow: geocellular modelling of the Delicate Arch Ramp, Utah. Petroleum Geoscience 15, 45–58. https://doi.org/10.1144/1354-079309-779

Rotevatn, A., Fossmark, H. S., Bastesen, E., Thorsheim, E., Torabi, A., 2017. Do deformation bands matter for flow? Insights from permeability measurements and flow simulations in porous carbonate rocks. Petroleum Geoscience 23, 104–119. https://doi.org/10.1144/petgeo2016-038

Silva, A. C. E. (2022). Efeito das Estruturas de Linkagem no Fluxo de Fluidos em Zona de Falha de Bandas de Deformação na Bacia Rio do Peixe, Nordeste do Brasil. Master Dissertation, Federal University of Campina Grande, 73p. Available at: http://dspace.sti.ufcg.edu.br:8080/xmlui/handle/riufcg/27499

Silva, J.G.F., Cordoba, V.C., & Caldas, L.H.C. (2014). Proposta de novas unidades litoestratigráficas para o Devoniano da Bacia do Rio do Peixe, Nordeste do Brasil. Brazilian Journal of Geology 44, 561–578. https://doi.org/10.5327/Z2317488920140004004

Silva, M.E., Nogueira, F.C.C., Perez, Y.A.R., Vasconcelos, D.L., Stohler, R.C., Sanglard, J. C.D., Balsamo, F., Bezerra, F.H.R., Carvalho, B.R.B.M., Souza, J.A.B., 2022. Permeability modeling of a basin-bounding fault damage zone in the Rio do Peixe Basin, Brazil. Marine and Petroleum Geology 135, 105409 https://doi.org/10.1016/j.marpetgeo.2021.105409

Skurtveit, E., Torabi, A., Sundal, A., Braathen, A., 2021. The role of mechanical stratigraphy on CO2 migration along faults-examples from Entrada Sandstone, Humbug Flats, Utah, USA. International Journal of Greenhouse Gas Control 109, 103376. https://doi.org/10.1016/j.ijggc.2021.103376

Souza, F.M., Gomes, I.F., Nogueira, F.C.C., Vasconcelos, D.L., Canabarro, B., Souza, J.A. B., Guimarães, L.J.N., Beserra, L.B.S., 2022. 2D modeling and simulation of deformation bands' effect on fluid flow: implications for hydraulic properties in siliciclastic reservoirs. Journal of Structural Geology 158, 104581. https://doi.org/10.1016/j.jsg.2022.104581

Stohler, R.C., Nogueira, F.C.C., Mello, C.L., Souza, J.A.B., 2022. 3D numerical modeling and simulation of the impact of fault zones on fluid flow in sandstones of the Rio do Peixe Basin, NE Brazil. Petroleum Geoscience 28, petgeo2022-024. https://doi.org/10.1144/petgeo2022-024

Tiab, D., Donaldson,E.C., 2004. Petrophysics. [S.l: s.n.].

Torabi, A, Balsamo, F., Nogueira, F.C.C., Vasconcelos, D.L., Silva, A.C.E., Bezerra, F.H.R., Souza, J.A.B., 2021. Variation of thickness, internal structure and petrophysical properties in a deformation band fault zone in siliciclastic rocks. Marine and Petroleum Geology 133, 1-24. https://doi.org/10.1016/j.marpetgeo.2021.105297

Vasconcelos, D.L., Marques, F.O., Nogueira, F.C.C., Perez, Y.A.R., Bezerra, F.H.R., Stohler, R.C., Souza, J.A.B., 2021. Tectonic inversion assessed by integration of geological and geophysical data. The intracontinental Rio do Peixe Basin, NE Brazil. Basin Research 33, 705–728. https://doi.org/10.1111/bre.12491

Winsauer, W.O., Shearin, H.M., Masson, P.H and Williams, M., 1952. Diffusion coefficients in nearshore marine sediments, Limnol. Oceanography 27, 552.

Zuluaga, L.F., Rotevatn, A., Keilegavlen, E., Fossen, H., 2016. The effect of deformation bands on simulated fluid flow within fault-propagation fold trap types: Lessons from the San Rafael monocline, Utah. AAPG Bulletin 100, 1523–1540. https://doi.org/10.1306/04151614153

Capítulo 6

Conclusões e Sugestões

6. Conclusões e Sugestões

Esta tese teve por estrutura os 2 *papers*, sendo o *paper* 1 (Afloramento Melancias) focado na modelagem e simulação bidimensional de alta fidelidade, onde foram inseridas uma complexa estrutura de bandas de deformação, representando assim as características fidedignas da área enquanto o *paper* 2 (Afloramento Utah) teve uma abordagem mais generalista, tendo a estrutura principal sido incorporada dentro do modelo tridimensional. Dentro deste contexto, observa-se que a modelagem geológica para o modelo 2D é mais detalhada, haja vista a área de estudo foi menor, quando comparada com a área 3D. A análise 2D e 3D construída nesta tese e, interpretada em conjunto, nos permitiu concluir que:

1- O padrão anastomosado das bandas de deformação, juntamente com as interseções é determinante para o comportamento do fluxo;

2- A simulação 2D mostrou o efeito parcial de barreira causado pelas bandas de deformação, indicando assim sua influência no fluxo de fluidos. Isso foi possível observar através dos saltos de pressão observados nos perfis gerados;

3- A rocha hospedeira precisa ter, pelo menos, 3 ordens de grandeza de diferença nos valores de permeabilidade para que esse contraste mostre claramente os efeitos das bandas de deformação no fluxo;

4- As orientações das bandas de deformação são determinantes para a identificação se as mesmas irão atuar como barreiras parciais ou condutos no fluxo. Quando temos o fluxo paralelo as bandas, estas agem como conduto. Quando se tem o fluxo obliquo as bandas, estas irão atuar como barreiras parciais;

5- A modelagem e simulação 3D identificou que os maiores constrastes nos valores de porosidade ao longo do cluster foi observado nas zonas de linkagem e nos valores de permeabilidade foi na porção mais fina do cluster;

6- O levantamento de resistividade elétrica se mostrou eficiente para geração do modelo de porosidade, bem como de um custo menor do que a amostragem convencional;

7- O modelo de porosidade gerado a partir da inversão dos dados de resistividade elétrica pode ser utilizado como tendência para geração de modelos de permeabilidade, similiar ao que acontece na inversão sísmica;

8- Os valores de permeabilidade ao redor do custer são maiores que os relatados anteriormente e em zonas mais distantes do cluster se tem maiores valores de permeabilidade, mostrando assim a complexidade da área de estudo. Entretanto, numa zona mais fina foi verificado altos valores de permeabilidade e neste ponto o fluido cruzou em todos os casos. Isto mostra que considerar a distribuição da permeabilidade homogênea ou constante ao longo do cluster pode levar a um efeito barreira falso;

9- Os clusters de bandas de deformação atuam ora como barreira e ora como conduto, variando de acordo com a distribuição de poços;

10- A conectividade hidráulica no cluster é influenciada pelas zonas de linkagem, onde zonas de alta complexidade podem atuar aumentando a permeabilidade efetiva.

Como sugestões para trabalhos futuros, temos:

- Implementar os dados de poços perfurados no afloramento 2 (espessura de camadas; litologias; propriedades petrofísicas in situ; propriedades dos fluidos).;
- Inserção dos clusters menores no modelo geológico 3D;
- Coletar, onde for possível, medidas tridimensionais de permeabilidade para construir diferentes cenários de permeabilidade, haja vista a distribuição não é isotrópica;
- Utilizar os valores de Keqv obtidos na modelagem 2D para povoar locais no modelo que possuam as mesmas características;
- Realizar projetos de produção/otimização para ter um controle de qual melhor disposição de poços seja mais eficiente para desenvolver um campo de petróleo.